RECONFIGURABLE DIRECT SPACE-TO-TIME PULSE SHAPING

A Thesis

Submitted to the Faculty

of

Purdue University

by

Nathaniel A. Webster

In Partial Fulfillment of the

Requirements for the Degree

of

Doctor of Philosophy

December 2005

For my grandfathers, Robert Webster and John Kikuchi.

ACKNOWLEDGMENTS

This work would not have been possible without the help of my advisor, Professor Andrew Weiner. His guidance and support throughout my time at Purdue have been invaluable. I would also like to thank Dan Leaird and Al Vega, for their advice, collaboration, and encouragement.

TABLE OF CONTENTS

LIST OF TABLES

LIST OF FIGURES

Figure   Page

ABBREVIATIONS

WDM	wavelength division multiplexing
OTDM	optical time division multiplexing
DST	direct space-to-time
AWG	arrayed waveguide grating
DSTAWG	direct space-to-time arrayed waveguide grating
ASE	amplified spontaneous emission
OSA	optical spectrum analyzer
FWHM	full width at half max
BP	band pass
SHG	second harmonic generation
EDFA	erbium doped fiber amplifier
FSR	free spectral range
RMS	root mean square
SLM	spatial light modulator
AFP	asymmetric Fabry-Perot
AFPM	asymmetric Fabry-Perot modulator
MQW	multiple quantum well
QCSE	quantum confined Stark effect
DBR	distributed Bragg reflector
PIN	p-type/intrinsic/n-type diode
FTIR	Fourier transform infra-red spectrometer

ABSTRACT

Webster, Nathaniel A. Ph.D., Purdue University, December, 2005. Reconfigurable Direct Space-To-Time Pulse Shaping. Major Professor: Andrew M. Weiner.

The Ultrafast optical word generator is an optical fiber communication subsystem under development by several researches in the Ultrafast Optics Lab. This system proposes to take parallel electrical data streams and serialize them onto a single optical channel. Potential applications of the optical word generator include its use in optical time-division multiplexing and also in the encryption of high-speed optical data streams. Two of the main components of the word generator are the direct space to time arrayed waveguide grating pulse shaper (DSTAWG), and the asymmetric Fabry-Perot modulator (AFPM).

This thesis covers development and modifications of the DSTAWG for incorporation into the word generator, and demonstrates reconfigurable direct space to time pulse shaping. The design of the AFPM is described and development of its fabrication process is discussed. The results of fabrication efforts to date are cataloged.

1. MOTIVATION: OPTICAL WORD GENERATOR

Future optical communications networks are expected to require increasingly higher bit rates to accommodate the rapid growth of internet traffic as well as new types of data services. Historically the bandwidth demand has successfully been met by expanding the number of channels per optical link, through the widely adopted use of wavelength division multiplexing (WDM). In a typical WDM system the channel rate is constrained by the limits of electronic modulation to 10 to 40 Gb/s, however the overall system rate can be much higher through multiplication by the number of channels. For example, dense WDM systems employing over a hundred 10 Gb/s channels for system rates over 1Tb/s are commercially available. [7]

As the demand for more transmission capacity continues to rise, new techniques will be needed to produce the bit rates required. One promising technology is optical time division multiplexing (OTDM), which allows the single-channel bit rate to be increased beyond the electronic modulation limit. [8] [9] A schematic representation of a generalized OTDM system [1] in Fig. 1.1 illustrates the time-slot multiplexing of channels. Several demonstrations of 160 Gb/s OTDM systems have been reported [10], both through 16×10Gb/s multiplexing [11], and multiplexing 4×40Gb/s data streams [12] [13]. One group has reported a 1.28 Tb/s transmission system that combines OTDM and polarization multiplexing. [14] Hybrid OTDM/WDM systems that take advantage of the higher channel rate of OTDM systems as well as the multi-channel capacity of WDM systems have also been proposed. [15] [16]

Many of the demonstrations of OTDM systems achieve high (160 Gb/s or more) data rates by interleaving multiple copies of a single lower rate channel. In this method, a single 10 or 40 Gb/s channel is generated, then split multiple times and delayed, either by means of multiple fiber delay stages [10] or a planar lightwave
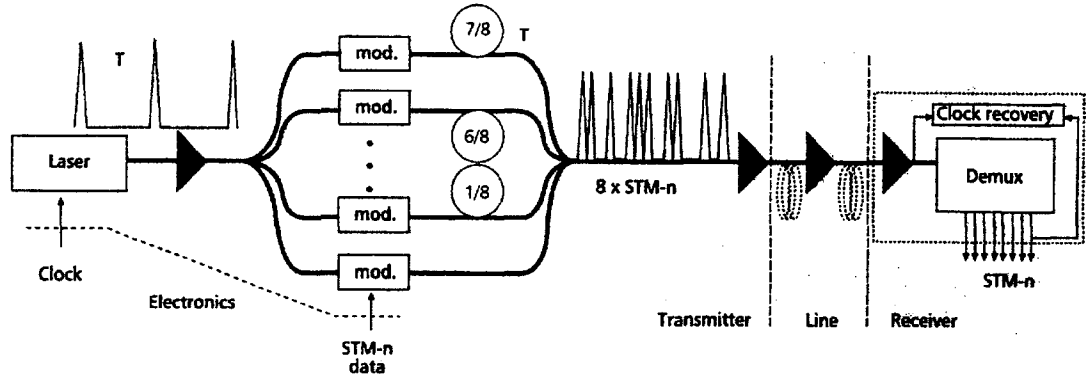
Fig. 1.1. Schematic illustration of a generalized OTDM transmission system. Figure taken from Spirit et. al. [1]

circuit [14] [13]. These appropriately delayed copies are then recombined to form the high rate channel. An arguably more realistic multiplexing method would entail encoding each low-rate channel separately before multiplexing. One such system, employing bulk optic delay lines, has been demonstrated to modulate four separate 40 Gb/s channels and then multiplex them onto a single 160 Gb/s channel. [17] Another implementation using a planar waveguide circuit 1-to-4 splitter, four integrated modulators, and planar delay line circuit has also been proposed. [18]
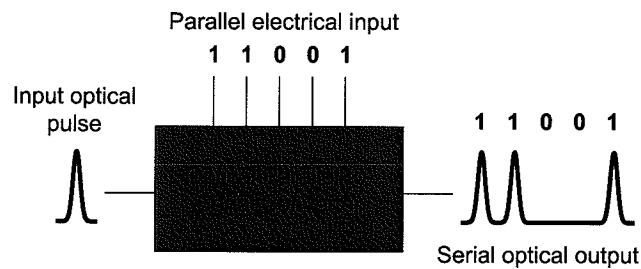
Fig. 1.2. Block diagram of the optical word generator.

The optical word generator described in this thesis is a method of generating patterned pulse trains that may be scaled to be used as a high bit-rate OTDM data

source. The optical word generator is essentially an electrical-to-optical parallel-to-serial multiplexer. The inputs to the word generator are a single ultrashort ($\sim$250 fs) optical pulse, and multiple parallel electrical signals. As shown in the block diagram of Fig. 1.2, the output is an ultrafast optical pulse packet containing the serialized input data.

One potential application of the optical word generator is the encryption of high bit-rate optical data streams. Electronic-only encryption schemes typically are limited to data rates of 10 Gb/s and below. [19] The ability to take a high-speed optical data stream and encrypt it in the physical layer with hybrid optical/optoelectronic systems is desirable. A block-diagram representation of a possible encryption scheme, proposed by researchers at the National Security Agency, is shown in Fig. 1.3.
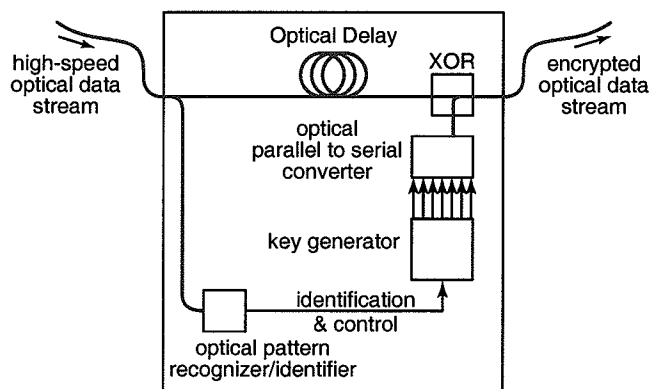
Fig. 1.3. High-speed optical encryption. (adapted from Jeff Ingle, Dept. of Defense)

One implementation of an optical encryption system would combine the optical word generator with a time-to-space optical converter [20], as shown in Fig. 1.4 The serial-to-parallel functionality of the time-to-space optical converter separates the n-bit serial optical data packet into n spatially separated pulses. An $n \times 1$ optoelectronic smart pixel array then processes the bits in parallel at the lower speed of the frame-rate (as opposed to the bit-rate). For example, for the 6-pulse data packet shown in Fig. 1.4, the frame-rate might be 10 Gb/s yielding a bit-rate of 60 Gb/s. The

advantage of this method is that the encryption can be carried out at the slower-speed frame-rate. The n parallel signals are then serialized by the optical word generator reproducing the high bit-rate data stream but now in encrypted form.
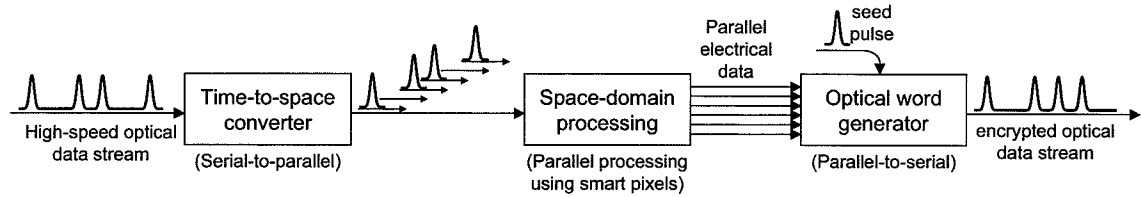
Fig. 1.4. Space-time optical system for encryption of high-speed optical data streams

The two fundamental components of the optical word generator are an integrated direct space-to-time pulse shaper and a high speed optical modulator array. The remainder of this thesis is divided into a discussion of these two components. The first half is organized as follows. Section 2 introduces the arrayed wavguide grating used in the word generator. Section 3 outlines measurement methods used in experiments with the arrayed waveguide grating. Sections 4 and 5 discus the spectral and temporal characteristics of the arrayed waveguide grating pulse shaper. Section 6 discusses modifications of the pulse shaper to accommodate a modulator, and Section 7 reports the results of reconfigurable pulse shaping. The organization of the second half of this thesis, a discussion the optical modulator array, is outlined in Section 8.

2. OPTICAL PULSE PACKET GENERATION WITH AN ARRAYED WAVEGUIDE GRATING

The ability to produce and shape femtosecond optical pulse packets is an integral requirement of the optical word generator. Arrayed waveguide gratings (AWGs) [21] have shown effective femtosecond pulse train generation [22, 23], while the ability to both generate and shape pulse trains has been demonstrated using direct space-to-time (DST) pulse shapers. [24, 25] Combining these two technologies, the integrated direct space-to-time arrayed-waveguide-grating (DSTAWG) pulse shaper, has likewise demonstrated shaped optical pulse packet generation in a more compact form. [26, 27] The DSTAWG in combination with a fixed spatial mask produces a direct mapping in the time domain of the spatial masking pattern used. [27] Building on the previous work, this thesis demonstrates re-configurable pulse shaping using a modified DSTAWG pulse shaper in combination with a spatial light modulator array (SLM) [28].

2.1 AWG Device Explanation

Arrayed waveguide gratings were developed for use as wavelength channel multiplexers and demultiplexers in WDM applications, and are widely adopted. [29] [30] [21] Devices with as many as 512 channels spaced at 10 GHz have been reported. [31] The AWG is an integrated optical planar waveguide circuit, often fiber coupled, and is typically fabricated within deposited silica layers on a substrate of silicon or silica. Cladding and core layers are deposited on the substrate and are lithographically patterned and etched to form the waveguide structures. [21]
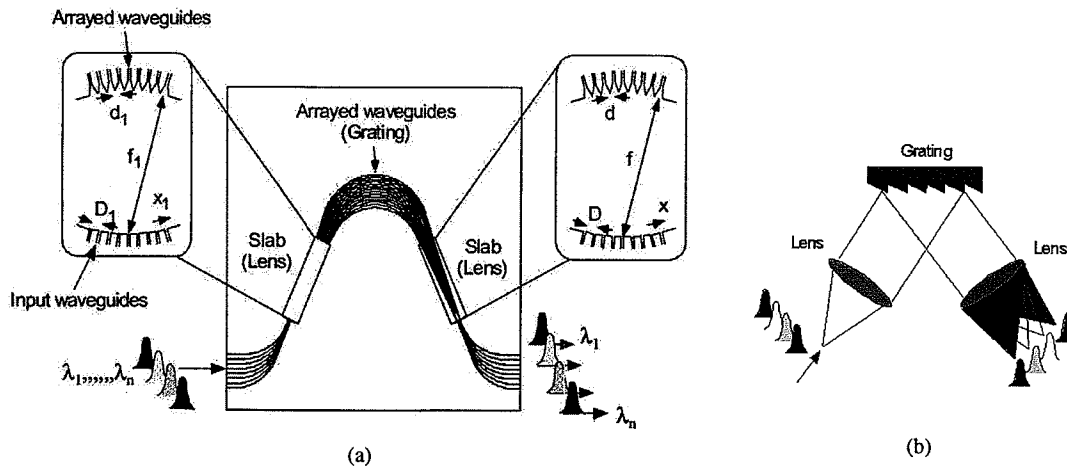
Fig. 2.1. Comparison of an AWG (a), and bulk optics grating and lenses (b). Figure taken from Hibino [2].

The AWG is analogous to the bulk optics grating and lens arrangement shown in Fig. 2.1b. [2] In the AWG, input light is spread out in the slab waveguide and coupled into each guide of the waveguide array. The slab is analogous to the first collimating lens in Fig. 2.1b. The waveguide array has a constant path length difference of ΔL between adjacent guides, and functions as a phased array, where the phase difference $\Delta L/\lambda$ is dependent on wavelength. The waveguide array is analogous to the diffraction grating in Fig. 2.1b. At the output of the phased array, light from each of the guides (effectively phased emitters) propagates through the second slab section and interferes constructively at only one of the output waveguides. Different wavelengths interfere constructively at different output waveguides, giving the AWG its demultiplexing capability. The second slab guide is comparable to the focusing lens in Fig. 2.1b. [2] [32]

The modified arrayed waveguide grating used in these experiments is depicted in Fig. 2.2a, and for comparison a conventional AWG structure is represented in Fig. 2.2b. The modified device used is essentially the first half of the standard AWG structure, consisting of several fiber-coupled input waveguides, or ports, a slab waveguide section, and finally the multiple arrayed waveguides. In both devices, the

waveguide array incorporates a constant path length difference ΔL between adjacent guides. In the modified AWG, however, there is no second slab, and the arrayed guides are terminated at the edge of the device, which enables free space access to the waveguide array. The conventional AWG is typically used in transmission mode, whereas the modified AWG is designed to operate in double-pass as a reflection device, with a reflector coupled to the free space interface. When operated in reflection mode, the modified device behaves essentially like a conventional AWG, with the input ports also doubling as output ports.
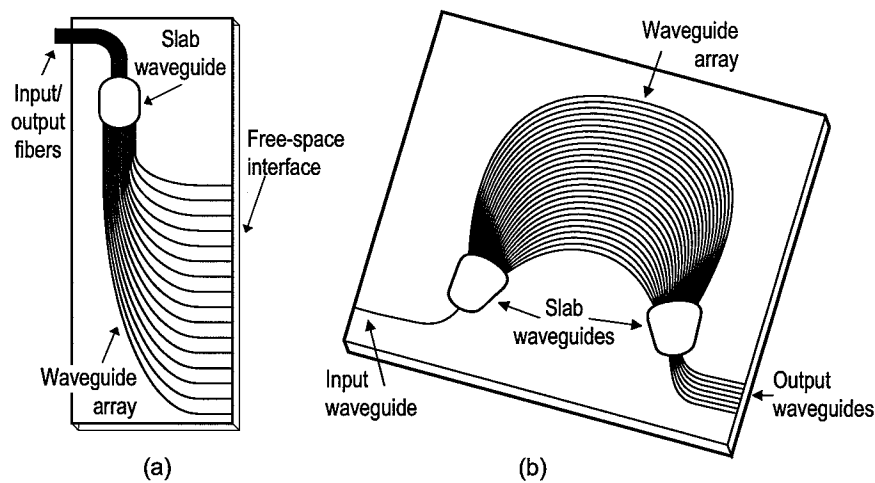
Fig. 2.2. (a) Modified arrayed waveguide grating. (b) Conventional arrayed waveguide grating.

The AWG[1] discussed in the remainder of this thesis has had extra loss added to some of the waveguides in order to equalize the power per guide. Without this loss engineering, a gaussian power distribution across the 16 arrayed waveguides would be present. This uneven power distribution is due to the spreading of the initial input pulse in the slab waveguide section. Like a gaussian beam exiting a single mode fiber, the input pulse has a gaussian cross-sectional profile. As the beam expands

---

[1]The AWG used in the experiments described in this thesis was designed by Dan Leaird in collaboration with Katsunari Okamoto. It was procured through a grant from the Photonics Technology Access Program, administered by the Optoelectronics Industry Development Association. It was fabricated at NTT Electronics Corporation (NEL) under the direction of Katsunari Okamoto.

in the slab, it maintains a gaussian profile, resulting in more power coupling into the center guides of the waveguide array, and less into the outer guides. [21] The additional loss engineered into the waveguide array has been designed to equalize the power per guide when light is double passed through the device. The motivation for equalizing the power per guide is that it enables the generation of flat topped temporal pulse trains. This can be seen in the cross-correlation trace of Fig. 4.5a and will become clearer in Section 5.

The device, shown in Fig. 2.2a, has eight fiber-coupled input/output ports[2] and 16 arrayed waveguides. The constant path length difference ΔL between adjacent waveguides produces a delay τ of about 0.79 ps between guides as measured at the free-space interface. The spacing between waveguides at the free-space interface is $150\,\mu$m. Note that this spacing is dependent on the particular layout geometry of the AWG, and is not necessarily directly related to ΔL. However, the path length difference corresponds to the delay between adjacent guides according to $\Delta L = \tau \times \frac{c}{n}$, which, for an assumed refractive index $n = 1.5$, gives $\Delta L = 158 \mu$m.

---

[2]The eight input waveguides are hereafter termed 'ports' to avoid confusion with the 16 arrayed waveguides

3. EXPERIMENTAL METHODS

The experiments that are described in this thesis were carried out using the experimental setups shown in Fig. 3.1. For the spectral measurements, an amplified spontaneous emission (ASE) source was used as the light source, and the output spectrum of the DSTAWG was measured using an optical spectrum analyzer (OSA). The 3dB bandwidth of the ASE source was approximately 40 nm, centered at 1547 nm, and the total source power was measured at 15 dBm. Fig. 3.2 shows the power spectrum of the ASE source, taken using an OSA bandwidth resolution of 0.05 nm.
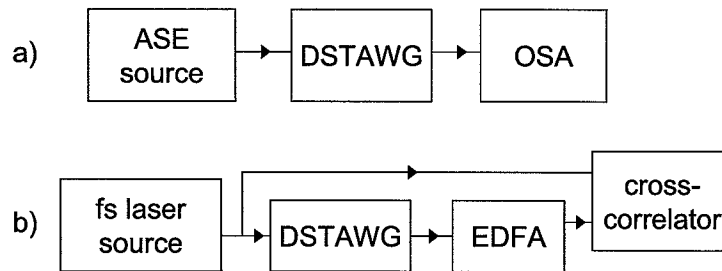
Fig. 3.1. (a) Spectral measurement setup. (b) Time domain pulse measurement setup.

For the time domain pulse measurements, a passively mode-locked fiber laser was used as the light source, producing short pulses of approximately 70 fs at FWHM, at a repetition rate of 50 MHz. [33,34] A bandpass filter was placed at the laser output, limiting the bandwidth to approximately 20 nm centered at 1560 nm. The filter was necessary to accommodate an erbium fiber amplifier, which has limited bandwidth and was needed to amplify the output of the DSTAWG. Fig. 3.3a shows the power spectrum of the source laser with and without the bandpass filter. Fig. 3.3b shows
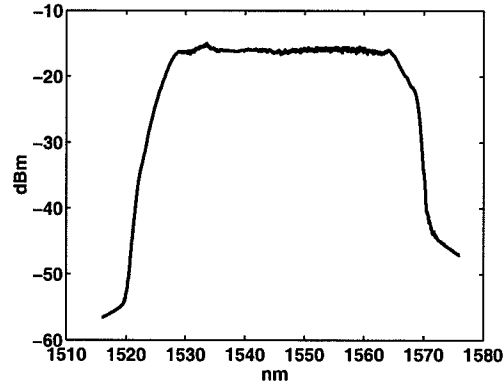
Fig. 3.2. ASE source spectrum

auto-correlation traces of the source laser with and without the BP filter. The full width half max of the pulses are 71 fs without the filter, and 258 fs with the filter.

(a)   (b)
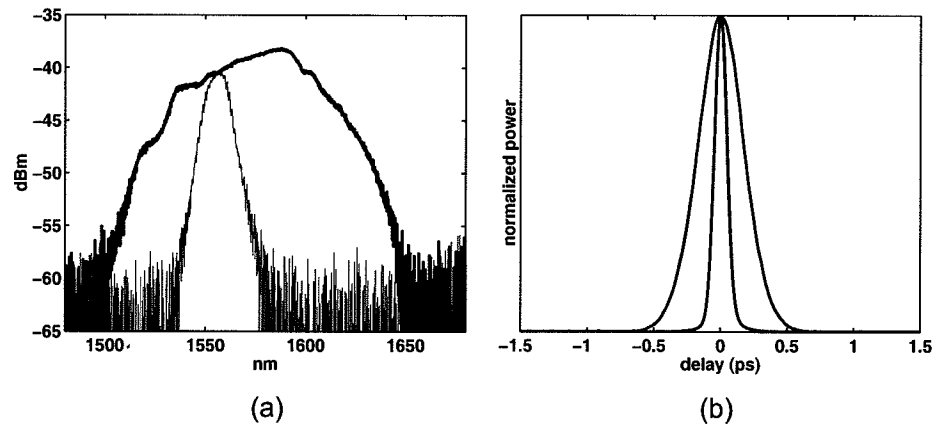
Fig. 3.3. (a) Femtosecond laser spectrum with(green) and without(blue) the BP filter. (b) Auto-correlation pulse measurements of the source laser with(green) and without(blue) the BP filter.

The output pulse trains were measured using an optical intensity cross-correlator, as shown in Fig. 3.1b. The cross-correlator contains two paths, a signal and reference path, with variable delay between the paths. A short reference pulse, split off from the source laser, is delay scanned through the signal pulse (or pulse train) under measurement. These two beams are focused onto a non-linear crystal which

generates an axial second harmonic output when both reference and signal pulses are present. By stepping the delay between the two arms and measuring the SHG output, the cross-correlation trace is produced. The fiber links of the reference path (from source to correlator) as well as the signal path (from source to DSTAWG to EDFA to correlator) must be carefully constructed so as to both have an appropriate delay and to be dispersion compensated. The delay is important so that the reference and signal pulses will overlap in time at the cross correlator. Chromatic dispersion compensation is important as well so that the ultrashort pulses do not become stretched out in the time domain as they traverse the fiber link and reach the cross correlator. Existing dispersion compensated links, constructed previously [27], were able to be reused for the experiments in this thesis.

4. SPECTRAL CHARACTERISTICS OF THE MODIFIED AWG

The modified AWG operated in reflection mode (i.e. with a mirror placed in direct contact to the free-space interface), displays many of the characteristics typically observed for a conventional AWG. For example, when a broadband source excites one of the input ports, the resulting power spectrum measured on any of the output ports displays a characteristic free spectral range (FSR). The FSR, as shown in Fig. 4.1, was measured at 630 GHz.[1] The device behaves as a phased array, where light double passing the 16 arrayed guides interferes in the slab portion causing different wavelengths to experience constructive or destructive interference as the light is coupled back into the output ports.
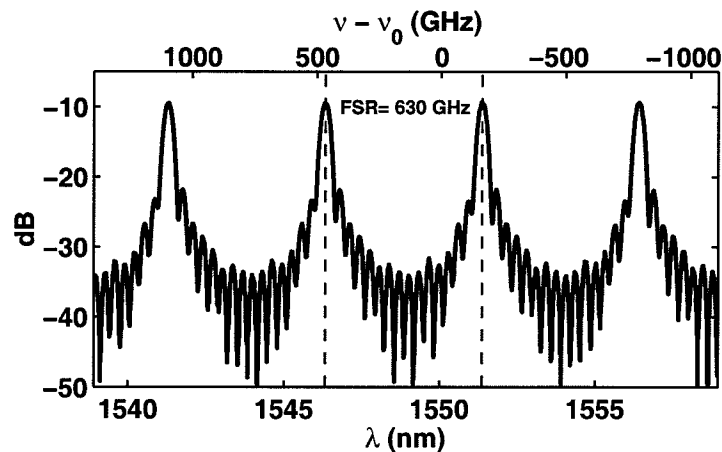
Fig. 4.1. Power spectrum for the modified AWG with a butt-coupled mirror. A broadband source is input on port 5, the output on port 4 is measured with an optical spectrum analyzer.

---

[1]The relationship between FSR and temporal pulse spacing will be discussed in Section 5

The modified AWG displays the wavelength separation characteristic of the conventional AWG as well. Fig. 4.2 shows different output ports corresponding to the different wavelength channels of the modified AWG. In the conventional AWG, typically only one wavelength channel is available at each output port, which is a necessary condition of the wavelength demultiplexing operation. [32] The FSR of the modified AWG is smaller than the bandwidth of the optical source, resulting in multiple wavelengths being observed at each output port. This is due to the design requirement that the delay increment between guides (inverse of FSR) be larger than the pulse duration (roughly inverse of the source bandwidth), in order to ensure that distinct output pulses are formed in the output pulse train. In Fig. 4.2, the "channel separation" $\Delta\lambda$, measured at 0.5 nm, is a function of the positioning of the output ports on the slab section and does not figure prominently in the use of the AWG as a pulse generator. However, the ratio of "channel width" to free spectral range, $\lambda_{\text{FWHM}}/\text{FSR}$, is useful for understanding the loss of the AWG.
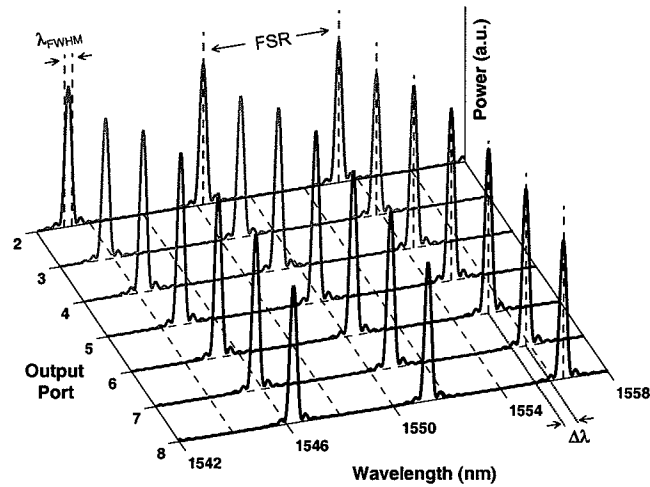
Fig. 4.2. Spectral response for multiple output ports on the modified AWG. Broadband input was launched on port 1. FSR $\simeq$ 5.1 nm, $\Delta\lambda \simeq$ 0.5 nm, $\lambda_{\text{FWHM}} \simeq$ 0.3 nm. For these measurements, the OSA bandwidth resolution was set to 0.05 nm.

4.1 AWG Loss

The loss measurements described here were performed with a mirror butt-coupled to the free-space interface of the AWG. Two types of loss measurement were performed. The spectrally integrated loss was measured by launching a broadband ASE source (Fig. 3.2) on port 1 of the AWG and measuring the power on port 6. This is a measure of the loss integrated over the entire source spectrum. An integrated-loss of 22 dB was obtained in this way. The peak-loss, or loss at the peak wavelength, was measured using a monochromatic continuous wave (CW) laser source, also launched on port 1 with the output measured on port 6. The CW source wavelength was tuned to align with a spectral peak for the port 6 output as shown in Fig. 4.3. Trace a is the AWG power spectrum measured on port 6, and trace b is the spectrum of the CW source tuned to a peak wavelength ($\sim$ 1550 nm) of the power spectrum. A peak wavelength loss of 10 dB was measured using this method.
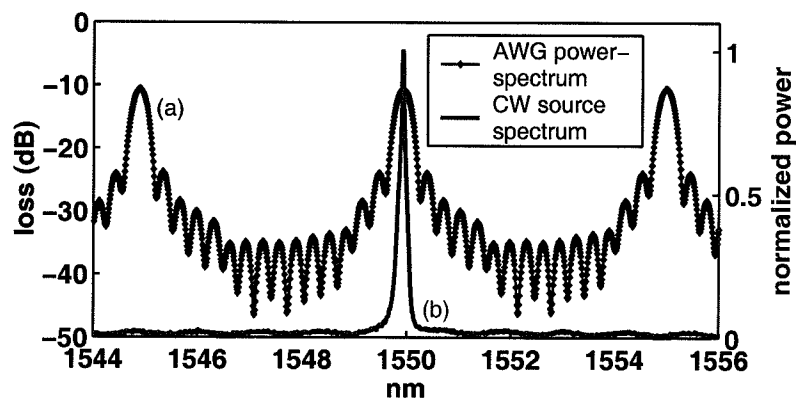
Fig. 4.3. (a) Power spectrum for the AWG with butt-coupled mirror, measured on port 6 with an optical spectrum analyzer. Broadband input was launched on port 1. (b) Spectrum of the monochromatic continuous wave (CW) source used for the peak-loss measurements. The plot overlay shows that the CW source is tuned to a spectral peak in the AWG response.

The 12 dB difference between the peak-loss and integrated-loss of the device is largely due to the wavelength filtering functionality of the AWG which is apparent

in Fig. 4.2. When output power is measured at any single output port, only a subset of the spectrum is sampled. The ratio of "channel width" to free spectral range, λ_{FWHM}/FSR in Fig. 4.2, gives an estimate as to how much of the integrated-loss is attributable to wavelength filtering. That ratio, 0.3/5.1, suggests that approximately 12 dB of the integrated-loss is due to spectral filtering. This estimate is in agreement with the difference between the measured integrated-loss and peak-loss, 22 dB - 10 dB = 12 dB. Some of the factors contributing to the 10 dB peak-loss are the intentional waveguide loss designed to flatten the pulse train, and the coupling loss between the fiber pigtails and the silica waveguides. Some minor power variation is evident between the output ports in Fig. 4.2, this is possibly due to non-uniform excitation of the different guides (power was launched into port 1 and spectral response was measured on ports 2-8). The integrated-loss was also measured with broadband power launched on port 5 and output measured on port 4 yielding a loss of 21 dB.

4.2 Internal Reflection of the modified AWG

One interesting characteristic of the modified arrayed waveguide grating which is not found in the traditional AWG is its internal reflection. The waveguides of the AWG device are fabricated on silicon dioxide deposited on a silicon substrate. The free-space interface, shown in Fig. 2.2a, is formed at the edge of the device where the wafer abruptly ends, due to cleaving or some other means. The discontinuity in refractive index at the glass to air interface gives rise to a small but measurable reflection, $\rho = \frac{n_1 - n_2}{n_1 + n_2}$. For $n_{air} = 1$ and $n_{glass} = 1.5$, the reflection $R = |\rho|^2$ is about 4%.

The internal reflection is evident in both the spectral and temporal performance of the AWG device. Fig. 4.4 shows the power spectra for the case of internal reflection alone, and also for the case of the mirror directly butt-coupled to the device at the free-space interface. The spectra are nearly identical, both displaying similar free spectral range. The primary difference is that the spectrum due to internal reflection

is approximately 14 dB down from the mirror reflection. With an assumed 4% glass/air reflection for trace b in Fig. 4.4, the 14 dB difference in trace a corresponds to a reflection of nearly 100%, as expected for a gold mirror ($\sim$ 98% at 1550 nm). Fig. 4.5 shows the intensity cross-correlations for the two cases. Again, they both show similar characteristics in terms of pulse spacing, the primary difference being less power in the internal reflection trace, as evidenced by the noisier signal. The temporal aspects of the AWG will be discussed in more detail in Section 5.
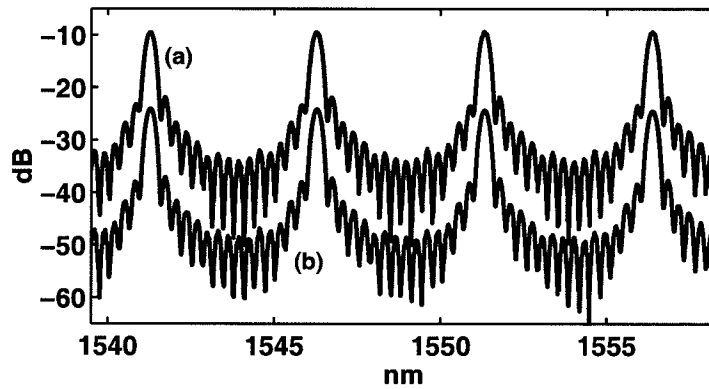
Fig. 4.4. Power spectra of the modified AWG. Trace (a) corresponds to the case of a mirror butt-coupled to the free-space interface. Trace (b) shows the case of internal reflection off the free-space interface.
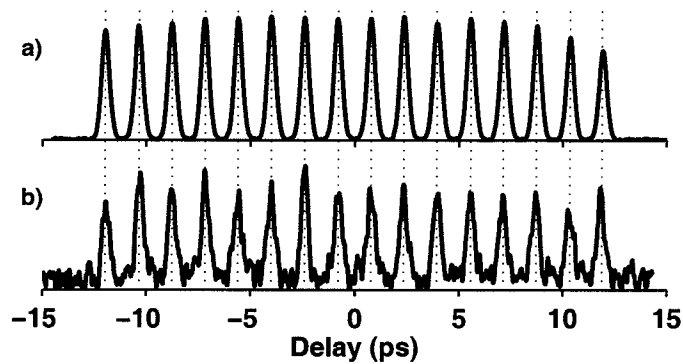
Fig. 4.5. Intensity cross correlation traces of the modified AWG for internal reflection only (b), and with a mirror butt-coupled to the free-space interface (a).

An attempt was made to suppress the internal reflection of the AWG by placing a 3° optical wedge and index matching fluid in contact with the AWG free-space interface. The index matching fluid would suppress the internal reflection, and the back reflection off of the wedge itself would be directed out of the plane of interest by the 3° angle. Fig. 4.6 shows that the addition of the wedge enabled the suppression of the internal reflection by about 20 dB. Ultimately however, with the later addition of relay optics to the setup, the internal reflection artifacts became temporally separated from the pulse trains of interest, and the wedge was removed.
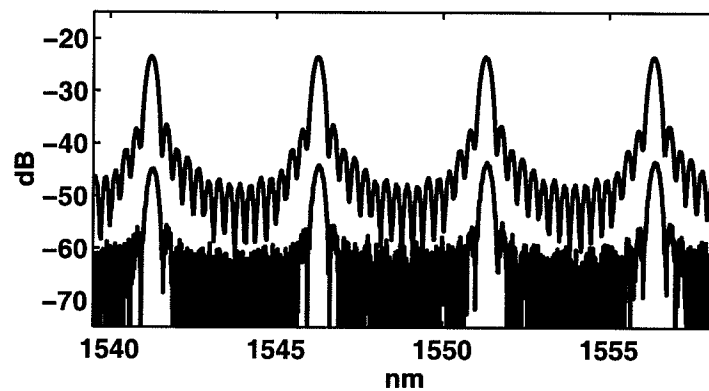
Fig. 4.6. Power spectrum for the AWG alone (top, red) and for the AWG with the 3° wedge (bottom, black)

5. SIMPLE PULSE TRAIN GENERATION

The constant path length increment between adjacent guides of the waveguide array is what enables the device to generate optical pulse trains. [23] When the input excitation is a short pulse and the pulse duration is shorter than the delay increment per guide, the resulting temporal trace is a train of pulses with the number of pulses equal to the number of arrayed waveguides. [27] This one-guide one-pulse argument [22] is illustrated in Fig. 5.1 where a short pulse excites one of the input ports. The pulse then spreads out in the slab section and excites individual pulses in each guide of the array. These 16 pulses traverse the waveguide array and are separated in time due to the path length difference across the array. The one to one relationship between a waveguide and its corresponding pulse also explains how adjusting the loss on a per-waveguide basis enables flat-topped pulse train generation.

**Modified Arrayed
Waveguide Grating**

1 2 3 · 16
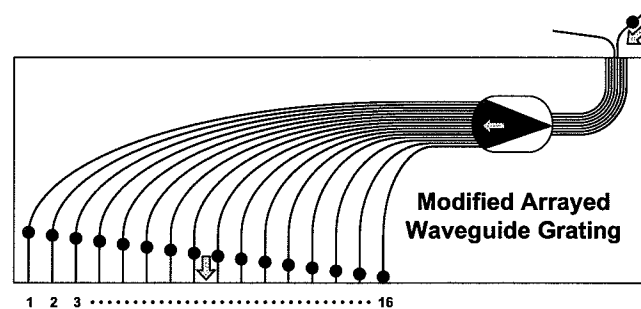
Fig. 5.1. Modified AWG under short pulse excitation. The waveguides are numbered for future reference.

When a mirror is placed in direct contact to the free-space interface of the AWG, each individual pulse is reflected directly back into its corresponding guide and re-traverses the waveguide array in reverse, picking up additional delay. The pulses

then re-enter the slab and excite 16 pulses in each of the output ports. Fig. 5.2 shows the resultant 16 pulse train for one of the output ports.
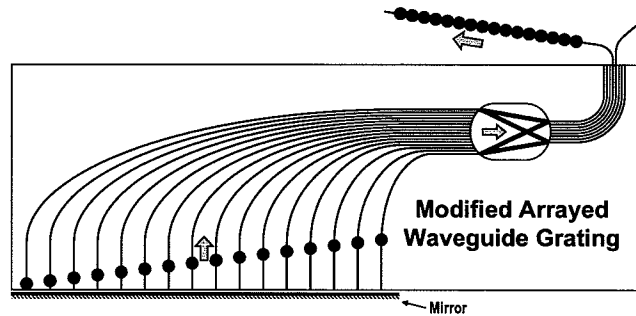
Fig. 5.2. Modified AWG in double-pass looking at the output pass and pulse recombination in the device

Fig. 5.3 is an optical intensity cross-correlation measurement taken on one of the output ports while the AWG was under short pulse excitation. The measured temporal profile displays a 16-pulse train in agreement with the one-guide one-pulse picture. The temporal profile can also be compared with the spectral data in Fig. 4.1. The time delay between pulses corresponds to the inverse of the free spectral range, $\Delta \tau = \frac{1}{FSR}$. [23] For the measured data $\frac{1}{630\text{GHz}} \simeq 1.59\text{ps}$.
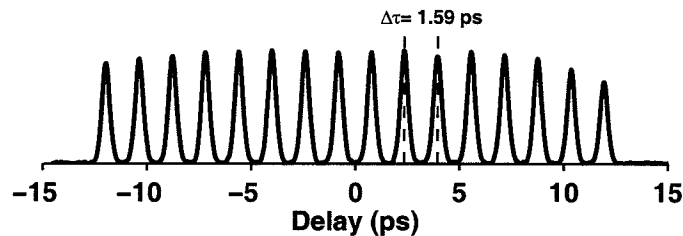
Fig. 5.3. Intensity cross correlation trace for modified AWG with butt-coupled mirror. Femtosecond source input on port 5, output on port 4

Although it is not depicted in Fig. 5.2, after the re-traversal of the waveguide array, a 16-pulse burst is excited in each of the output ports of the AWG, not just

one. In Fig. 5.4, intensity cross-correlation measurements show essentially identical output pulse trains in the time domain for each of the output ports.
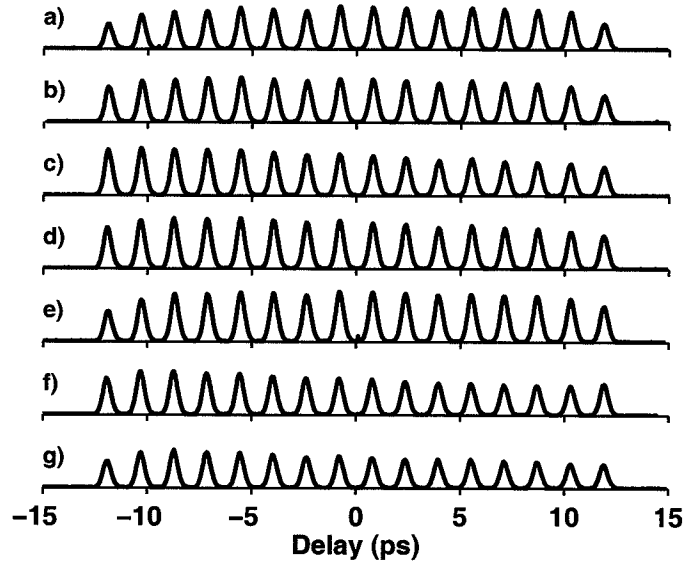
Fig. 5.4. Intensity cross-correlation traces for the AWG with mirror directly butt-coupled to the free-space interface. Input pulse is on port 1, traces (a)-(g) correspond to output measured on ports 2-8 respectively. The traces show similar 16-pulse trains.

5.1   Direct Space-to-Time Pulse Shaping

By replacing the mirror with a patterned reflective mask, the modified AWG becomes a direct space-to-time pulse shaper. Such DSTAWG pulse shapers have previously demonstrated 30 pulse packet generation. [27] Similar results are reproduced here with the 16 pulse AWG using a standard semiconductor lithography grade photomask of patterned chrome on glass Fig. 5.5a. The mask pattern, designed using WaveMaker layout software, consists of two columns of pseudo-random binary (on/off) pixel strings repeating in a 16-bit period. Each pixel is 150 μm wide, to match the AWG's guide spacing, and 2.5 mm tall, to facilitate vertical alignment. For example, the simple 3-pixel string '101' would consist of a 150 μm × 2.5 mm

chrome rectangle on the surface of the mask adjacent to an equally sized 'open' rectangle of bare glass, followed by a second chrome rectangle.
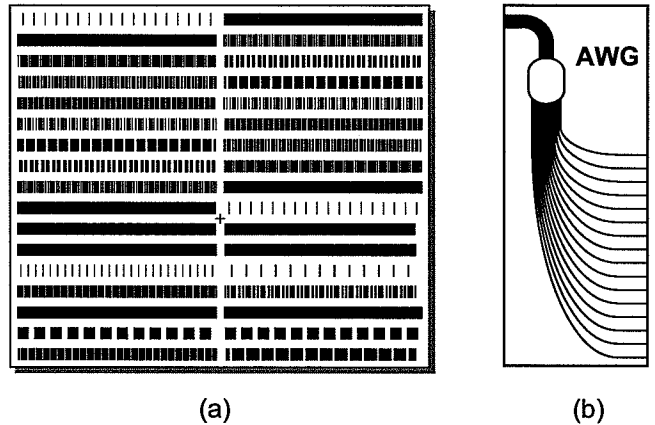
Fig. 5.5. (a) Patterned chrome on glass photomask. (b) Config-uration of the AWG with the mask butt-coupled to the free-space interface.

The obvious effect of replacing the mirror with the reflective mask is to select a subset of the 16 guides and reflect the light from only those guides, allowing it to be coupled back into the AWG. The guides which are not reflected simply transmit through the transparent area of the mask and the light is lost. Due to the fact that each guide corresponds one-to-one with a single pulse, the resulting pulse train will have some of its pulses suppressed while others will be preserved. The pulse train pattern is a direct mapping in time of the spatial masking pattern. Fig. 5.6 shows intensity cross-correlation traces for the case of mask pattern '1010011110101010'. The mask was butt-coupled to the AWG free-space interface and index matching fluid was applied to suppress both internal reflection and any reflection from the open (glass) portions of the mask. As would be expected for a fixed mask, the contrast ratio is high. Fig. 5.7 is an enlargement of Fig. 5.6d and shows that the lower limit of the contrast ratio is bounded by the background level, which is approximately 20 dB down.
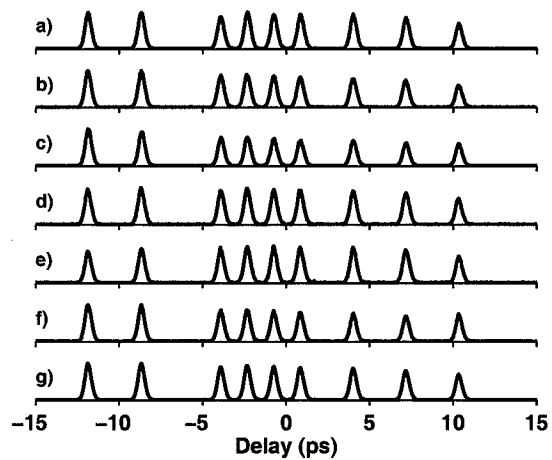
Fig. 5.6. Nearly identical traces from multiple output for the '1010011110101010' pattern mask butt-coupled to the AWG. The input pulse was launched on port 1. Traces (a)-(g) correspond to output on ports 2-8 respectively.
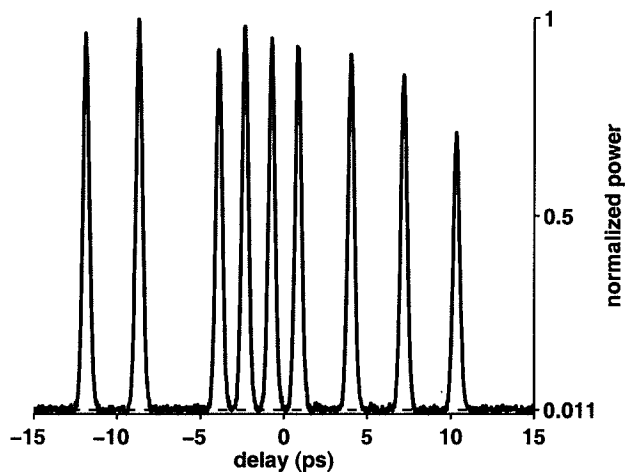
Fig. 5.7. Enlargement of trace (d) in Fig. 5.6 showing the contrast ratio to be ~ 20 dB.

6. REPRODUCING THE AWG SPOT PATTERN AT THE MODULATION PLANE

The simple pulse shaping discussed in Section 5.1 entailed bringing a patterned mask into direct contact with the free-space interface of the AWG. Clearly, in such a system the only way to change the output pulse train is to physically replace the mask with one of a different pattern. In order to be able to more easily reconfigure the output pulse train, an electrically programmable spatial modulator is needed. To accommodate the addition of a modulator, which due to practical limitations cannot be brought into direct contact with the AWG, a simple two-lens unit-magnification telescope is configured to reproduce the free-space interface of the AWG at the focal plane of the telescope. Fig. 6.1 shows the configuration used.
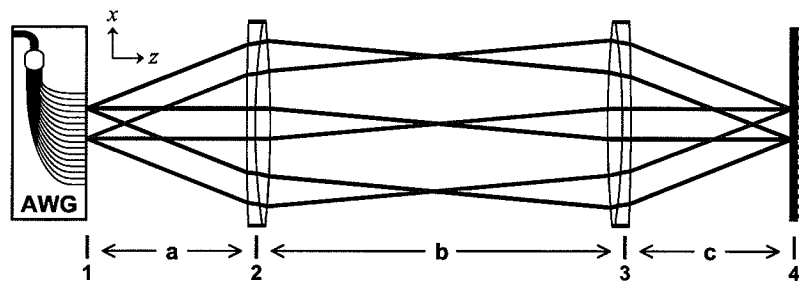
Fig. 6.1. Representation of the 1:1 conjugate telescope. Rays are traced for two of the 16 arrayed waveguides. Plane 1 is the free-space interface of the AWG. Planes 2 and 3 are collimating lenses. Plane 4 is the mirror or modulation plane. Lengths a and c are each 1f, and length b is 2f. The lenses are 40 mm focal length, 15 mm diamater, achromat doublets, #LAI005 from Melles Griot.

Before the incorporation of the mask or modulator into the modified pulse shaper, the telescope was first tested with a gold mirror to verify that the pulse burst genera-

tion functionality of the AWG was preserved. With broadband input power launched on port 5, a spectrally integrated loss of approximately 24 dB was measured at the output on port 4. Comparing this to the 21 dB integrated-loss reported in Section 4.1 (also for ports 5 and 4), it is evident that the addition of the telescope introduces an additional 3 dB loss. It also became apparent from this test that the telescope itself imparts some shape to the envelope of the temporal pulse train. Fig. 6.2 shows a typical pulse train generated using the telescope and mirror configuration of Fig. 6.1. The 'm' shaped envelope evident on the pulse train is an artifact of spherical abberation of the telescope. The effect is particularly pronounced because of the wide field angle of the AWG's 16 free-space outputs, which are spaced at a 150μm pitch. The effect of the abberation is to produce a curvature of the focal plane. For a brief overview of monochromatic aberrations, including field curvature, see Section E.
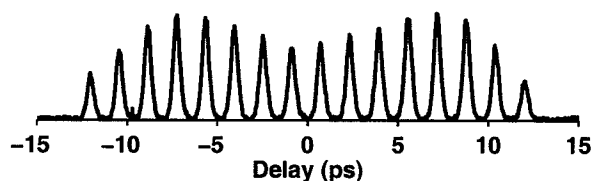
Fig. 6.2. Intensity cross-correlation trace demonstrating the 'm' shaped envelope on the pulse train. The pulse shaper was configured using the 1:1 telescope and gold mirror. Input was on port 5, and output on port 4

To support this analysis, the field curvature was modeled using the Zemax optical software package. Fig. 6.3 shows a ray trace, at the AWG free-space interface (plane 1 in Fig. 6.1), for the case of the return pass of the pulses, after reflection. Ray bundles are shown coupling back into eight of the waveguides. Note that it is necessary to model only half of the 16 waveguides because the AWG is positioned to be reflection-symmetric across the optical axis. In Fig. 6.3 the bottom ray bundle is radially closest to the optical axis ($r = 75\mu$m), corresponding to guide 8 (and 9 by symmetry). The top ray bundle is farthest from the optical axis ($r = 1.125$mm), corresponding to

guide 1 (and 16). As shown by the red dashed line in Fig. 6.3, the focal length is dependent on radial distance from the optical axis. Consequently, the ray bundles do not all reach their focus at the plane of the AWG free-space interface.

When the mirror distance (length c in Fig. 6.1) is changed slightly along the z-axis, the focal positions of the ray bundles at (or near) the free-space interface are also affected. Table 6.1 shows variation in ray bundle RMS spot radius for guides 1-8 as a function of slight changes in mirror displacement (changes in length c). The return-pass spot radius for five different mirror positions was modeled using Zemax. The mirror displacements (changes in length c) used were, 0μm (no displacement), $\pm40\mu$m, and $\pm20\mu$m.
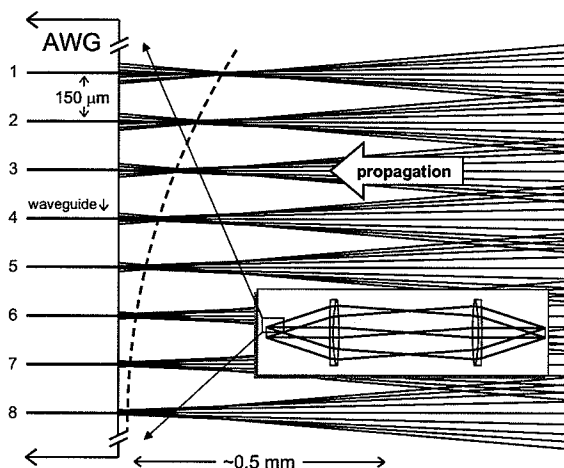
Fig. 6.3. Close up ray trace at the AWG free-space interface on the return pass (i.e. after reflection). Guides 1-8 of the AWG are pictured. The red dashed line approximates the actual focus.

Due to the fact that light must be coupled back into the waveguides to be detected, the return-pass spot sizes at the free-space interface are directly related to the corresponding pulse powers in the output pulse train (recall the one-guide one-pulse analogy). Fig. 6.4 shows rough estimates of relative coupling efficiencies into the waveguides, calculated using the spot sizes from Table 6.1. The estimate is simply given by the inverse spot area, the assumption being that even the most

guide #	Mirror displacement				
	-40μm	-20μm	0μm	20μm	40μm
1	13.0	9.6	6.7	5.0	5.8
2	12.5	9.1	6.3	4.9	6.1
3	11.5	8.2	5.6	4.9	6.7
4	10.1	7.0	5.0	5.4	7.8
5	8.3	5.7	4.9	6.7	9.6
6	6.6	5.1	6.1	8.8	12.1
7	5.7	6.3	8.6	11.7	15.1
8	7.0	9.1	12.0	15.4	18.9

Table 6.1

Return-pass RMS spot radius values (in μm) as a function of mirror displacement along the z-axis, modeled using Zemax. The values shown for guides 1-8 are equivalent to those for guides 16-9 due to the system's reflection symmetry across the optical axis.

tightly focused spot is larger than the mode field diameter of the waveguide. Typical waveguide core dimensions of a conventional AWG are 6 × 6μm, with a relative refractive index difference of 0.7%, between core and cladding. [2] The smallest RMS spot diameter in Table 6.1 is 9.8μm. Additionally, the intensity is assumed to be uniform over the spot.

Fig. 6.4 shows guide-by-guide coupling efficiency estimates for the five different mirror displacements listed in Table 6.1. Plots (a)-(e) in Fig. 6.4 correspond to displacements of -40 through 40μm in Table 6.1. Fig. 6.5 shows intensity cross-correlation data taken with the setup of Fig. 6.1, also using the same five amounts of mirror displacement listed in Table 6.1. Comparing the cross-correlation data in Fig. 6.5 with the estimated coupling efficiency in Fig. 6.4 shows similar changes in the pulse train envelope as a function of mirror position.
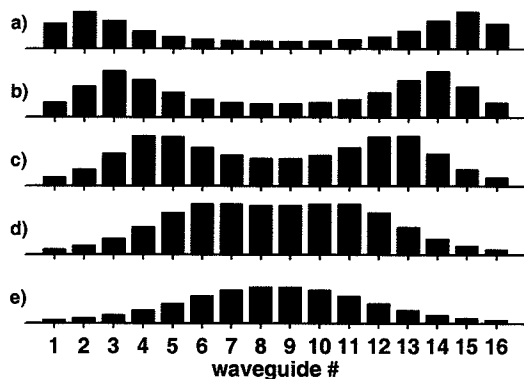
Fig. 6.4. Estimated coupling efficiency into each waveguide for five different mirror positions. Plots (a)-(e) correspond to $-40, -20, 0, 20, 40\mu$m of mirror displacement respectively.
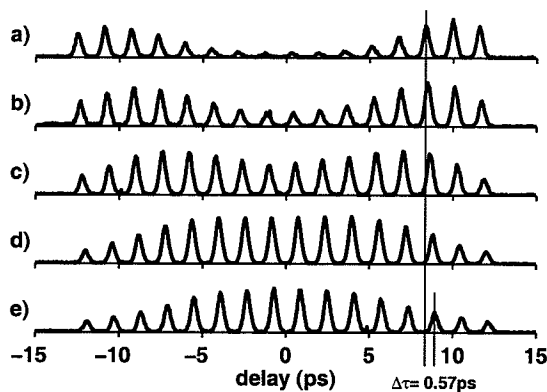
Fig. 6.5. Intensity cross-correlation traces for five different mirror positions. Traces (a)-(e) correspond to $-40, -20, 0, 20, 40\mu$m of mirror displacement respectively.

Another interesting effect which is apparent in Fig. 6.5 is that changing the mirror position (length c in Fig. 6.1) will also time shift the entire pulse train. Clearly, this is due to the fact that the optical path length changes uniformly across all 16 waveguides, creating a uniform delay of the pulses. Comparing traces (a) and (e) in Fig. 6.5, for which there is a difference in mirror displacement of approximately 80μm, a time shift of 0.57ps is observed. This roughly agrees with the expected

0.53ps transit time for a free space length of 160μm (80μm double-passed). The five traces of Fig. 6.5 were taken using the same fiber-coupled input and output ports and without adjusting the cross-correlator configuration, allowing a meaningful comparison of time shifts.

6.1 Pulse Shaping with a Fixed Mask and Telescope

Section 6 discussed the relay optics added to the pulse shaper to reproduce the free-space interface of the AWG at a secondary plane which would enable a mirror, mask, and ultimately spatial modulator to be physically located in the setup. This section discusses the replacement of the mirror in the previous setup (Fig. 6.1) with the spatially patterned mask of Fig. 5.5a, to enable fixed mask pulse shaping with telescope relay optics. The modified setup is shown in Fig. 6.6.
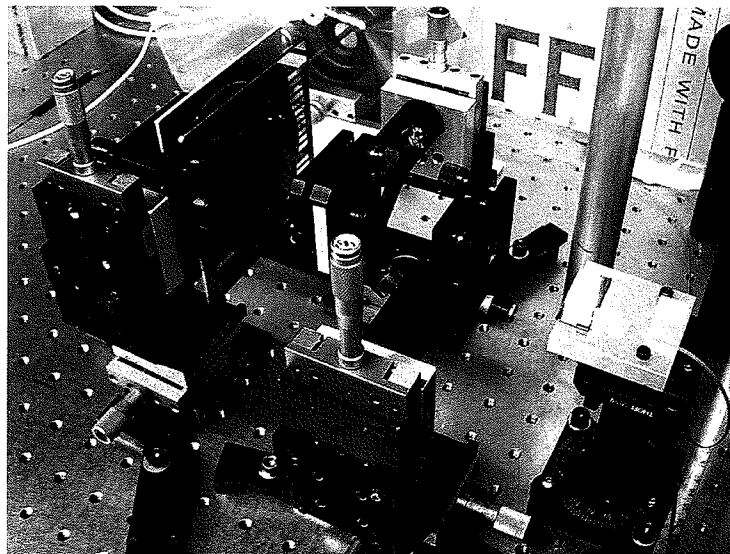
Fig. 6.6. Photograph of the AWG setup with the 1× magnification telescope and fixed spatial mask mounted. The AWG is on the far right and the mask is on the far left, mounted on multiple translation stages (x, y, z, rotation, and 2-axis tilt).

The replacement of the mirror with the spatial mask necessitated a more complicated mount. In addition to the z-axis translation and 2-axis tilt used for the mirror, the spatial mask also required translation and rotation in the x-y plane to enable the selection and centering of a particular mask pattern and to level the pattern in the plane of the AWG.
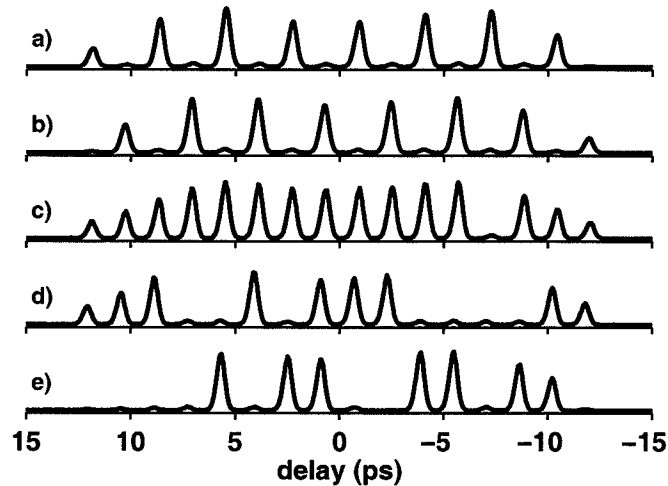
Fig. 6.7. Intensity cross-correlation traces of five different pulse trains taken using the 1× telescope and patterned spatial mask. The traces correspond to spatial masking patterns as follows, (a) 1010101010101010, (b) 0101010101010101, (c) 1111111111110111, (d) 1110010111000011, (e) 0000101100110110.

Fig. 6.7 shows several patterned pulse trains produced with different masking patterns using the setup of Fig. 6.6. Note that the delay axis has been reversed to enable a direct comparison between the spatial masking pattern and the temporal pulse pattern. This is necessary because the telescope inverts the spatial order of the arrayed waveguides at the masking plane, as is evident from Fig. 6.1. The spatial inversion is equivalent to inverting the pulse train in time.

It is apparent from the traces in Fig. 6.7 that the contrast ratio between 'on' and 'off' pulses is not infinite. There is some residual energy present in the 'off' pulses which correspond to the zero bits, or open pixels, of the spatial pattern. To better quantify the contrast ratio, Fig. 6.8a shows a periodic '1010' pulse pattern overlayed on a pattern of all ones (a mirror). The energy in each pulse position was calculated for both traces by first zeroing out the background level and then integrating over each pulse period. The pulse energies of the '1010' pattern were then normalized to

those of the mirror, as shown in Fig. 6.8b. The normalized 'off' pulse energies are a measure of the contrast ratio.
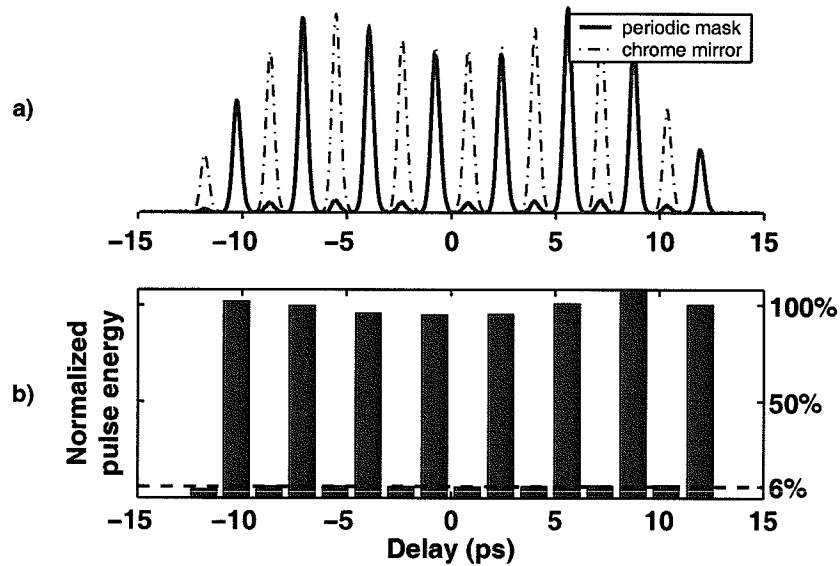
Fig. 6.8. (a) Overlayed cross-correlation traces for a periodic chrome mask and chrome miror. (b) Normalized pulse energies. The dashed red line indicates the average energy of the 'off' pulses.

First, note that the normalized energies for the 'on' pulse positions in the periodic pattern are seen to be nearly 100% as would be expected. The observed slight deviations are likely due to the fact that the process of changing the mask position (from '1010' to '1111') inevitably disturbs the focus, tilt, etc. of the mask mount. The 'off' pulse positions, on the other hand, display an average normalized energy of about 6%, for a contrast ratio of about 12 dB (as compared with the 20 dB reported in Section 5.1 for the butt-coupled mask). This is also to be expected when it is considered that the mask consists of patterned chrome on glass. The chrome is approximately 67% reflective at 1.55μm, while the glass is roughly 4%. Normalizing the glass reflection to that of chrome gives the 6% observed.

Moving the patterned mask along the x-axis (as defined in Fig. 6.1) in increments of 150 μm shifts the spatial pattern by one guide spacing and effectively shifts the

temporal pattern across the pulse train. In Fig. 6.9 a repeating mask pattern of '1110010111000011' is used for five different cases of shift, and the pulse pattern is seen to shift across the pulse train.
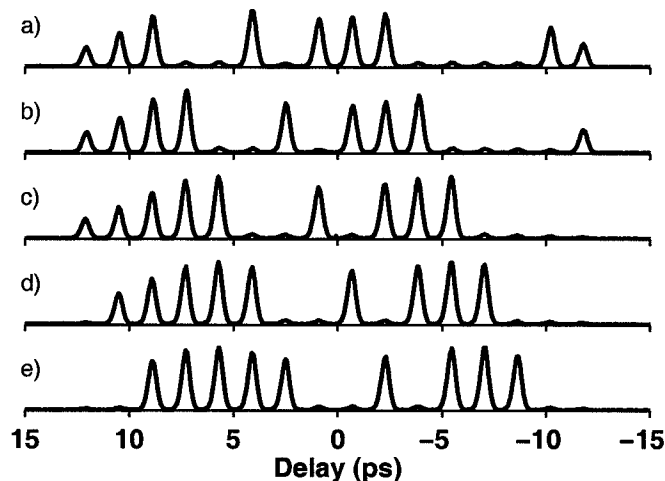
Fig. 6.9. Repeating mask pattern '1110010111000011' shifted along the x-axis in five steps of 150μm.

6.2 Magnifying the AWG pitch

Before the spatial light modulator could be integrated into the direct space-to-time pulse shaper, one additional step was necessary. The spatial light modulator consists of a 1 × 128 array of 100μm wide pixels, while the AWG guide spacing at the free-space interface is 150μm. In order to be able to utilize an integral number of pixels per guide, the guide spacing was stretched to 200μm at the focal plane by adjusting the relay otics magnification to 1.33×. The lenses used in the setup of Fig. 6.1 were retained in this new configuration of Fig. 6.10. The defocusing introduced into the relay optics system in Fig. 6.10 does mean that the system is no longer a 1:1 telescope. Therefore, the Gaussian beam (emitted from any of the AWG guides), after making a round trip through the relay optics and reflector, will not be at a beam waist point when it reaches the AWG free-space interface. The

result is an overall reduction in coupling efficiency across all the waveguides (and equivalently, reduced pulse powers).
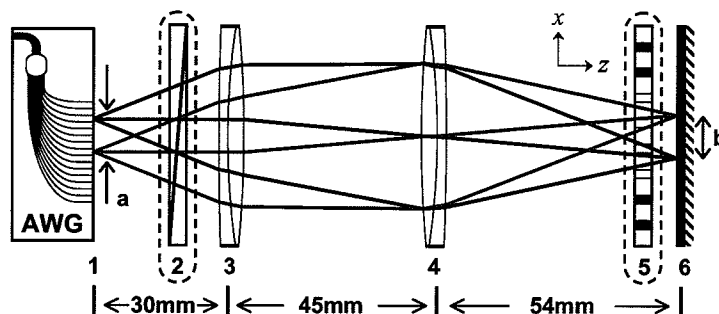
Fig. 6.10. Telescope modified for 1.33× magnification. The AWG guide spacing, $a = 150\mu$m at plane 1, is stretched to 200μm at plane 6. Planes 2 and 5, representing the polarizer and SLM, are grayed out to indicate that they were used for the measurements in Section 7 only.

The magnification of the telescope was tested before inserting the SLM by using a fixed mask with 200μm features. Fig. 6.11 shows the measured pulse trains for 1.33× magnification using a mirror and four different mask patterns. Between traces (d) and (e) in Fig. 6.11 the mask was shifted 200μm along the x-axis. The observed shift of the pulse pattern by one position is confirmation that the guide spacing has been stretched to 200μm.

There was some concern that the aberration introduced by the telescope might cause non uniform coupling to the output ports. However, pulse train measurements were again taken on each output port with nearly identical output as seen in Fig. 6.12.
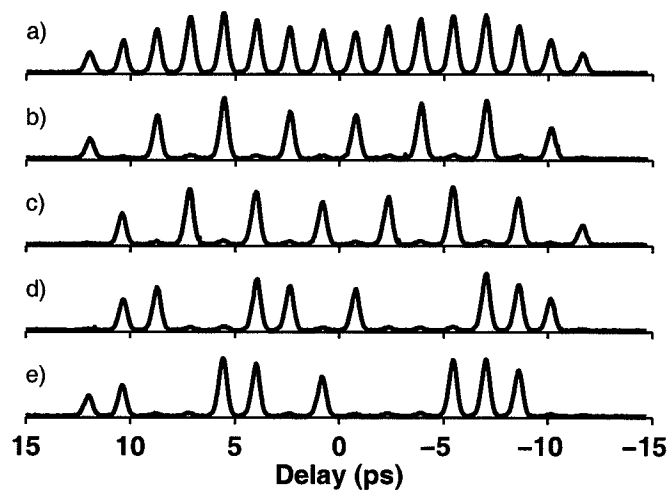
Fig. 6.11. Intensity cross-correlation traces for five masking patterns applied using the 1.33× telescope. The patterns are as follows, (a) mirror, (b) 1010101010101010, (c) 0101010101010101, (d) 0110011010001110, (e) 1100110100011100.
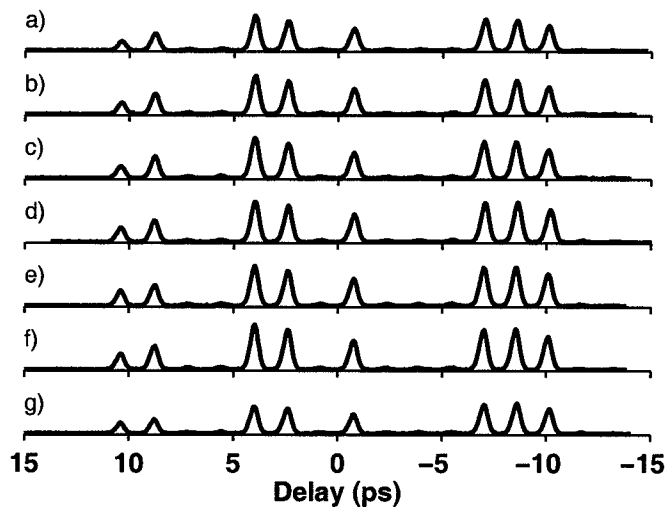
Fig. 6.12. Intensity cross-correlation traces (a)-(e) measured on ports 2-8 respectively with the 1.33× telescope. The masking pattern was 0110011010001110 and input was on port 1.

7. RECONFIGURABLE PULSE SHAPING WITH THE SLM

The spatial light modulator used in these experiments was a 128 pixel two-layer phase and amplitude device from CRI Inc. Each layer contains a thin film of liquid crystal molecules whose axes are aligned with eachother and lie in the x-y plane. When a voltage is applied across the layer, the LC molecules begin to rotate out of the x-y plane, and light polarized along the crystal axis undergoes a phase shift that is dependent on the degree of rotation. The two layers of the device have crystal axes that are misaligned by 90°, both lying in the x-y plane. The combination of these two layers forms a birefringent crystal with the property that the phase of both axes are independently programmable. The addition of a polarizer before the SLM, aligned at 45° to both crystal axes, enables independent phase and amplitude control of each pixel. [28] With the polarizer and SLM included in the 1.33× telescope the setup appears as in Fig. 6.10, with planes 2 and 5 (the polarizer and SLM) included. Due to the thickness of the SLM casing and the thickness of the glass layer in which the liquid crystal is sandwiched, there is a finite separation between plane 5, the modulation plane (i.e. the actual plane of the liquid crystal itself), and plane 6, the reflector. This separation is estimated to be approximately half a millimeter.

Fig. 7.1 shows pulse trains produced using the SLM. Trace *a* was taken with all of the SLM pixels 'open', or transparent, and is comparable to Fig. 6.11a. Traces *b* through *e* demonstrate the reconfigurability of pulse shaping using the SLM. The only differences between these traces were the patterns applied with the SLM. Fig. 7.2 simply shows that each pulse can be selected individually using the SLM.
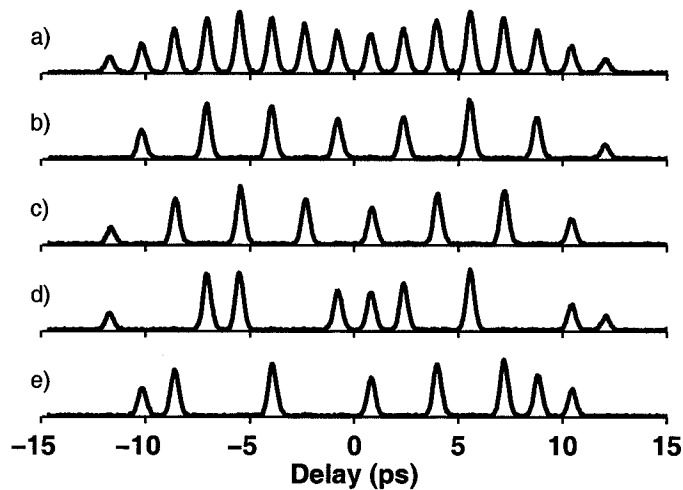
Fig. 7.1. Intensity cross-correlation traces for the pulse shaper and SLM combination. The applied patterns are, (a) all pixels open, (b) 1010101010101010, (c) 0101010101010101, (d) 1001100111010011, (e) 0110010010101110.
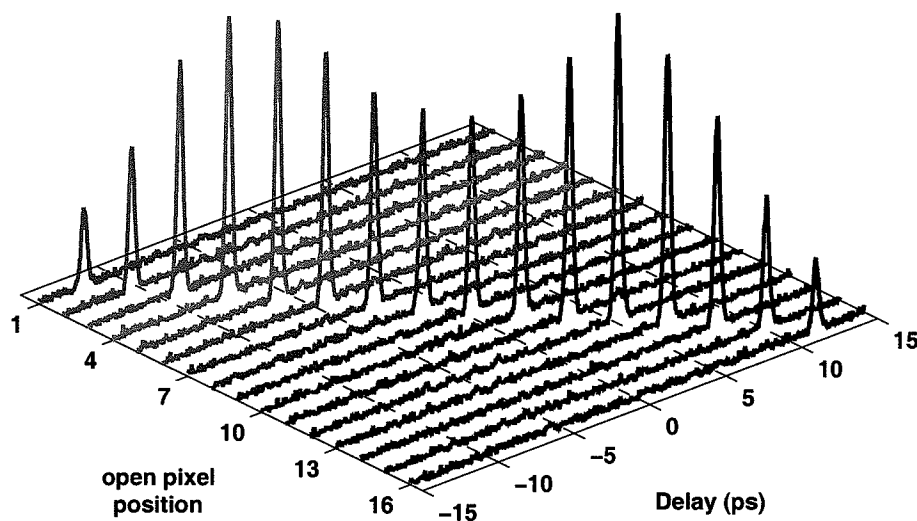
Fig. 7.2. Demonstration of the ability to isolate individual pulses using the SLM.

Fig. 7.3 shows an enlarged version of trace *b* of Fig. 7.1. Some residual power in the 'off' pulses is just detectable above the background level, and the contrast ratio is approximately 14 dB.
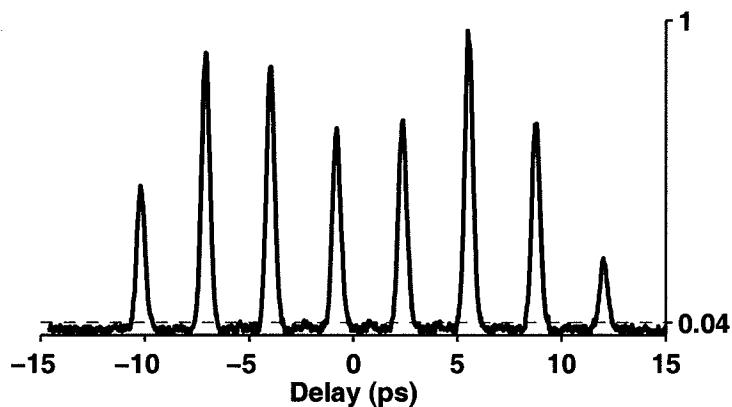
Fig. 7.3. Expanded view of Fig. 7.1b. Contrast ratio $\simeq$ 14 dB.

An attempt was made to flatten the pulse train envelope by eliminating the two weakest pulses on each end of the train (pulses 1, 2, 15, and 16) and reducing the power in the stronger pulses. The result is Fig. 7.4b, where the pulse train has been shortened to 12 pulses with a more nearly flat topped envelope. The strongest pulse has been reduced to about 60% peak power in order to equalize it to the power of the weaker pulses.
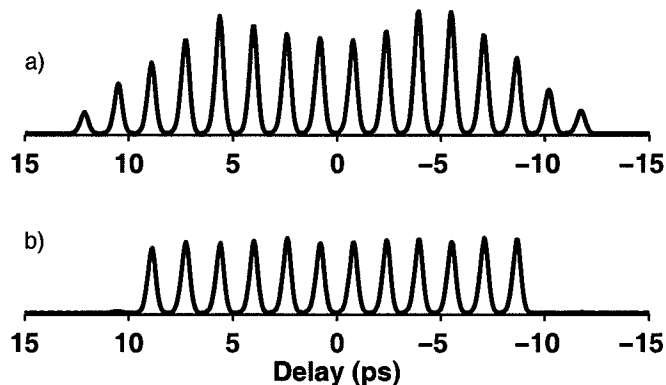
Fig. 7.4. (a) 16-pulse train produced with all SLM pixels 'open', (b) 12-pulse flat topped pulse train generated by suppressing pulses 1, 2, 15, and 16, and scaling the remaining pulses using 'greyscale' (partial transmittance) on the SLM
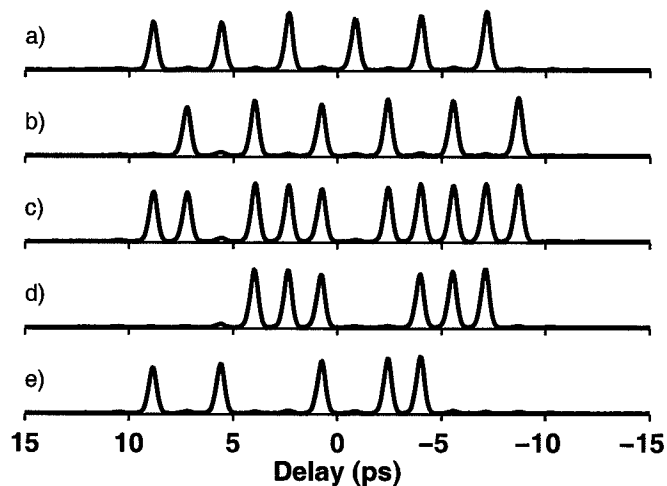
Fig. 7.5. Various 12-bit patterns applied to the flat-topped pulse train. (a) 101010101010 (b) 010101010101 (c) 110111011111 (d) 000111001110 (e) 101001011000

Fig. 7.5 shows 12 pulse traces for equalized and patterned pulse trains. Fig. 7.6 shows an enlarged version of trace *a* of Fig. 7.5. The residual power in the 'off' pulses is more evident than it was in Fig. 7.3. This is in part due to the signal being less noisy (a longer integration time was used for these particular traces), but it is also due to the reduced scale since the pulses have been equalized. Keeping in mind that the peak power has been scaled to $\simeq 60\%$ in Fig. 7.4, the 4% or 14 dB contrast ratio observed for Fig. 7.3 should correspond to a contrast of $6 \sim 7\%$ or about 12 dB, as observed in Fig. 7.6
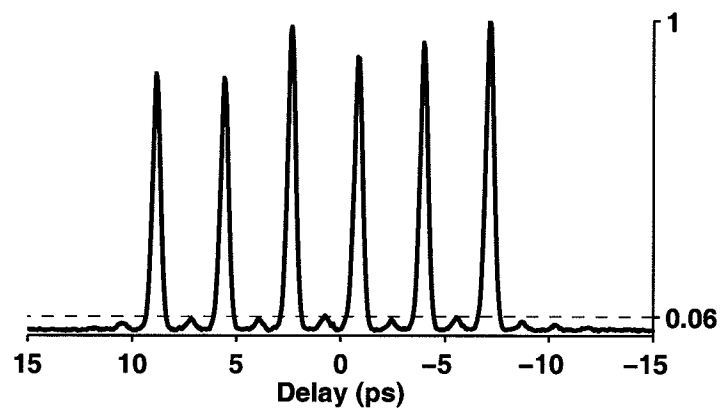
Fig. 7.6. Expanded view of Fig. 7.5(a). Contrast ratio $\simeq$ 12 dB.

8. HIGH SPEED MODULATOR ARRAY

The high speed optoelectronic modulator array is the second key component of the optical word generator. It is intended to replace the liquid crystal SLM used in Fig. 6.10 to enable high speed operation. Potentially, transmission rates of 160 Gb/s could be achieved with a 10 GHz rep-rate short pulse laser source, a 16 guide AWG and a 16 modulator array capable of updating at the laser rep-rate. This application, among others, fuels interest in the development of optoelectronic modulators which meet two requirements, operation in the communications significant 1.55 μm wavelength range, and the capability for on-chip integration to form arrays of multiple devices. The latter requirement focuses attention on surface normal modulators, as opposed to waveguide devices, of which class the asymmetric Fabry-Perot multiple quantum well modulator [35–37] is an important member.[1] Although, at least one group has proposed using 4 waveguide modulators coupled to a 1:4 planar lightwave circuit splitter as an OTDM packet generator. [18]

Electroabsorption based modulators, including the asymmetric Fabry-Perot (AFP) modulator, typically make use of the quantum-confined Stark effect [40] in semiconductor based multiple quantum wells (MQWs) to control optical absorption in the device. Single-pass transmission modulators have been reported [41] which use electroabsorption to reduce transmission of light through the device. This can give good insertion loss, but limited contrast ratio. [37] Double-pass reflection modulators, employing a single high reflector, have also been demonstrated. [42] These devices double the attenuating effect of the absorbing layer by making two passes through it. This represents an improvement over transmission devices, but suffers from the same problems.

---

[1] AFP multi-quantum well modulators have also been reported in waveguide configurations. [39]

The asymmetric Fabry-Perot modulator improves on many of the limitations of transmission and double-pass modulators. [37] This type of modulator is a vertical cavity device which employs the quantum-confined Stark effect (QCSE) to control the absorption of MQW layers situated inside a resonator cavity. [38] By varying absorption inside a Fabry-Perot cavity [43], the modulator shifts the cavity balance through the resonance point, changing the cavity reflection. [44] AFP modulators take advantage of cavity resonance to achieve low insertion loss with a high contrast ratio. [44]

Successful GaAs and AlGaAs based AFP modulators operating in the 0.85-1.0 μm range have been reported by several research groups. [45–47] Some work has also been done in the 1.55 μm range using InGaAs/InP [48] and AlInGaAs [49, 50] material. Modulator arrays based on InGaAs/InP MQWS have been reported, with a 4×4 array of non-resonant transmission devices [51]. An 8×8 array of InGaAs/InP AFP modulators operating at 1.61 μm has also been reported [52]

The second half of this thesis describes the design of an InGaAs/InAlAs MQW based asymmetric Fabry-Perot modulator. It is organized as follows. Section 9 explains the resonance effects of absorbing AFP cavities, and discusses some of the properties of semiconductor quantum wells and their significance to electro-absorption. Section 10 covers the design of an epitaxial semiconductor growth structure and lithographic photomask for the fabrication of modulator devices. Section 11 discusses the experimental methods developed to characterize epitaxial wafers after growth, and diagnose problems. Section 12 includes simulations of expected performance. And Section 13 catalogs optical characterization data take for several wafers grown to date and comments on their limitations.

9. DEVICE EXPLANATION

The asymmetric Fabry-Perot modulator is a reflection mode device with a normally-on high reflection state. The fundamental components of the modulator are the absorption layer, which is the source of modulation, and the Fabry-Perot cavity, which is designed to exploit resonance conditions to enhance the effect of absorption. [37]

9.1 Fabry-Perot cavity

The basic asymmetric Fabry-Perot cavity, shown in Fig. 9.1, consists of a low reflectivity ($R_f \approx 30\%$) front mirror and a high reflectivity ($R_b \approx 99\%$) back mirror. The general expression for the total reflectivity of the cavity at normal incidence is given by Eqn. 9.1 where $\phi = \frac{2\pi n L}{\lambda}$ is the single pass phase. [35,53] [see section A for detail]

$$R = \frac{\left(\sqrt{R_f} - \sqrt{R_b}e^{-\alpha d}\right)^2 + 4\sqrt{R_f R_b}e^{-\alpha d}\sin^2\phi}{\left(1 - \sqrt{R_f R_b}e^{-\alpha d}\right)^2 + 4\sqrt{R_f R_b}e^{-\alpha d}\sin^2\phi} \qquad (9.1)$$

The device is designed with the cavity spacing tuned to resonance at the operating wavelength. The modulator is in the high reflectivity 'on' state when there is no absorption in the cavity ($\alpha = 0$). The 'on' state reflectivity at resonance is given by Eqn. 9.2 and can be quite high due to the asymmetry of the mirrors. [36]

$$R = \frac{\left(\sqrt{R_f} - \sqrt{R_b}\right)^2}{\left(1 - \sqrt{R_f R_b}\right)^2} \qquad (9.2)$$
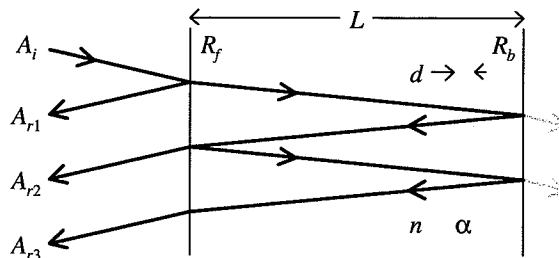
Fig. 9.1. Asymmetric Fabry-Perot with absorption layer

The addition of an absorbing layer (shown as α in Fig. 9.1) in the cavity increases the cavity losses. Adding loss to the cavity is equivalent to reducing the reflectivity of the back mirror R_b. [54] The absorbing layer combined with the back mirror can be thought of as an effective mirror with reduced reflectivity. Seen from the front of the cavity, the effective back mirror reflectivity is given by $R_b^{\text{eff}} = R_b e^{-2\alpha d}$ since the light makes two passes through the absorption layer.

(a)

(b)
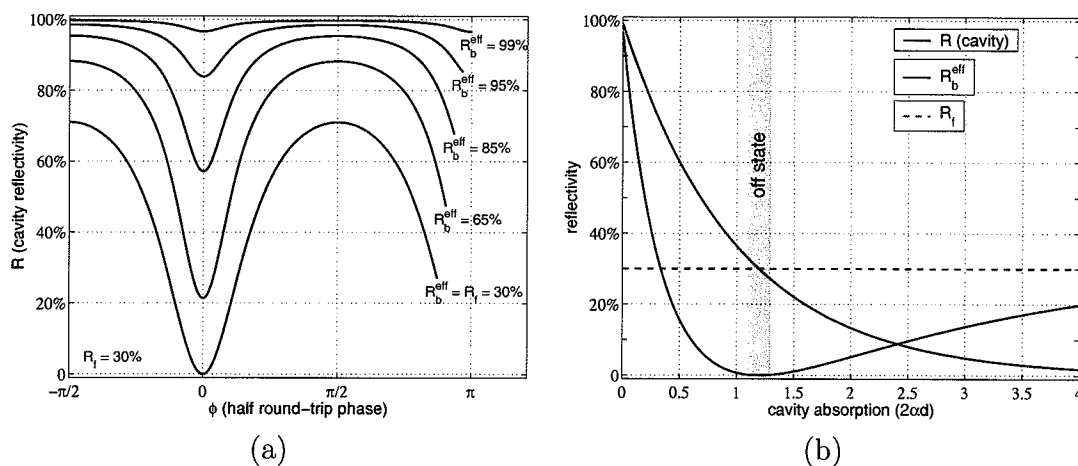
Fig. 9.2. (a) Cavity reflection vs. detuning for different R_b^{eff}. (R_f fixed at 30%). (b) On-resonance cavity reflection, R, and R_b^{eff} as functions of absorption $2\alpha d$. The zero-reflection 'off' condition is highlighted. ($R_f = 30\%$, $R_b = 99\%$)

Turning on absorption in the cavity modifies Eqn. 9.2 by replacing R_b with R_b^{eff}. Zero reflection at resonance is achieved when the mirrors have equal reflectivity. The 'off' state is then $R_f = R_b^{\text{eff}}$ which leads to the condition for the required amount of absorption to reach zero reflection. [35, 37, 55]

$$\alpha d = \ln \sqrt{\frac{R_b}{R_f}} \qquad (9.3)$$

The expression for reflection also appears in the literature as Eqn. 9.4 with an average cavity loss defined as $R_\alpha = \sqrt{R_f R_b} e^{-\alpha d}$. [37]'[see section A for detail]

$$R = \frac{R_f \left(1 - \left(\frac{R_\alpha}{R_f}\right)\right)^2}{(1 - R_\alpha)^2} \qquad (9.4)$$

The effect of reducing the back mirror reflectivity is shown in Fig. 9.2a where the cavity reflectivity is plotted as a function of the detuning for different values of R_b^{eff}. As R_b^{eff} approaches R_f, the overall cavity reflectivity drops until, at the point when the mirrors are matched and the cavity is balanced, the reflectivity goes to zero (at resonance). [56, 57] Since the mirrors are balanced, this is simply the resonance condition for a symmetric cavity. The plot also gives some idea of the wide bandwidth at the on-resonance operating point which is due to the low Finesse of the lossy cavity ($R_f = 30\%$). Fig. 9.2b conveys the same information in another form, showing the on-resonance cavity reflection R and R_b^{eff} as functions of the amount of round-trip absorption $2\alpha d$ in the cavity. The 'off' state is highlighted showing $R \Rightarrow 0$ as $R_b^{\text{eff}} \Rightarrow R_f$ for the critical amount of absorption, $2\alpha d \simeq 1.2$, for this particular cavity ($R_b = 99\%, R_f = 30\%$);

Because this device is a reflection modulator, we would like the 'on' state to be as highly reflective as possible, to minimize insertion loss. In order to achieve good insertion loss, the FP has to be highly asymmetric, with the back mirror as perfect as possible, and with the 'on' state (unbiased) absorption close to zero. We also want the 'off' state reflection to be as close to zero as possible to give a good contrast

ratio. Additionally we would like to minimize the amount of absorption needed to shift from 'on' to 'off' to keep the operating voltage low and ease growth thickness requirements. [37,44] Good contrast ratio requires the 'off' state reflection to be zero, which means the effective back mirror reflection has to equal the front, making the cavity symmetric. This requirement determines the amount of absorption that needs to be turned on during the biased 'off' state. The required amount of absorption is eased by either higher R_f or lower R_b at the expense of insertion loss. When the cavity is balanced $R_b^{\text{eff}} = R_f$ the finesse is determined by the two mirror reflectivities. Lower R_f means lower finesse and a wider bandwidth over the resonance point.

9.2 Cavity Implementation

The previous section outlined the desirable cavity requirements for an Asymmetric Fabry Perot Modulator, high back reflector, low front reflector, and controllable absorption layer, with the cavity tuned to resonance at the operating wavelength. This section describes several possible cavity configurations for such a device based on epitaxial growth for III-V semiconductors, particularly the InAlGaAs on InP system.
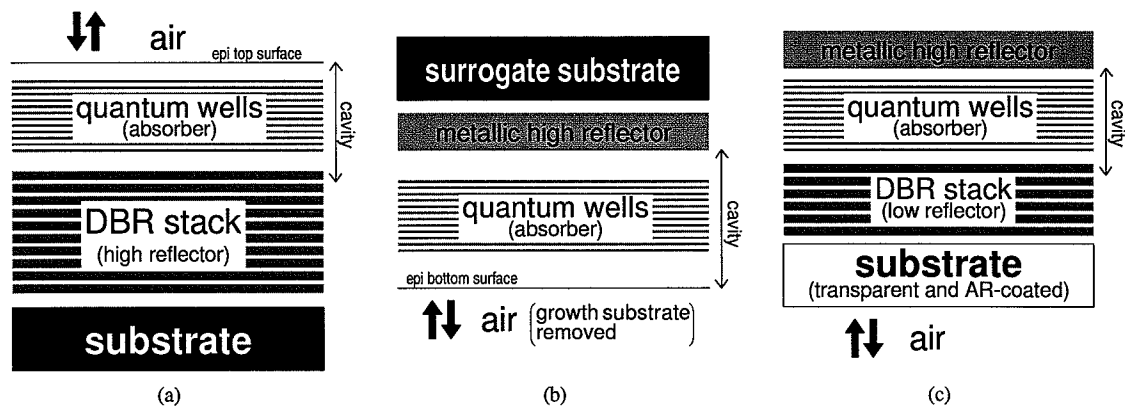
Fig. 9.3. Three possible cavity configurations. (a) thick DBR. (b) no DBR. (c) thin DBR.

Fig. 9.3a shows a cavity implementation which uses a thick distributed Bragg reflector for the back mirror. This design has been popular for devices operating at 850 nm using GaAs substrates (which are opaque in that range). [37,58] The DBR is a multilayer stack of alternating materials of low and high optical index, where each layer is a quarter wavelength thick. For the systems operating at 1.55μm in the InGaAs system we can use a multilayer stack of $In_{.53}Al_{.13}Ga_{.34}As/In_{.52}Al_{.48}As$ layers. With this index variation (3.12 for InAlAs, 3.43 for InAlGaAs) it requires about 40 $\lambda/4$ layers to reach close to 99% reflectivity. This results in a DBR about 9.4μmthick. In this configuration the input is through the top of the structure. The front mirror of the cavity can simply be the semiconductor/air interface which provides about 30% reflectivity for the typical semiconductor index of about 3. This cavity configuration is well suited for materials systems with absorbing substrates, since the optical path never passes through the substrate.

Fig. 9.3b shows a configuration which eliminates the need for a DBR mirror. The high back reflector is instead provided by a metallic mirror deposited on the top of the structure. The structure is then bonded top down to a surrogate substrate, and the original growth substrate is removed from the bottom of the structure. [59] The resulting interface at the bottom of the epi-layer then provides the front mirror, about 30% for the typical semiconductor. This implementation requires less growth time and material, because it eliminates the thick DBR structure. However it increases the level of difficulty of processing because of the bonding and substrate removal which are necessary to form the cavity.

Fig. 9.3c shows a compromise configuration which alleviates some of the problems of the thick DBR in Fig. 9.3a by using a thinner DBR as the low reflectivity front mirror instead of the high reflector. [53] For the InGaAlAs/InAlAs system this means about 8 layers for a 30% mirror. In this structure the high reflector is formed by a deposited metallic mirror as in Fig. 9.3b, but there is no need for substrate removal. Instead, the substrate is required to be transparent at the operating wavelength and an anti-reflection coating is applied to the optically polished bottom of the structure.

This effectively eliminates the substrate from interfering with the cavity design, even though the optical path crosses through it.

There has also been at least one device reported [44] that incorporates two DBR mirrors, one each for the front and back reflectors. This device required a high (76%) front reflector greater than the 30% reflection achievable from the semiconductor:air interface.

9.3 Quantum Wells

To realize the controllable absorption needed for modulation that was described in section 9.1, asymmetric Fabry-Perot modulator designs take advantage of electroabsorption in quantum wells. A quantum well is simply a one-dimensional potential energy well, depicted in Fig. 9.4. A classical particle in this finite potential well is
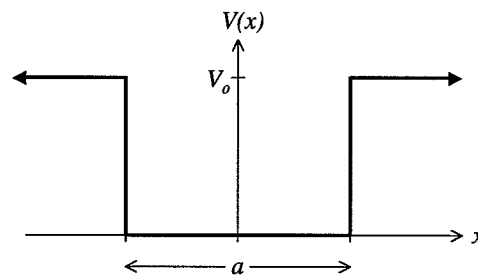
Fig. 9.4. Finite square well potential

trapped as long as its energy does not exceed that of the potential barrier V_0. (For a quantum particle, the wavefunction is localized in the well, but partially tunnels into the barriers.) Unlike a free particle, the energy of a particle trapped in a well is quantized into distinct energy levels. The energy levels for a finite potential well are discussed in section C, but they are qualitatively similar to the simple formula for an infinite potential well, or particle-in-a-box. In particular, a particle in a quan-

tum well has a finite (non-zero) ground state energy. The lowest energy state of a particle-in-a-box is given by [60]

$$E = \frac{\pi^2 \hbar^2}{2ma^2} \tag{9.5}$$

where m is the particle mass and a is the well width. Briefly, this is a consequence of the Heisenberg uncertainty principle $\Delta p \Delta x \geq \hbar/2$ which requires the product of uncertainties in position and momentum to always be greater than or equal to the constant $\hbar/2$. For a trapped particle, whose wavefunction is localized in the well, there is a restriction on its position uncertainty, $\Delta x \simeq a$. This means the uncertainty in momentum, $\Delta p \geq \hbar/(2a)$, is non-zero and therefore the particle must have a non-zero energy. [60]

Quantum wells can be formed with III-V semiconductor heterojunctions, such as $In_{.53}Ga_{.47}As$ and $In_{.52}Al_{.48}As$, because these materials have different energy gaps between their valence and conduction bands. A layer of narrow bandgap material forms the well and is sandwiched between layers of wider bandgap material which form the potential barriers. Modern crystal growth technologies, like molecular beam epitaxy, enable the growth scientist to tightly control the thickness and material composition of each crystal layer as it is being grown. Typical well and barrier layer thicknesses are on the order of 100Å. Adjusting the mole fractions of ternary alloys, such as $In_{.52}Al_{.48}As$ and $In_{.53}Ga_{.47}As$, allows the grower to tailor the lattice constants to match between well and barrier materials. This lattice matching makes it possible to grow alternating layers of different materials while maintaining the perfect crystal structure throughout.

9.3.1 Quantum Confinement

In a bulk semiconductor, an absorption event is the creation of an electron-hole pair through the absorption of a photon resulting in an electron elevated to the conduction band and a hole created in the valence band. As shown by Eqn. 9.5, an electron (or hole) in a quantum well has an elevated ground state, above the energy

level of the well bottom. This means that in a quantum well, an absorption event requires more energy since the electron (hole) must be elevated to an energy 'higher' than the conduction (valence) band level. For a quantum well, the effective bandgap is increased over that of a bulk semiconductor of the same material. Specifically, it is increased by an amount equal to the combined elevated ground states of the electron and hole. This effect is known as quantum confinement and is dependent on the width of the quantum well and the barrier height, as explained further in section C. [40, 61]

9.3.2 Exciton
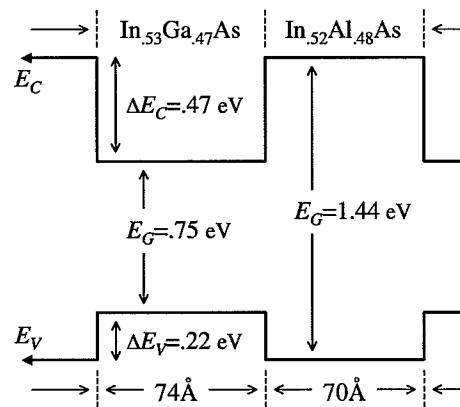
Fig. 9.5. $In_{.53}Ga_{.47}As/In_{.52}Al_{.48}As$ quantum well energy band diagram

The band diagram for a $In_{.53}Ga_{.47}As/In_{.52}Al_{.48}As$ heterojunction is shown in Fig. 9.5. For InGaAs/InAlAs as well as other optically interesting III-V heterojunctions, such as GaAs/AlGaAs and InGaAs/InP, the conduction and valence bands line up in such a way that the bands of the narrow gap material are 'inside' those of the wider gap material. In other words the valence band of $In_{.53}Ga_{.47}As$ is above that of $In_{.52}Al_{.48}As$, while for the conduction band the situation is reversed. This type of band offset results in both electrons and holes seeing a quantum well and becoming trapped in the same physical layer. In this situation the electron and hole experience

a strong Coulomb attraction and form a hydrogen-atom-like pair, called an exciton. One effect of the exciton is that it causes a small correction to the calculation of the effective bandgap for a quantum well. The bandgap is slightly reduced by an amount equal to the binding energy of the exciton [62]

$$E = \frac{\mu_{\text{eff}} e^4}{8h^2 \epsilon_r^2 \epsilon_0^2} \tag{9.6}$$

where μ_{eff} is the reduced effective mass of the hole and electron. More importantly, the exciton has a strong absorption peak, which enhances the absorption (of the well) at the band-edge. It should be noted that excitons have also been observed in bulk semiconductors under the right conditions, such as low temperature, but that their creation is significantly enhanced in quantum wells where the electron and hole are confined to a thin layer. [40]

9.3.3 Stark shift

The above section has explained two effects of quantum wells, quantum confinement resulting in elevated bangap, and the creation of excitons and their related absorption peak. For the AFP modulator application however, the most significant properties of quantum wells are exhibited when an electric field is applied perpendicular to the well layers. The electric field applied across a semiconductor causes the energy bands to bend, as shown in Fig. 9.6. This results in several related effects. First, the quantum confinement is reduced since the potential barriers are lowered on one side, this lowers the ground state energy, decreasing the effective bandgap. Second, the electron and hole will be pulled to opposite sides of the quantum well, decreasing the binding energy of the exciton. Finally, if the particles tunnel through the barrier, they will be swept away to opposite sides (due to the potential), destroying the exciton. [40] The probability of tunnelling is increased with an applied field because of the reduced quantum confinement. This reduces the lifetime of the exciton, resulting in a lifetime broadening of the absorption peak (also an uncertainty effect) and reduction in absorption at the peak (due to broadening). In a
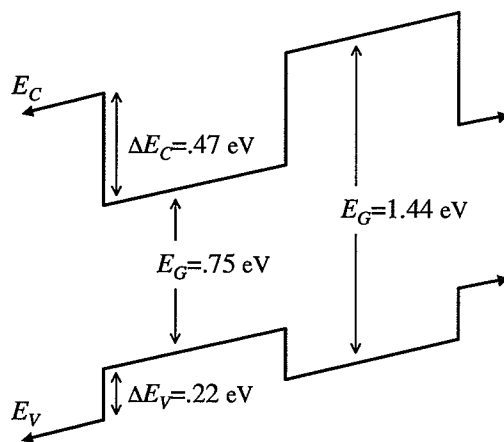
Fig. 9.6. Energy band bending under applied field

bulk semiconductor, this broadening and weakening of the exciton quickly lead to the exciton absorption peak being completely washed out. However, in a quantum well, because the electron and hole are confined (at least partially) in the well layer, the broadening and weakening of the exciton is much reduced over that of the bulk semiconductor. [40] Therefore a strong exciton absorption peak is still resolvable even under fields of the order of 10^7 V/m. The combined effect of the above, is that as the electric field is applied perpendicular to the wells, the absorption peak and band edge red-shift to longer wavelengths, and the peak also broadens somewhat. This is known as the quantum confined Stark effect [40] and this is exactly the absorption characteristic needed in the AFP modulator.

By designing the cavity resonance slightly to the red of the absorption edge, it is then possible to shift the absorption edge into the resonance range using an applied field. In this way, the AFP modulator's low absorption state is achieved under zero bias, with the absorption increasing with applied field.

10. GROWTH STRUCTURE AND DEVICE DESIGN

The epi-layer structure of the modulator cavity is shown in Fig. 10.1. This design is of type c as shown in Fig. 9.3, using a metallic back reflector and buried DBR front reflector. The materials chosen for the well and barrier layers of the MQWs were InGaAs and InAlAs respectively. The finite square well potential (solved in Section C), was used to calculate the quantum well thicknesses necessary to place the expected exciton peak at ~ 1550 nm. The thickness and alloy compositions are shown in Fig. 10.1.

The materials chosen for the DBR were InAlAs and InAlGaAs. The DBR reflectivity was modelled using the characteristic matrix method, to determine suitable thicknesses for the layers. The characteristic matrix [M], given by Eqn. 10.1, of a thin film layer contains all the information necessary to calculate the reflectivity of that layer.

$$[M] = \begin{bmatrix} \cos(kd) & -i\eta \sin(kd) \\ \frac{-i}{\eta} \sin(kd) & \cos(kd) \end{bmatrix}$$

(10.1)

$In_{.53}Ga_{.47}As$	Be doped p-contacting layer	300Å
$In_{.52}Al_{.48}As$	p-type spacer	3500Å
	intrinsic quantum well region	80 periods
$In_{.53}Ga_{.47}As$	wells	74Å
$In_{.52}Al_{.48}As$	barriers	70Å
$In_{.52}Al_{.48}As$	n-type spacer	3000Å
	undoped DBR	8 periods
$In_{.52}Al_{.48}As$	quarter wavelength layer	1219Å
$In_{.53}Al_{.13}Ga_{.34}As$	quarter wavelength layer	1138Å
InP	semi-insulating substrate	

Fig. 10.1. Epi-layer growth structure with low-reflectivity DBR
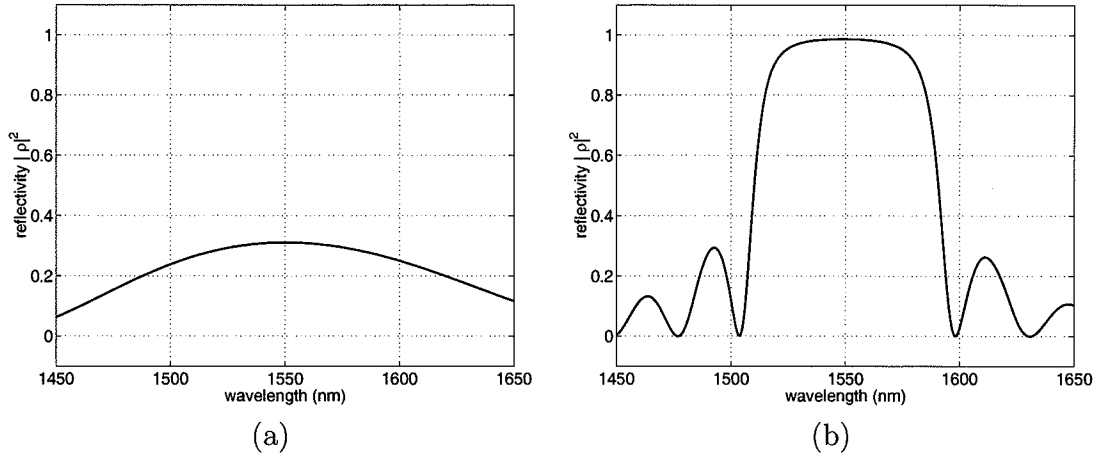
Fig. 10.2. (a) 8 period InAlAs/InAlGaAs DBR $\lambda/4$ stack (1.9μm thick), (b) 40 period InAlAs/InAlGaAs DBR (9.4μm thick)

where η, k, and d are the characteristic impedence, wave vector, and thickness of the layer. The transfer matrix method, reviewed in section B, combines the characteristic matrices of a system of thin films to calculate the total reflectivity of the system.

We have used the transfer matrix method to model the quarter wavelength multilayer stack of Fig. 10.1. The reflectivity of this eight period InAlAs/InAlGaAs DBR is shown in Fig. 10.2a. For comparison, the reflectivity for a 40 period DBR of the same material is shown in Fig. 10.2b. The eight period reflector gives 30% reflection at 1.55 μm and is 1.9 μm thick. This makes the total thickness of the cavity structure about 3.7 μm.

In order to maximize the field across the quantum wells for a given applied voltage, the wells are grown in the intrinsic region of a p-i-n diode. When the diode is reverse biased, the quantum wells form the depletion region and a large voltage drop across the wells can be obtained without significant current flow. [40] These p and n-type InAlAs spacer regions are shown in Fig. 10.1. Ultimately these layers will need to be electrically contacted from off-chip so the thicknesses are chosen to be 3000 Å or more to make the process of contacting easier.

Fig. 10.3 shows cross-sectional and top-down views of the fabricated modulator as designed. The modulator is designed to be optically accessed through the substrate, with the DBR as the front reflector and the gold mirror as the back reflector of the cavity. The quantum well region and p-i-n diode are shown with contacts deposited to give off-chip electrical access to the device.
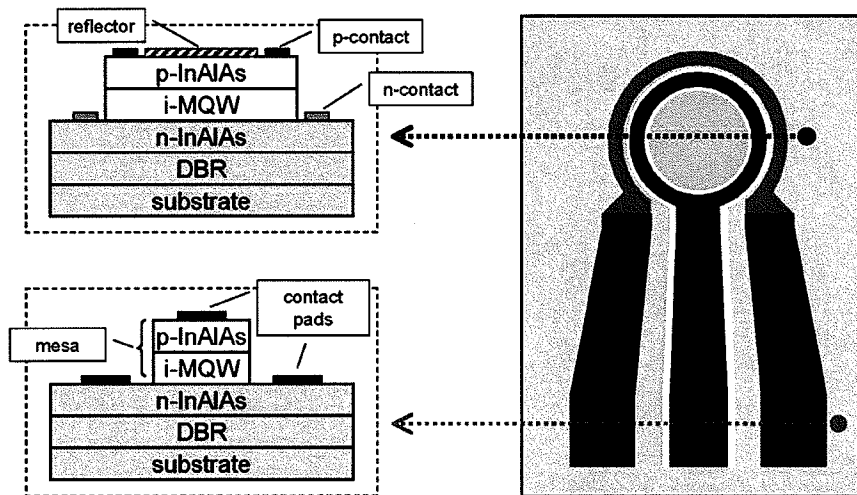
Fig. 10.3. (top left) Cross section of the device active area. (bottom left) Cross section of the electrical contacting pad area. (right) Top-down view of a device. The gold colored active area is 150 μm in diameter.

Fig. 10.4 shows the photomask[1] that was designed for device fabrication. Several different sizes of modulators, ranging from 10 to 300 μm in active region diameter were included on the mask, as well as test patterns for electrical contacts. The redundancy of elements on the mask design will allow us to test several different devices sizes.

---

[1]Mask design and layout were done by Albert Vega using the WaveMaker software package
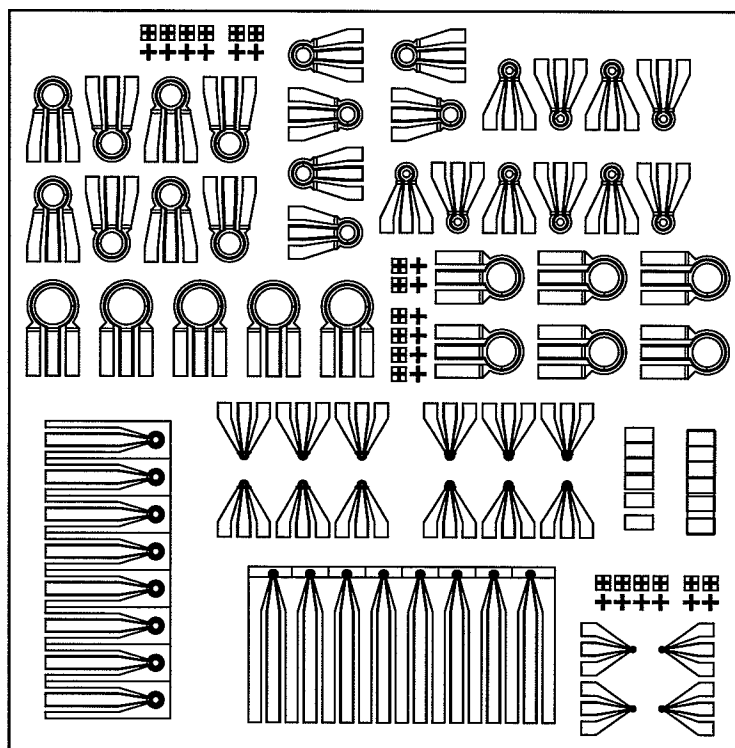
Fig. 10.4. Modulator photomask layout ($\sim 5 \times 5$ mm)

11. EXPERIMENTAL METHODS

In order to characterize the optical properties of the semiconductor wafers grown and to diagnose problems, an optical characterization setup was built. The setup is a spectrometer enabling measurements of transmitted and reflected light for the wafer under test. A diagram of the setup is shown in Fig. 11.1. It consists of a black body kilowatt white light source, a monochromator, chopper, and two InGaAs photodetectors (Thorlabs PDA-400). The semiconductor wafer sample is placed at a focal point of the chromatically filtered and chopped beam. Its normal is rotated off the optical axis by a slight angle so that the reflected beam can be captured. By incrementally stepping the monochromator and detecting the chopped optical beams with a lock-in amplifier, this setup is able to capture wafer transmission and reflection data as a function of wavelength over the range of 1300 - 1700 nm (beyond 1700 nm the photodetector sensitivity dies off).
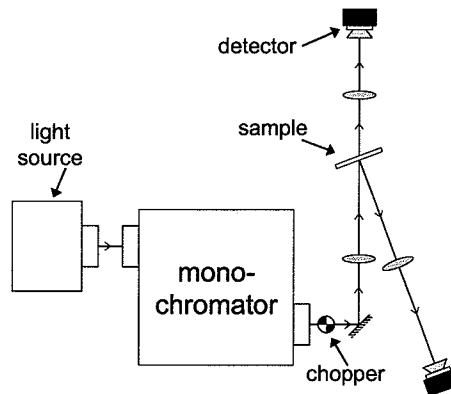
Fig. 11.1. Optical characterization setup

In addition to this characterization capability developed in-house, the epitaxial semiconductor growth vendor contracted to grow the wafers was able to supply a

limited amount of optical data as well. This consisted of transmission-only data over a range of 1.3 - 2.4 μm, which augmented the overall range available for optical characterization of the wafers.

As discussed in Section 9.1, the AFPM modulator is a resonant cavity device, and its modulation mechanism relies on the spectral alignment of two critical optical features. These are the reflection peak of the DBR stack, and the absorption edge of the MQW layers. Methods were developed to characterize these two properties for the wafers grown. The wafer absorption can be obtained by first measuring transmission and reflection with the spectrometer of Fig. 11.1. The wafer absorption is then found by $A = 1 - (T + R)$. Typical absorption curves display a recognizable absorption edge which is easily observed. Fig. 11.2 shows the spectral absorption for a typical wafer grown with the full device structure (structure shown in Fig. 10.1).
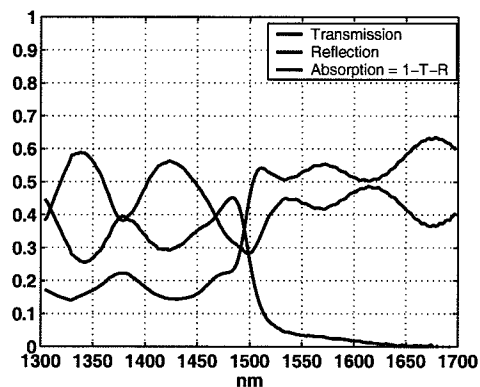
Fig. 11.2. Transmission, reflection and absorption spectra for a typical wafer grown with the full device structure. (OSemi growth #S203-18)

Determining the spectral response of the DBR stack is more difficult. Simply measuring the wafer reflection using the spectrometer in Fig. 11.1, will not yield the DBR response. Fig. 11.3a shows the predicted reflection spectrum for the DBR modelled by itself, while Fig. 11.3b shows the modelled reflection (as well as transmission and absorption) for the full wafer structure (substrate + all epi-layers). It is difficult to deduce the DBR response with any kind of certainty based on the wafer response.
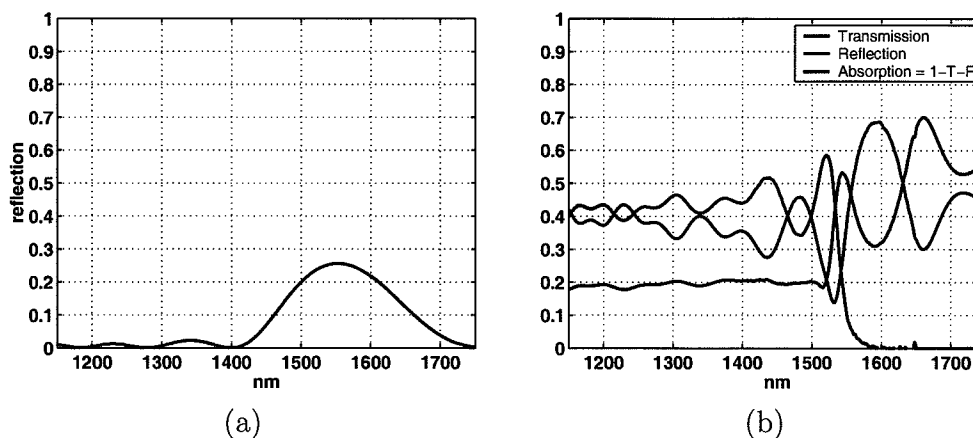
Fig. 11.3. (a) Modelled reflection of the stand-alone DBR. (b) Modelled spectral response of the full wafer structure. (structure shown in Fig. 10.1)

This difference in reflection is due to two primary factors. First, the absorption of the MQW layers obscures the reflection of the DBR. Second, even neglecting absorption, the growth structure consists of many layers with multiple reflections, which interfere with eachother. Reflections from three surfaces in particular are significant. These are the air/substrate reflection, the reflection from the DBR itself, and the epilayer/air reflection (assuming the wafer is placed substrate first in the spectrometer). The reflectivities are roughly equal in strength, each approximately 30%.
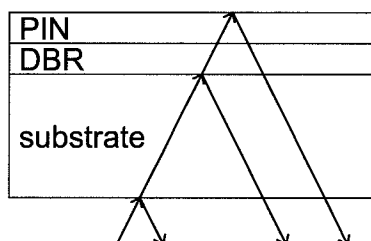
Fig. 11.4. Cross-section of the wafer structure showing the three reflections whose interference largely determines the total wafer reflection
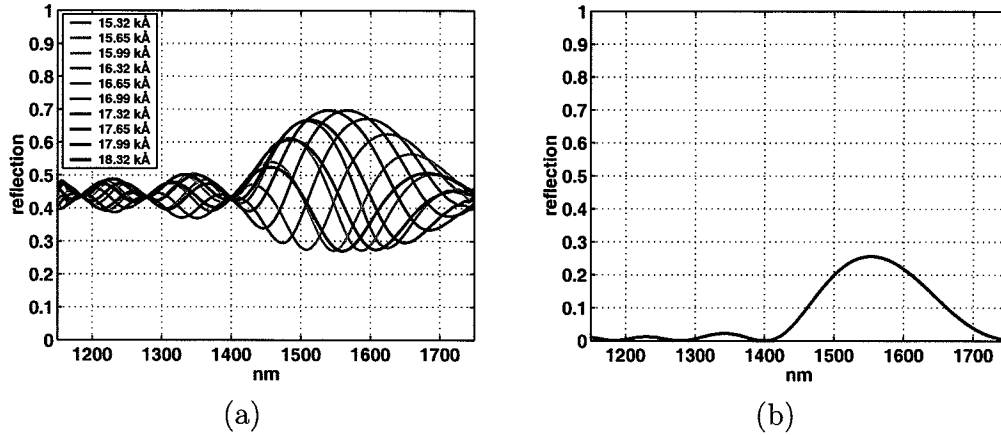
Fig. 11.5. (a) Modelled reflection spectra of the wafer structure after removal of the MQW layers, and for subsequent shallow etches. (b) Modelled reflection of the stand-alone DBR.

For a resonant cavity of length L and index n, the roundtrip phase is given by $\phi = 2\pi \times \frac{2nL}{\lambda}$. For $\lambda_2 = \lambda_1 + \Delta\lambda$, an interference fringe of width $\Delta\lambda$ is observed when $\phi_2 - \phi_1 = 2\pi$. The InP substrate is nominally 500 μm thick with a refractive index of roughly 3. This means that any interference fringes due to the substrate cavity (i.e. mirrors formed by air/substrate and DBR) will be less than 1 nm wide and will be unresolvable with the spectrometer setup (the resolution of the spectrometer is at best 1 nm). Therefore, the contribution of the air/substrate reflection is simply to uniformly increase the total reflection by about 30% (a constant offset).

The cavity formed between the DBR and the epi-layer/air interface, however, is much shorter, on the order of $1.8 \sim 3.7$ μm (it is not well defined since the DBR is not an abrupt interface). The Fabry-Perot fringes due to this cavity are on the order of ~ 100 nm and will significantly impact the total wafer reflection observed by the spectrometer setup in Fig. 11.1. Due to the multiple interfaces and the distributed nature of their reflections, they are best modelled using the transfer matrix approach discussed in more detail in Section B.

The following approach was developed to characterize the DBR response of a wafer. First the MQW layers are etched away, leaving the DBR and n-spacer layer.

This removes the absorbing material, eliminating the effect of absorption obscuring the reflection. The spectral reflection of the wafer is then measured. Next the DBR-to-air cavity is slightly shortened through a second shallower etch of ~ 200 Å, and the spectral reflection is measured again. These last two steps of shortening the cavity and measuring the reflection spectrum are repeated several times. The effect of shortening the cavity is to shift the Fabry-Perot fringes observed in the reflection spectrum. When several spectra with shifted fringes are superimposed, an envelope develops which is related to the stand-alone response of the DBR. This effect is shown in Fig. 11.5a where an envelope can be seen that is clearly related to the response of the DBR shown in Fig. 11.5b. The offset between the envelope and DBR response is largely due to the reflection from the air/substrate interface.
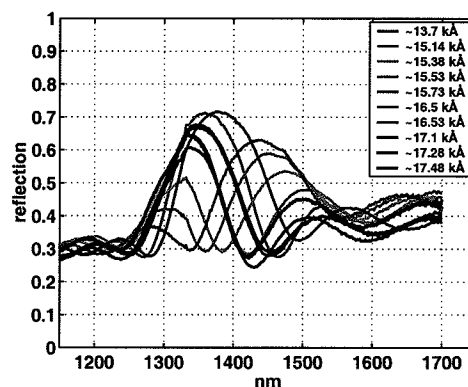
Fig. 11.6. Reflection spectra taken after multiple etches were performed on a sample of the same wafer used in Fig. 11.2.

Fig. 11.6 shows the results of this multi-etch process being carried out. The sample used to obtain this data was from the same wafer that was used to obtain the spectral responses shown in Fig. 11.2. Judging solely from the spectra of Fig. 11.2 it is not clear where the DBR resonance peak lies. However, with the data in Fig. 11.6 the peak resonance can be seen to be a little below 1400 nm, clearly far from the target resonance of 1550 nm.

12. SIMULATION

To help in evaluating the design of the growth structure shown in Fig. 10.1, we used existing absorption data taken from an earlier growth to model the expected device reflectivity. The structure of the earlier growth is shown in Fig. 12.1 and is essentially the same as the structure already shown in Fig. 10.1, but without the DBR layers. The key issue concerning the absorption data is that the MQW regions of the two structures are identical. The absorption measured for the earlier growth is shown in Fig. 12.2.

By extending the characteristic matrix model to cover the entire cavity structure of Fig. 10.1 plus a deposited back reflector, and also including absorption data taken from the first growth sample, we modelled the expected performance of the devices shown in Fig. 10.3. We used the measured unbiased absorption data of Fig. 12.2 and then artificially red-shifted it to simulate an applied bias as shown in Fig. 12.3a. The conversion from transmission to absorption coefficient is given by

$$\alpha = -\frac{1}{d} \ln \frac{I}{I_0}$$

The absorption coefficient calculated in this way is artificially high due to reflection loss in the transmission measurement. Therefore the coefficient was DC shifted

$In_{.52}Al_{.48}As$	p-type spacer	1000Å
	intrinsic quantum well region	80 periods
$In_{.53}Ga_{.47}As$	wells	74Å
$In_{.52}Al_{.48}As$	barriers	70Å
$In_{.52}Al_{.48}As$	n-type spacer	2933Å
InP	n-type substrate	

Fig. 12.1. Epi-layer growth structure
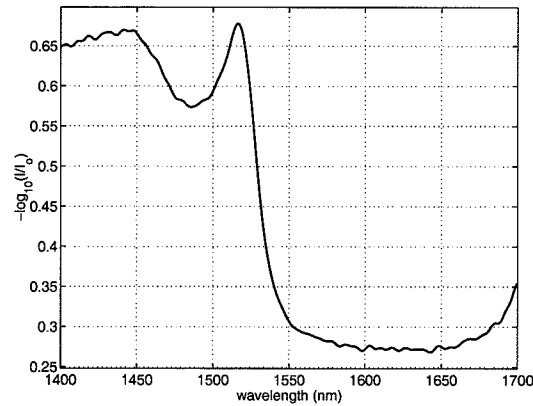
Fig. 12.2. Zero bias absorption curve from initial growth (structure
of Fig. 12.1). The growth was carried out using a molecular beam
epitaxy reactor in the Solid State Laboratories of Purdue University
by Professor Mike Melloch.

(a)   (b)
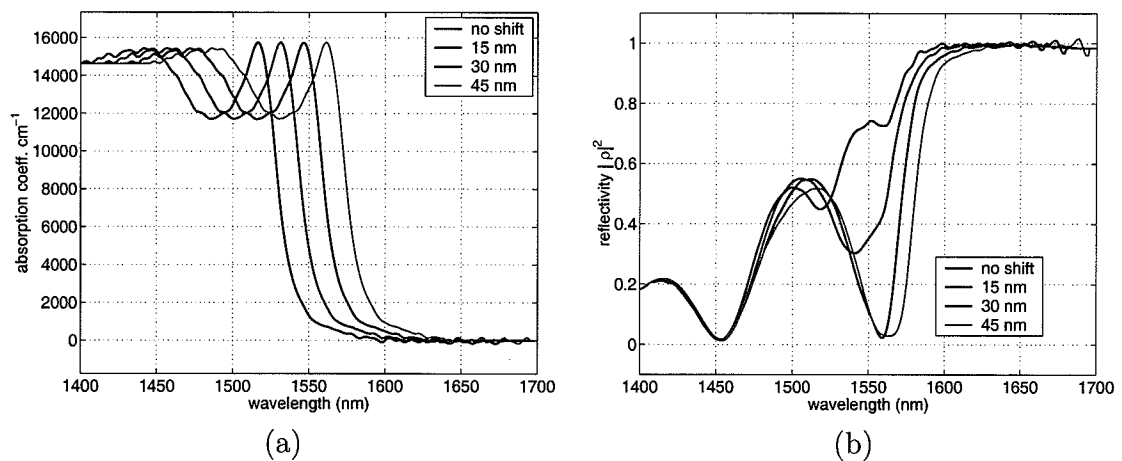
Fig. 12.3. (a) Artificially shifted absorption spectra used in model,
(b) Reflectivity of the cavity model for different absorption shifts

so that it would zero out around 1.65μm. This was done to reflect the negligible
absorption expected for wavelengths well above the absorption edge.

The absorption coefficient data in Fig. 12.3a were used to calculate the imaginary
part of the refractive index of the InGaAs quantum well layers given by [63]

$$n_i = \frac{\lambda\alpha}{4\pi}$$

This imaginary refractive index was then included in the characteristic matrix for the InGaAs layers to take into account the effect of absorption in the model. The results of the transfer matrix calculation are shown in Fig. 12.3b, which shows the reflectivity of the device for different absorption shifts. The dark blue line shows the unbiased case for high reflectivity. The red line shows the reflectivity dropping nearly to zero under a simulated absorption shift of 30 nm.
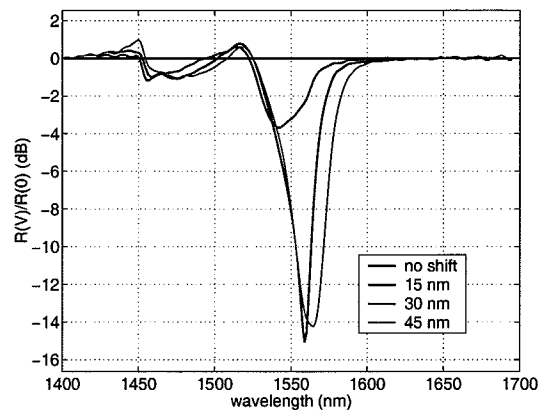
Fig. 12.4. Contrast ratio for different absorption shifts

Fig. 12.4 shows the contrast ratio in dB for the reflection change, $10 \times \log_{10}(R_{bias}/R_0)$. This model predicts an approximately 14 dB contrast ratio for a 35 nm shift in the absorption spectrum.

13. CATALOG OF CHARACTERIZED WAFERS

The following is a catalog of characterizations performed on four wafers grown over a period of about a year. These wafers were procured under a grant from the Photonics Technology Access Program administered by the Optoelectronics Industry Development Association. They were grown by OSemi Incorporated at their facility in Rochester, MN. During this period other test wafers were also grown which did not contain the full epitaxial structure shown in Fig. 10.1. These test wafers were grown in attempts to calibrate various aspects of the growth process but were never intended to be operational modulators, and so are not shown here.

Fig. 13.1 shows data taken for wafer #S203-18 grown on 6/6/2003. This wafer, and the procedure used to obtain the DBR reflection envelope were discussed in Section 11. This wafer had an absorption peak near 1490 nm which is near the design target, but the DBR resonance peak was just short of 1400 nm, which was too far from the design point of 1550 nm.

Fig. 13.2 shows data taken for wafer #S203-42 grown on 7/3/2003. The absorption peak is again near 1490 nm as with #S203-18, but with this wafer the DBR resonance is much more on target, near 1550nm. This wafer displayed the best optical properties of any of the four because the MQW absorption and DBR resonance were fairly well aligned and close to the target. However several attempts to make ohmic contact to this wafer, using variations of Ti:Au, Ti:Pt:Au, and Zn:Au, were not successful.

Fig. 13.3 shows data taken for wafer #S203-51 grown on 10/9/03. The absorption peak was found to be near 1580 nm, which puts the absorption edge too far past the target of 1550 nm to be useful. Fig. 13.3b shows transmission data supplied by OSemi Inc. (using an FTIR, Fourier transform infra-red spectrometer, at their site). This
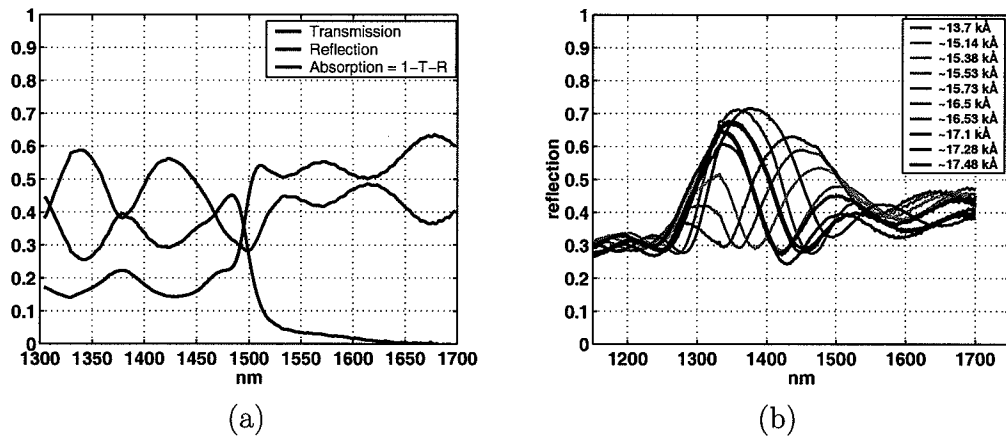
Fig. 13.1. (a) Wafer #S203-18. Transmission, reflection and absorption spectra. (b) Reflection spectra taken between multiple shallow etches after removal of the MQW region.
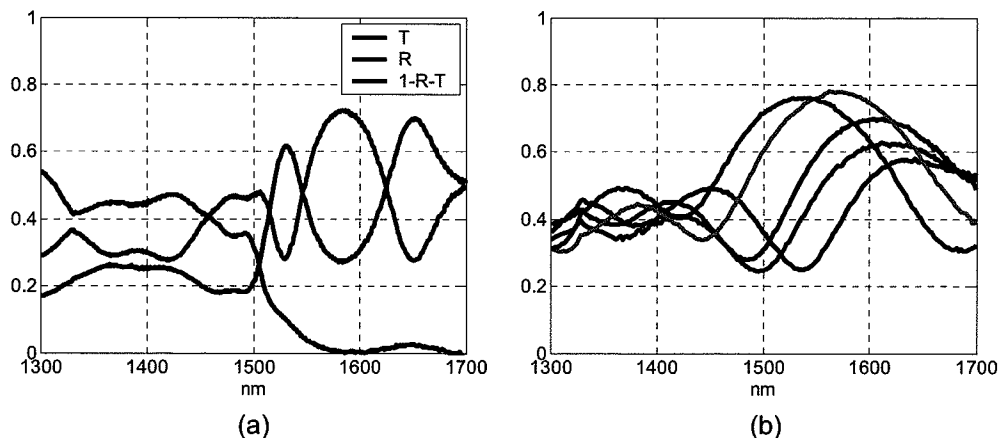
Fig. 13.2. (a) Wafer #S203-42. Transmission, reflection and absorption spectra. (b) Reflection spectra taken between multiple shallow etches after removal of the MQW region.

transmission data was compared to a matrix transfer model of the transmission. In order to get agreement between the model and data, the DBR resonance was moved to 1800 nm, indicating that the DBR was far off of the target resonance. The observed difference between the model and data around 1400 nm and shorter is likely due to absorption of the InAlGaAs layers in the DBR, which was not accounted for in the model.

Fig. 13.4 shows data taken for wafer #S203-52 grown on 10/14/03. As with wafer #S203-51 the absorption edge is shifted past the target operating point of 1550 nm. The multi-etch DBR characterization process used for wafers #S203-18 and #S203-42 was also carried out with this wafer. As shown in Fig. 13.4b, no DBR resonance can be seen within the 1300 - 1700 nm range of the spectrometer. No FTIR data was provided by OSemi for this wafer, but the lack of evidence of the DBR suggests that, as with wafer #S203-51, the DBR resonance lies far out past 1700 nm. While the optical characteristics of this wafer were poor, the electrical contacting characteristics were much better than with previous wafers. Ti:Pt:Au p-type contacts were made to this wafer and the I-V curves for several circular transmission line patterns of
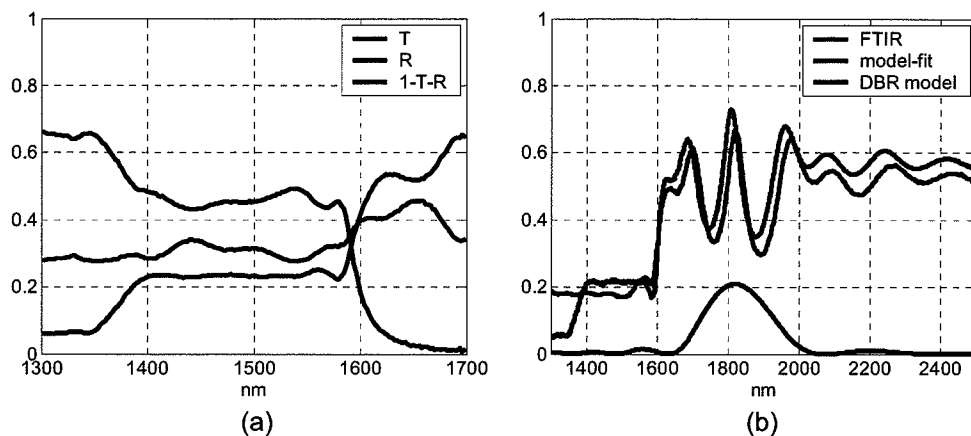
Fig. 13.3. (a) Wafer #S203-51. Transmission, reflection and absorption spectra. (b) FTIR transmission data supplied by OSemi and comparison to a transmission model fitted by adjusting the DBR resonance.

different sizes. The contact geometries are shown in Fig. 13.5b and the measured I-V curves are shown in Fig. 13.5a.
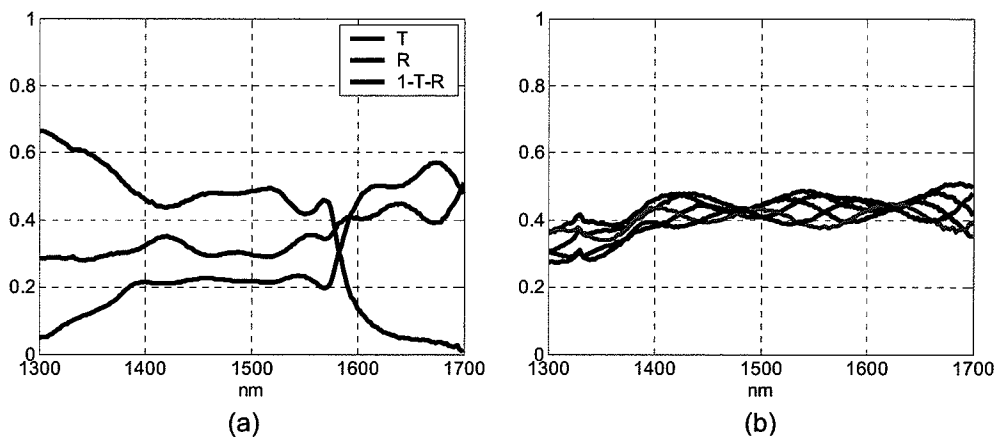
Fig. 13.4. (a) Wafer #S203-52. Transmission, reflection and absorption spectra. (b) Reflection spectra taken between multiple shallow etches after removal of the MQW region.

Combining the desirable optical properties of growth #S203-42 and the desirable electrical properties of growth #S203-52 was the obvious goal of further growths. To

(a) (b)
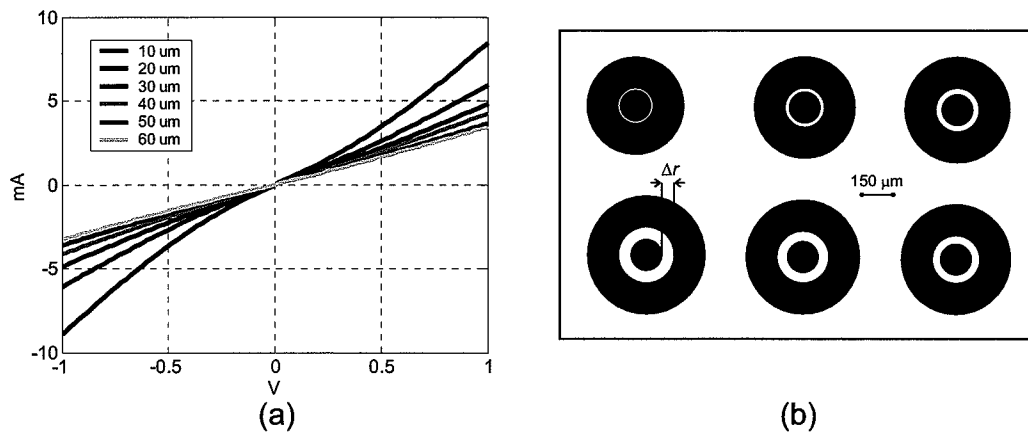
Fig. 13.5. (a) Wafer #S203-52. Ti:Pt:Au contacts to p-type InGaAs
cap layer after 450C anneal. (b) Circular transmission line contact
patterns. Six different sizes are shown. Clockwise from top left,
$\Delta r = 10\,\mu\text{m}, 20, 30, 40, 50, 60\,\mu\text{m}$.

this end, in the spring of 2004, the optical characterization setup was transported
to the OSemi site in Minnesota in an attempt to be able to characterize wafers
as soon as the were grown and provide immediate feedback to the grower. The
hope was to shorten the lag time between growths and thereby be able to achieve
more control over the optical and electrical properties. During this trip however,
OSemi's molecular beam epitaxy system suffered a critical system failure after only
one calibration growth, and no further growths were possible. The system was not
fully operational again for over half a year, at which point a search to secure a second
round of funding and another epitaxial growth vendor was underway. That funding
has now been secured through a second grant from the Photonic Technology Access
Program administered by the Optoelectronics Industry Development Association.
As of this writing a new vendor, IQE Inc., had been chosen and was in the process
of growing calibration wafers

14. CONCLUSION

To meet the expected future demand for higher bit rate optical time-division multiplexed networks, we have proposed the ultrafast optical word generator as an OTDM pulse packet generation scheme. This thesis has described the use of a direct space-to-time arrayed waveguide grating pulse shaper in combination with a high speed optical modulator array to form the ultrafast optical word generator. The DSTAWG pulse shaper operation has been demonstrated using a fixed spatial mask generating 16-pulse pulse trains of arbitrary pulse patterns. The DSTAWG has also been demonstrated in a different configuration using a liquid crystal modulator array to generate patterned pulse trains in a reprogrammable fashion.

The asymmetric Fabry-Perot modulator has been proposed as the building block for the second component of the optical word generator, the high speed modulator array. The AFPM modulator has been described and its operation simulated. A semiconductor growth structure and device photomask have been designed for the implementation of the AFPM on epitaxially grown semiconductor. Several semiconductor wafers have been grown, their relevant optical and electrical properties characterized, and their limitations determined. The work is ongoing, with a new round of funding for continued wafer growth.

A couple of key issues to be considered for future work stand out. The first is the growth of semiconductor wafers displaying both the desired optical and electrical properties. The characterization of the wafers obtained from OSemi Inc. demonstrated that there can be significant variations between wafers. The new wafers currently being grown by IQE Inc. will be important in assessing the feasibility of obtaining the necessary semiconductor material. The second issue is the envelope that is introduced on the pulse train by the relay optics in the DSTAWG pulse

shaper. For the purposes of this thesis, demonstrating reconfigurable pulse shaping, the envelope was not an issue. But in future implementations of the word generator it may be desirable to diminish the envelope. One possibility may be to use a micro-lens array, with a lens for each waveguide of the AWG, rather than a bulk optic lens, this would eliminate the off-axis problem. Another possibility is to consider a different modulator device design, one that can be brought into direct contact with the AWG, by-passing the need for relay optics. This option will probably be influenced by an evaluation of the performance of the wafers currently being grown at IQE.

LIST OF REFERENCES

LIST OF REFERENCES

[1] D.M. Spirit, A.D. Ellis, and P.E. Barnsley. Optical time division multiplexing: systems and networks. *IEEE Communications Magazine*, 32(12):56 – 62, December 1994.

[2] Y. Hibino. Recent advances in high-density and large-scale AWG multi/demultiplexers with higher index-contrast silica-based PLCs. *IEEE Journal of Selected Topics in Quantum Electronics*, 8(6):1090–1101, November 2002.

[3] Eugene Hecht. *Optics*, pages 153–155. Addison-Wesley, New York, 1998.

[4] Geunyoung Yoon.

[5] Eugene Hecht. *Optics*, page 262. Addison-Wesley, New York, 1998.

[6] http://www.photonics.com/dictionary/lookup/xq/asp/url.lookup/
entrynum.3846/letter.p/pu./qx/lookup.htm.

[7] Y. Mochida, N. Yamaguchi, and G. Ishikawa. Technology-oriented review and vision of 40-Gb/s-based optical transport networks. *Journal of Lightwave Technology*, 20(12):2272–2281, December 2002.

[8] W.H. Knox. Ultrafast technology in telecommunications. *IEEE Journal on Selected Topics in Quantum Electronics*, 6(6):1273–1278, November/December 2000.

[9] M. Saruwatari. All-optical signal processing for terabit/second optical transmission. *IEEE Journal of Selected Topics in Quantum Electronics*, 6(6):1363–1374, November 2000.

[10] J.P. Turkiewicz, E. Tangdiongga, G. Lehmann, H. Rohde, W. Schairer, Y.R. Zhou, E.S.R. Sikora, A. Lord, D.B. Payne, G.-D. Khoe, and H. de Waardt. 160 Gb/s OTDM networking using deployed fiber. *Journal of Lightwave Technology*, 23(1):225–235, January 2005.

[11] E. Tangdiongga, J.P. Turkiewicz, H. Rohde, W. Schairer, G. Lehmann, E.S.R. Sikora, Y.R. Zhou, A. Lord, D. Payne, G.D. Khoe, and H. de Waardt. 160 Gbit/s OTDM add-drop networking using 275 km installed fibres. *Electronics Letters*, 40(9):552–554, April 2004.

[12] H.F. Chou, J.E. Bowers, and D.J. Blumenthal. Compact 160-Gb/s add-drop multiplexer with a 40-Gb/s base rate using electroabsorption modulators. *IEEE Photonics Technology Letters*, 16(6):1564–1566, June 2004.

[13] S. Arahira and Y. Ogawa. 160-Gb/s OTDM signal source with 3r function utilizing ultrafast mode-locked laser diodes and modified NOLM. *IEEE Photonics Technology Letters*, 17(5):992–994, May 2005.

[14] M. Nakazawa, T. Yamamoto, and K.R. Tamura. 1.28Tbit/s-70km OTDM transmission using third- and fourth-order simultaneous dispersion compensation with a phase modulator. *Electronics Letters*, 36(24):2027–2029, November 2000.

[15] K. Uchiyama and T. Morioka. All-optical signal processing for 160 Gbit/s/channel OTDM/WDM systems. *Conference on Optical Fiber Communication, Technical Digest Series*, 54(4):ThH2/1–ThH2/3, 2001.

[16] R.P. Schmid, T. Schneider, and J. Reif. Femtosecond all-optical wavelength and time demultiplexer for OTDM/WDM systems. *Applied Physics B (Lasers and Optics)*, B74(suppl.):205–208, June 2002.

[17] H. Murai, M. Kagawa, H. Tsuji, and K. Fujii. Ea modulator-based optical multiplexing/demultiplexing techniques for 160 Gbit/s OTDM signal transmission. *IEICE Transactions on Electronics*, E88-C(3):309–318, March 2005.

[18] T.G. Ulmer, M.C. Gross, K.M. Patel, J.T. Simmons, P.W. Juodawlkis, B.R. Washburn, W.S. Astar, A.J SpringThorpe, R.P Kenan, C.M Verber, and S.E. Ralph. 160-Gb/s optical time-division multiplexed link with all-optical demultiplexing. *Journal of Lightwave Technology*, 18(12):1964–1977, December 2000.

[19] J. Ingle and S. McNown. Facets of security for all-optical networks. *Workshop on the Role of Optical Systems and Devices in Security and Anti-counterfeiting* (Washington, D.C, 1996).

[20] A.M. Weiner and A.M Kan'an. Femtosecond pulse shaping for synthesis, processing, and time-to-space conversion of ultrafast optical waveforms. *IEEE Journal of Selected Topics in Quantum Electronics*, 4(2):317–331, March/April 1998.

[21] K. Okamoto. Recent progress of integrated optics planar lightwave circuits. *Quantum and Optical Electronics*, 31(2):107–129, February 1999.

[22] D.E. Leaird, A.M. Weiner, S. Kamei, M.Ishii, A. Sugita, and K. Okamoto. Generation of flat-topped 500-GHz pulse bursts using loss engineered arrayed waveguide gratings. *IEEE Photonics Technology Letters*, 14(6):816–818, June 2002.

[23] D.E. Leaird, A.M. Weiner, S. Kamei, M.Ishii, A. Sugita, and K. Okamoto. Generation of high-repetition-rate WDM pulse trains from an arrayed-waveguide grating. *IEEE Photonics Technology Letters*, 13(3):221–223, March 2001.

[24] D.E. Leaird and A.M. Weiner. Femtosecond direct space-to-time pulse shaping. *IEEE Journal of Quantum Electronics*, 37(4):494–504, April 2001.

[25] D.E. Leaird and A.M. Weiner. Femtosecond optical packet generation by a direct space-to-time pulse shaper. *Optics Letters*, 24(12):853–855, June 1999.

[26] D.E. Leaird, A.M. Weiner, S. Shen, A. Sugita, S. Kamei, M. Ishii, and K. Okamoto. High repetition rate femtosecond WDM pulse generation using direct space-to-time pulse shapers and arrrayed waveguide gratings. *Optical and Quantum Electronics*, 33(7-10):811–826, July/October 2001.

[27] D.E. Leaird and A.M. Weiner. Femtosecond direct space-to-time pulse shaping in an integrated-optic configuration. *Optics Letters*, 29(13):1551–1553, July 2004.

[28] A.M. Weiner. Femtosecond pulse shaping using spatial light modulators. *Review of Scientific Instruments*, 71(5):1929–1960, May 2000.

[29] H. Takahashi, S. Suzuki, K. Kato, and I. Nishi. Arrayed-waveguide grating for wavelength division multi/demultiplexer with nanometre resolution. *Electronics Letters*, 26(2):87–88, January 1990.

[30] R. Adar, Charles H. Henry, C. Dragone, R.C. Kistler, and Michele A. Milbrodt. Broad-band array multiplexers made with silica waveguides on silicon. *Journal of Lightwave Technology*, 11(2):212–219, February 1993.

[31] K. Takada, M. Abe, M. Shibata, M. Ishii, and K. Okamoto. Low-crosstalk 10-GHz-spaced 512-channel arrayed-waveguide grating multi/demultiplexer fabricated on a 4-in wafer. *IEEE Photonics Technology Letters*, 13(11):1182–1184, November 2001.

[32] M.K. Smit and C. van Dam. Phasar-based wdm-devices: principles, design and applications. *IEEE Journal on Selected Topics in Quantum Electronics*, 2(2):236 – 250, June 1996.

[33] D.E. Leaird. PhD thesis.

[34] K. Tamura, E.P. Ippen, H.A. Haus, and L.E. Nelson. 77-fs pulse generation from a stretched-pulse mode-locked all-fiber ring laser. *Optics Letters*, 18(13):1080–1082, July 1993.

[35] M. Whitehead, G. Parry, and P. Wheatley. Investigation of etalon effects in GaAs-AlGaAs multiple quantum well modulators. *IEE Proceedings J*, 136(1):52, 1989.

[36] Ran-Hong Yan, Robert J. Simes, and Larry A. Coldren. Electroabsorptive Fabry-Perot reflection modulators with asymmetric mirrors. *IEEE Photonics Technology Letters*, 1(9):273–275, September 1989.

[37] M. Whitehead and G. Parry. High-contrast reflection modulation at normal incidence in asymmetric multiple quantum well Fabry-Perot structure. *Electronics Letters*, 25(9):566–568, 1989.

[38] M. Whitehead, A. Rivers, and G. Parry. Low-voltage multiple quantum well reflection modulator with on:off ratio >100:1. *Electronics Letters*, 25(15):984–985, July 1989.

[39] B. Pezeshki, J.A. Kash, and F. Agahi. Waveguide version of an asymmetric Fabry-Perot modulator. *Applied Physics Letters*, 67(12):1662–1664, September 1995.

[40] D.A.B. Miller, D.S. Chemla, T.C. Damen, A.C. Gossard, W. Wiegmann, T.H. Wood, and C.A. Burrus. Electric field dependence of optical absorption near the band gap of quantum-well structures. *Physical Review B*, 32(2):1043–1060, July 1985.

[41] T.H. Wood, C.A. Burns, D.A.B. Miller, D.S. Chemla, T.C. Damen, A.C. Gossard, and W. Wiegmann. High-speed optical modulation with GaAs/GaAlAs quantum wells in a p-i-n diode structure. *Applied Physics Letters*, 44(1):16–18, January 1983.

[42] G.D. Boyd, D.A.B. Miller, D.S. Chemla, S.L. McCall, A.C. Gossard, and J.H. English. Multiple quantum well reflection modulator. *Applied Physics Letters*, 50(17):1119–1121, April 1987.

[43] C. Fabry and A. Pérot. Théorie et applications d'une nouvelle methode de spectroscopie interférentielle. *Ann. Chim. Phys.*, 16(7):115, 1899.

[44] K.-K. Law, M. Whitehead, J.L. Merz, and L.A. Coldren. Simultaneous achievement of low insertion loss, high contrast and low operating voltage in asymmetric Fabry-Perot reflection modulator. *Electronics Letters*, 27(20):1863–1865, September 1991.

[45] D.S.Gerber, R. Droopad, and G.N. Maracas. A GaAs/AlGaAs asymmetric Fabry-Perot reflection modulator with very high contrast ratio. *IEEE Photonics Technology Letters*, 5(1):55–58, January 1993.

[46] L. Buydens and P. Demeester. High-contrast/low-voltage normally on In-GaAs/AlGaAs asymmetric Fabry-Perot modulator. *IEEE Photonics Technology Letters*, 3(12):1104–1106, December 1991.

[47] M. Nawaz, B.T. Olsen, and K. Macilvaney. High-speed modulation of GaAs/AlGaAs multiple-quantum-well (MQW) asymmetric Fabry-Perot (ASFP) reflection modulator. *Applied Physics Letters*, 7(3):128–132, February 1994.

[48] A.J. Moseley, J. Thompson, M.Q. Kearley, D.J. Robbins, and M.J. Goodwin. Low voltage InGaAs/InP multiple quantum well reflective Fabry-Perot modulator. *Electronics Letters*, 26(13):913, 1990.

[49] S.J.B. Yoo, M.A. Koza, R. Bhat, and C. Caneau. 1.5 μm asymmetric Fabry-Perot modulators with two distinct modulation and chirp characteristics. *Applied Physics Letters*, 72(25):3246–3248, June 1998.

[50] S.J.B. Yoo, J. Gamelin, R. Bhat, C Caneau, M.A. Kosa, and T.P. Lee. High-speed 1.5-μm asymmetric Fabry-Perot modulators. In *OFC '96. Optical Fiber Communication*, volume 2 of *Technical Digest Series*, pages 9–10, Washington D.C., 1996. Optical Society of America.

[51] N. Barnes, P. Healey, M.A.Z. Rejman-Greene, E.G. Scott, and R.P. Webb. 16-channel parallel optical interconnect demonstration with an InGaAs/InP MQW modulator array. *Electronics Letters*, 26(15):1126–1127, July 1990.

[52] A.J. Moseley, M.Q. Kearley, R.C. Morris, D.J. Robbins, J. Thompson, and M.J. Goodwin. Uniform 8x8 array InGaAs/InP multiquantum well asymmetric Fabry-Perot modulators for flipchip solder bond hybrid optical interconnect. *Electronics Letters*, 28(1):12–14, January 1992.

[53] Kezhong Hu, Anupam Madhukar, Ping Chen, Chris Kyriakakis, Zaheed Karim, and Armand R. Tanguay, Jr. Inverted cavity GaAs/InGaAs asymmetric Fabry-Perot reflection modulator. *Applied Physics Letters*, 59(14):1664, 1991.

[54] P. Zouganeli and G. Parry. Evaluation of the tolerance of asymmetric Fabry-Perot modulators with respect to realistic operating conditions. *IEEE Journal of Quantum Electronics*, 31(6):1140–1151, June 1995.

[55] J.F. Heffernan, M.H. Maloney, J. Hegarty, J.S. Roberts, and M. Whitehead. All optical, high contrast absorptive modulation in an asymmetric Fabry-Perot etalon. *Applied Physics Letters*, 58(24):2877–2879, June 1991.

[56] P. Zouganeli, P.J. Stevens, D. Atkinson, and G. Parry. Design trade-offs and evaluation of the performance attainable by GaAs-Al$_{0.3}$Ga$_{0.7}$As asymmetric Fabry-Perot modulators. *IEEE Journal of Quantum Electronics*, 31(5):927–943, May 1995.

[57] D.R.P. Guy and N. Apsley. Modelling of InGaAs-InP electro-absorptive Fabry-Perot modulators. In *IEE Colloquium on 'Modelling of Optoelectronic Devices' (Digest No. 030)*, page 7/1, London, 1990. IEE.

[58] J.F. Heffernan, M.H. Maloney, J. Hegarty, and J.S. Roberts. Optical switching in an asymmetric Fabry-Perot with high contrast ratio and very low insertion loss. *Electronics Letters*, 27(8):659–660, 1991.

[59] K.W. Goossen, J.E. Cunningham, and W.Y. Jan. Flip-chip bonded MQW modulator operating at ECL voltage levels. In *1998 IEEE/LEOS Summer Topical Meeting. Digest. Broadband Optical Networks and Technologies: An Emerging Reality. Optical MEMS. Smart Pixels. Organic Optics and Optoelectronics*, pages IV/15–16, New York, 1998. IEEE.

[60] Robert Eisberg and Robert Resnick. *Quantum Physics of Atoms, Molecules, Solids, Nuclei, and Particles*, pages 214–218. John Wiley & Sons Inc., New York, 1985.

[61] Robert Eisberg and Robert Resnick. *Quantum Physics of Atoms, Molecules, Solids, Nuclei, and Particles*, pages H1–H5. John Wiley & Sons Inc., New York, 1985.

[62] D.A.B. Miller. Course packet: Semiconductor optical devices, EE 243. Stanford University, 1999.

[63] D. K. Schroder. *Semiconductor Material and Device Characterization*, page 468. John Wiley & Sons, New York, 1990.

[64] Ran-Hong Yan, Robert J. Simes, and Larry A. Coldren. Surface-normal electroabsorption reflection modulators using asymmetric Fabry-Perot structures. *IEEE Journal of Quantum Electronics*, 27(7):1922–1931, July 1991.

[65] Elsa Garmire. Criteria for optical bistability in a lossy saturating Fabry-Perot. *IEEE Journal of Quantum Electronics*, 25(3):289–295, March 1989.

[66] Amnon Yariv. *Optical Electronics in Modern Communications*, pages 125–127. Oxford University Press, New York, 1997.

[67] D.J. Robbins and A.K. Tipping. Modelling of asymmetrical Fabry-Perot modulators in InGaAs/InP. In *IEE Colloquium on 'Modelling of Optoelectronic Devices' (Digest No. 030)*, page 9/1, London, 1990. IEE.

[68] Max Born and Emil Wolf. *Principles of Optics*, pages 54–60. The Macmillan Company, New York, 1959.

[69] H.A. Macleod. *Thin-Film Optical Filters*, pages 17–22. American Elsevier Publishing Company Inc., New York, 1969.

[70] D.A.B. Miller. Course packet: Advanced optoelectronic devices, EE 343. Stanford University, 2002.

[71] Y. Ando and T. Itoh. Calculation of transmission tunneling current across arbitrary potential barriers. *Journal of Applied Physics*, 61(4):1497–1502, February 1987.

[72] Shun Lien Chuang. *Physics of Optoelectronic Devices*, page 91. John Wiley & Sons, Inc., New York, 1995.

[73] David J. Griffiths. *Introduction to Quantum Mechanics*, page 55. Prentice Hall, Inc., Upper Saddle River, New Jersey, 1995.

[74] K.J. Habell and Arthur Cox. *Engineering Optics*, pages 61–86. Sir Isaac Pitman and Sons Ltd., London, 1966.

[75] Joseph Goodman. *Introduction to Fourier Optics*, page 33. The McGraw-Hill Companies, New York, 1996.

[76] Eugene Hecht. *Optics*, pages 257–271. Addison-Wesley, New York, 1998.

[77] Warren Smith. *Modern Optical Engineering*, pages 58–68. The McGraw-Hill Companies, New York, 1990.

[78] Earle Brown. *Modern Optics*, pages 173–179. Reinhold Publishing Corporation, New York, 1965.

APPENDIX

APPENDIX A

REFLECTION FROM AN ABSORBING ASYMMETRIC FABRY-PEROT CAVITY

A simple model for the asymmetric Fabry-Perot cavity (Fig. A.1) is useful to provide an understanding of the design tradeoffs inherent in the implementation of AFP modulators. The model assumes simple mirrors and uniform optical index with no wavelength dependence. Expressions for the reflectivity of asymmetric Fabry-Perot modulators given in the literature, typically for the on-resonance case, are of the form [35, 64, 65]

$$R = \frac{\left(\sqrt{R_f} - \sqrt{R_b}e^{-\alpha d}\right)^2}{\left(1 - \sqrt{R_f R_b}e^{-\alpha d}\right)^2}$$

This section briefly outlines the derivation of this reflectivity expression and the more general off-resonance case. The analysis is based on the explanation of symmetric Fabry-Perot etalons in Yariv [66], extending it to allow for asymmetric cavities and absorption.
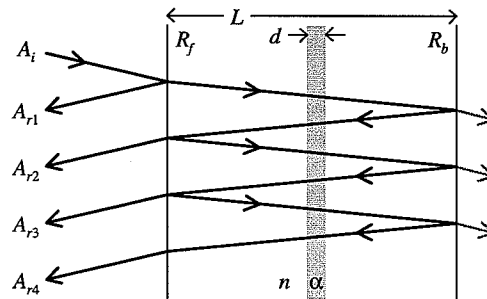
Fig. A.1. Simple asymmetric Fabry-Perot cavity with absorption layer

For the simple AFP cavity of Fig. A.1 we can write the amplitudes of the first four partial reflection components $A_{r1} \ldots A_{r4}$ in terms of the amplitude of the incident wave A_i.

$$A_{r1} = A_i r'_f \tag{A.1}$$

$$A_{r2} = A_i t'_f r_b t_f e^{i2\pi \frac{2nL}{\lambda}} e^{-\frac{\alpha}{2}2d} \tag{A.2}$$

$$A_{r3} = A_i t'_f r_b r_f r_b t_f e^{i2\pi \frac{4nL}{\lambda}} e^{-\frac{\alpha}{2}4d} \tag{A.3}$$

$$A_{r4} = A_i t'_f r_b r_f r_b r_f r_b t_f e^{i2\pi \frac{6nL}{\lambda}} e^{-\frac{\alpha}{2}6d} \tag{A.4}$$

Where r and t are reflection and transmission coefficients and the unprimed coefficients correspond to the inward faces of the mirrors. Summing over Eqns. A.1-A.4 we have the first four terms of the reflected wave amplitude A_r.

$$A_r = A_i \left(r'_f + t'_f t_f r_b e^{i2\phi} e^{-\alpha d} \left[1 + r_f r_b e^{i2\phi} e^{-\alpha d} + \left(r_f r_b e^{i2\phi} e^{-\alpha d} \right)^2 + \cdots \right] \right) \tag{A.5}$$

Where we have defined the half round-trip phase as $\phi = 2\pi n L/\lambda$. Here the term in brackets in Eqn. A.5 is the geometric series $(1 + x + x^2 + \cdots) = 1/(1 - x)$. We also utilize the relationship between reflection and transmission coefficients for non-absorbing mirrors, $r' = -r$ and $tt' = 1 - r^2$, to write the ratio of reflected to incident wave amplitude A_r/A_i as

$$\frac{A_r}{A_i} = \frac{-r_f + r_b e^{i2\phi} e^{-\alpha d}}{1 - r_f r_b e^{i2\phi} e^{-\alpha d}} \tag{A.6}$$

The reflectivity R of the AFP cavity is then given by

$$R = \left| \frac{A_r}{A_i} \right|^2 = \frac{R_f - \sqrt{R_f R_b} e^{-\alpha d} \left(2 - 4\sin^2 \phi \right) + R_b e^{-\alpha 2d}}{1 - \sqrt{R_f R_b} e^{-\alpha d} \left(2 - 4\sin^2 \phi \right) + R_f R_b e^{-\alpha 2d}}$$

$$= \frac{\left(\sqrt{R_f} - \sqrt{R_b} e^{-\alpha d} \right)^2 + 4\sqrt{R_f R_b} e^{-\alpha d} \sin^2 \phi}{\left(1 - \sqrt{R_f R_b} e^{-\alpha d} \right)^2 + 4\sqrt{R_f R_b} e^{-\alpha d} \sin^2 \phi} \tag{A.7}$$

Where we have replaced the reflection coefficient r_f (r_b) with the corresponding reflectivity R_f (R_b) according to the relation $R_f = r_f^2$. Also we have made the substitution $e^{i2\phi} + e^{-i2\phi} = 2 - 4\sin^2\phi$.

If we look at the on-resonance case, where the round-trip phase 2ϕ is a multiple of 2π, we can write the cavity reflectivity in terms of an effective back mirror reflectivity $R_b^{\text{eff}} = R_b e^{-2\alpha d}$.

$$R = \frac{\left(\sqrt{R_f} - \sqrt{R_b^{\text{eff}}}\right)^2}{\left(1 - \sqrt{R_f R_b^{\text{eff}}}\right)^2} \tag{A.8}$$

This is the expression used in section 9.1 to compare tradeoffs in cavity designs.

Alternatively, in much of the literature [35, 65] the cavity reflectivity is often expressed in terms of a composite reflectivity $R_\alpha = \sqrt{R_b R_f}\, e^{-\alpha d}$ as

$$\begin{aligned} R &= \frac{R_f\left(1 - \frac{R_\alpha}{R_f}\right)^2 + 4R_\alpha \sin^2\phi}{(1 - R_\alpha)^2 + 4R_\alpha \sin^2\phi} \\ R &= \frac{B + F\sin^2\phi}{1 + F\sin^2\phi} \end{aligned} \tag{A.9}$$

Where the on-resonance reflectivity is accumulated in B

$$B = \frac{R_f\left(1 - \left(\frac{R_\alpha}{R_f}\right)\right)^2}{(1 - R_\alpha)^2} \tag{A.10}$$

and the finesse is given by F

$$F = \frac{4R_\alpha}{(1 - R_\alpha)^2} \tag{A.11}$$

APPENDIX B

REVIEW OF TRANSFER MATRIX METHOD

The main characteristics of asymmetric Fabry-Perot modulators can be understood using the equations outlined in section A for idealized cavities. However for a real modulator, particularly one with a DBR, the distributed nature of a particular multi-layer implementation of the cavity requires a more detailed model. The optical transfer matrix method is a standard method for modelling the multi-layer structures of AFP modulators. [48, 67] The following derivation of a reflectivity calculation using the transfer matrix approach is adapted from Born [68] and Macleod [69] and is reviewed here for completeness and because it forms the basis of the simulation models used in this work.
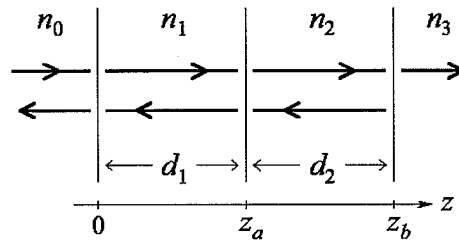
Fig. B.1. Thin film stack

Consider the system of multiple dielectric layers shown in Fig. B.1 with a plane wave normally incident from the left. We can solve the 1D Helmholtz equation in layer 1 and write the phasor fields in terms of sinusoids as

$$
\begin{aligned}
E(z) &= A\cos(k_1 z) + B\sin(k_1 z) \\
H(z) &= \frac{i}{\eta_1}\left(B\cos(k_1 z) - A\sin(k_1 z)\right)
\end{aligned}
\tag{B.1}
$$

Applying boundary conditions, $E(0)$ and $H(0)$, at $z = 0$ gives

$$A = E(0) \tag{B.2}$$

$$B = -i\eta_1 H(0)$$

The fields at $z = z_a$ can be written as

$$E(z_a) = E(0)\cos(k_1 z_a) - i\eta_1 H(0)\sin(k_1 z_a) \tag{B.3}$$

$$H(z_a) = H(0)\cos(k_1 z_a) - \frac{i}{\eta_1}E(0)\sin(k_1 z_a)$$

From this we can write a matrix expression for the fields at $z = z_a$ as a function of the fields at $z = 0$.

$$\begin{bmatrix} E(z_a) \\ H(z_a) \end{bmatrix} = \begin{bmatrix} \cos(k_1 z_a) & -i\eta_1\sin(k_1 z_a) \\ \frac{-i}{\eta_1}\sin(k_1 z_a) & \cos(k_1 z_a) \end{bmatrix} \begin{bmatrix} E(0) \\ H(0) \end{bmatrix} \tag{B.4}$$

Alternatively, we can express the fields at $z = 0$ as a function of the fields at $z = z_a$. Here we incorporate the layer thickness d_1 by the substitution $d_1 = z_a - 0$.

$$\begin{bmatrix} E(0) \\ H(0) \end{bmatrix} = \begin{bmatrix} \cos(k_1 d_1) & i\eta_1\sin(k_1 d_1) \\ \frac{i}{\eta_1}\sin(k_1 d_1) & \cos(k_1 d_1) \end{bmatrix} \begin{bmatrix} E(z_a) \\ H(z_a) \end{bmatrix} \tag{B.5}$$

Similarly, the fields at $z = z_a$ can be expressed as a function of the fields at $z = z_b$.

$$\begin{bmatrix} E(z_a) \\ H(z_a) \end{bmatrix} = \begin{bmatrix} \cos(k_2 d_2) & i\eta_2\sin(k_2 d_2) \\ \frac{i}{\eta_2}\sin(k_2 d_2) & \cos(k_2 d_2) \end{bmatrix} \begin{bmatrix} E(z_b) \\ H(z_b) \end{bmatrix} \tag{B.6}$$

$[M_L]$ is called the characteristic matrix of layer L.

$$[M_L] = \begin{bmatrix} \cos(k_L d_L) & i\eta_L\sin(k_L d_L) \\ \frac{i}{\eta_L}\sin(k_L d_L) & \cos(k_L d_L) \end{bmatrix} \tag{B.7}$$

Recall that tangential E and H fields are continuous across dielectric boundaries, and we are considering a normally incident plane wave where all fields are tangential. Therefore, it is a straightforward extension of Eqn. B.5 to see that we can express the fields at $z = 0$ as a function of the fields in any layer. In particular, using the fields at $z = z_b$,

$$\begin{bmatrix} E(0) \\ H(0) \end{bmatrix} = [M_1][M_2] \begin{bmatrix} E(z_b) \\ H(z_b) \end{bmatrix} \tag{B.8}$$

We then define the characteristic matrix $[M]$ of the entire multilayer stack as the product of the individual characteristic matrices of each layer, $[M] = [M_1][M_2]$.

In order to determine the reflectivity of the stack, we first need to determine the load impedence Z_{ld} observed at the entrance to the stack, ($z = 0$). Using the definition of impedance $Z = E/H$, we can rewrite Eqn. B.8 in terms of the load impedance $Z_{ld} = E(0)/H(0)$ and the characteristic impedance of the last layer $\eta_3 = E(z_b)/H(z_b)$.

$$H(0) \begin{bmatrix} Z_{ld} \\ 1 \end{bmatrix} = [M] \begin{bmatrix} \eta_3 \\ 1 \end{bmatrix} H(z_b) \tag{B.9}$$

We then solve this system of equations for the load impedence Z_{ld}, eliminating the H fields, giving

$$Z_{ld} = \frac{\eta_3 m_{11} + m_{12}}{\eta_3 m_{21} + m_{22}} \tag{B.10}$$

Finally, the equations for reflection coefficient ρ and reflectivity R of the multilayer stack are given by

$$\rho = \frac{Z_{ld} - \eta_0}{Z_{ld} + \eta_0} \tag{B.11}$$

$$R = |\rho|^2 = \left| \frac{(\eta_3 m_{11} + m_{12}) - \eta_0(\eta_3 m_{21} + m_{22})}{(\eta_3 m_{11} + m_{12}) + \eta_0(\eta_3 m_{21} + m_{22})} \right|^2 \tag{B.12}$$

B.1 Derivation detail of reflection, transmission, and absorption

$$\begin{bmatrix} E(0) \\ H(0) \end{bmatrix} = [M] \begin{bmatrix} E(z_b) \\ H(z_b) \end{bmatrix} \tag{B.13}$$

$$E(z) = \begin{cases} E_0^+ e^{-jkz} + E_0^- e^{jkz} & z \leq 0 \\ E_{z_b}^+ e^{-jkz} & z \geq z_b \end{cases} \tag{B.14}$$

B.1.1 Reflection

$$\begin{bmatrix} E_0^+ + E_0^- \\ \frac{1}{\eta_0} E_0^+ - \frac{1}{\eta_0} E_0^- \end{bmatrix} = \begin{bmatrix} m_{11} & m_{12} \\ m_{21} & m_{22} \end{bmatrix} \begin{bmatrix} E(z_b) \\ \frac{1}{\eta_3} E(z_b) \end{bmatrix} \tag{B.15}$$

$$E_0^+ + E_0^- = \left(m_{11} + \frac{1}{\eta_3} m_{12} \right) E(z_b) \tag{B.16}$$

$$\frac{1}{\eta_0} E_0^+ - \frac{1}{\eta_0} E_0^- = \left(m_{21} + \frac{1}{\eta_3} m_{22} \right) E(z_b)$$

$$E_0^+ + E_0^- = \frac{m_{11} + \frac{1}{\eta_3} m_{12}}{m_{21} + \frac{1}{\eta_3} m_{22}} \left(\frac{1}{\eta_0} E_0^+ - \frac{1}{\eta_0} E_0^- \right) \tag{B.17}$$

$$\eta_0 E_0^+ + \eta_0 E_0^- = \frac{\eta_3 m_{11} + m_{12}}{\eta_3 m_{21} + m_{22}} \left(E_0^+ - E_0^- \right) \tag{B.18}$$

$$E_0^- \left(\frac{\eta_3 m_{11} + m_{12}}{\eta_3 m_{21} + m_{22}} + \eta_0 \right) = E_0^+ \left(\frac{\eta_3 m_{11} + m_{12}}{\eta_3 m_{21} + m_{22}} - \eta_0 \right) \tag{B.19}$$

$$\frac{E_0^-}{E_0^+} = \frac{(\eta_3 m_{11} + m_{12}) - \eta_0 (\eta_3 m_{21} + m_{22})}{(\eta_3 m_{11} + m_{12}) + \eta_0 (\eta_3 m_{21} + m_{22})} \tag{B.20}$$

$$\rho = \frac{E_0^-}{E_0^+} = \frac{(\eta_3 m_{11} + m_{12}) - \eta_0 (\eta_3 m_{21} + m_{22})}{(\eta_3 m_{11} + m_{12}) + \eta_0 (\eta_3 m_{21} + m_{22})} \tag{B.21}$$

$$R = |\rho|^2 = \left| \frac{(\eta_3 m_{11} + m_{12}) - \eta_0 (\eta_3 m_{21} + m_{22})}{(\eta_3 m_{11} + m_{12}) + \eta_0 (\eta_3 m_{21} + m_{22})} \right|^2 \tag{B.22}$$

B.1.2 Transmission

$$E_0^+ + E_0^- = \left(m_{11} + \frac{1}{\eta_3} m_{12} \right) E_{z_b}^+ e^{-jkz_b} \tag{B.23}$$

$$\frac{1}{\eta_0} E_0^+ - \frac{1}{\eta_0} E_0^- = \left(m_{21} + \frac{1}{\eta_3} m_{22} \right) E_{z_b}^+ e^{-jkz_b}$$

$$E_0^- = \left(m_{11} + \frac{1}{\eta_3} m_{12} \right) E_{z_b}^+ e^{-jkz_b} - E_0^+ \tag{B.24}$$

$$E_0^- = E_0^+ - \eta_0 \left(m_{21} + \frac{1}{\eta_3} m_{22} \right) E_{z_b}^+ e^{-jkz_b}$$

$$2E_0^+ = \frac{1}{\eta_3} E_{z_b}^+ e^{-jkz_b} \left((\eta_3 m_{11} + m_{12}) + \eta_0 (\eta_3 m_{21} + m_{22}) \right) \tag{B.25}$$

$$\tau = \frac{E_{z_b}^+}{E_0^+} = e^{jkz_b} \frac{2\eta_3}{(\eta_3 m_{11} + m_{12}) + \eta_0(\eta_3 m_{21} + m_{22})} \tag{B.26}$$

$$T = \frac{P_{z_b}^+}{P_0^+} = \frac{\frac{1}{2}E_{z_b}^+ H_{z_b}^{+*}}{\frac{1}{2}E_0^+ H_0^{+*}} = \frac{E_{z_b}^+ \frac{1}{\eta_3} E_{z_b}^{+*}}{E_0^+ \frac{1}{\eta_0} E_0^{+*}} = |\tau|^2 \frac{\eta_0}{\eta_3} \tag{B.27}$$

$$T = \frac{4\eta_0 \eta_3}{|(\eta_3 m_{11} + m_{12}) + \eta_0(\eta_3 m_{21} + m_{22})|^2} \tag{B.28}$$

B.1.3   Absorption

$$R = |\rho|^2 = \left| \frac{(\eta_3 m_{11} + m_{12}) - \eta_0(\eta_3 m_{21} + m_{22})}{(\eta_3 m_{11} + m_{12}) + \eta_0(\eta_3 m_{21} + m_{22})} \right|^2 \tag{B.29}$$

$$T = \frac{4\eta_0 \eta_3}{|(\eta_3 m_{11} + m_{12}) + \eta_0(\eta_3 m_{21} + m_{22})|^2} \tag{B.30}$$

$$B = \eta_3 m_{11} + m_{12} \tag{B.31}$$

$$C = \eta_3 m_{21} + m_{22}$$

$$R = \frac{|B - \eta_0 C|^2}{|B + \eta_0 C|^2}$$

$$T = \frac{4\eta_0 \eta_3}{|B + \eta_0 C|^2}$$

$$1 - R = \frac{|B + \eta_0 C|^2 - |B - \eta_0 C|^2}{|B + \eta_0 C|^2} \tag{B.32}$$

$$1 - R = \frac{(|B|^2 + 2\eta_0 \Re(BC^*) + \eta_0^2 |C|^2) - (|B|^2 - 2\eta_0 \Re(BC^*) + \eta_0^2 |C|^2)}{|B + \eta_0 C|^2} \tag{B.33}$$

$$1 - R = \frac{4\eta_0 \Re(BC^*)}{|B + \eta_0 C|^2} \tag{B.34}$$

$$T = \frac{\eta_3(1-R)}{\Re(BC^*)} \tag{B.35}$$

$$
\begin{aligned}
A &= 1 - R - T \\
A &= (1-R)\left(1 - \frac{\eta_3}{\Re(BC^*)}\right)
\end{aligned}
\tag{B.36}
$$

APPENDIX C

FINITE SQUARE WELL FOR CALCULATION OF EFFECTIVE BANDGAP

In the quantum well layers of the AFP modulator, the $In_{.53}Ga_{.47}As$ and $In_{.52}Al_{.48}As$ conduction (and valence) band offset forms a finite square well potential (Fig. C.1) in which the carriers become localized. This quantum confinement leads to an elevated ground state in the well, increasing the effective bandgap above that of the bulk material. To determine the effective bandgap for the $In_{.53}Ga_{.47}As$ quantum wells of the AFP modulator we apply the finite square well solution given in Eisberg and Resnick [61] shown below.
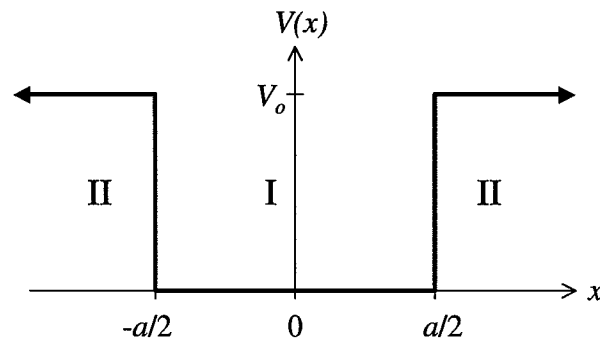

Fig. C.1. Finite square well potential

The 70 Å $In_{.52}Al_{.48}As$ barrier layers are wide enough to keep each individual well from leaking into its neighbors, so for the purposes of this calculation we treat the barriers as infinite in x. The general solution of the Schroedinger equation in the barrier layers II and the well layer I are

$$\psi(x) = \begin{cases} Ce^{k_{\mathrm{II}}x} + De^{-k_{\mathrm{II}}x} & x < -\frac{a}{2} \\ Ae^{ik_{\mathrm{I}}x} + Be^{-ik_{\mathrm{I}}x} & -\frac{a}{2} < x < \frac{a}{2} \\ Fe^{k_{\mathrm{II}}x} + Ge^{-k_{\mathrm{II}}x} & x > \frac{a}{2} \end{cases} \qquad (\text{C.1})$$

where

$$k_{\mathrm{I}} = \frac{\sqrt{2m_{\mathrm{I}}E}}{\hbar} \qquad k_{\mathrm{II}} = \frac{\sqrt{2m_{\mathrm{II}}(V_o-E)}}{\hbar} \qquad (\text{C.2})$$

The wavefunction must remain finite, so we can immediately set $D = F = 0$. Also, from (D.5) in section D, we know the boundary conditions that apply to the wavefunction. Specifically, ψ must be continuous across the boundary, and $\frac{1}{m}\frac{d}{dx}\psi$ must also be continuous across the boundary. We apply these boundary conditions at $x = \frac{a}{2}, \frac{-a}{2}$.

$$Ce^{-k_{\mathrm{II}}\frac{a}{2}} = Ae^{-ik_{\mathrm{I}}\frac{a}{2}} + Be^{ik_{\mathrm{I}}\frac{a}{2}} \qquad \left(\psi(\tfrac{-a}{2})\right) \qquad (\text{C.3a})$$

$$Ge^{-k_{\mathrm{II}}\frac{a}{2}} = Ae^{ik_{\mathrm{I}}\frac{a}{2}} + Be^{-ik_{\mathrm{I}}\frac{a}{2}} \qquad \left(\psi(\tfrac{a}{2})\right) \qquad (\text{C.3b})$$

$$\frac{1}{m_{\mathrm{II}}}Ck_{\mathrm{II}}e^{-k_{\mathrm{II}}\frac{a}{2}} = \frac{1}{m_{\mathrm{I}}}\left(Aik_{\mathrm{I}}e^{-ik_{\mathrm{I}}\frac{a}{2}} - Bik_{\mathrm{I}}e^{ik_{\mathrm{I}}\frac{a}{2}}\right) \qquad \left(\frac{1}{m}\frac{d}{dx}\psi\big|_{\frac{-a}{2}}\right) \qquad (\text{C.3c})$$

$$\frac{1}{m_{\mathrm{II}}}Gk_{\mathrm{II}}e^{-k_{\mathrm{II}}\frac{a}{2}} = \frac{1}{m_{\mathrm{I}}} - Aik_{\mathrm{I}}e^{ik_{\mathrm{I}}\frac{a}{2}} + Bik_{\mathrm{I}}e^{-ik_{\mathrm{I}}\frac{a}{2}} \qquad \left(\frac{1}{m}\frac{d}{dx}\psi\big|_{\frac{a}{2}}\right) \qquad (\text{C.3d})$$

if $A \neq -B$ and $C \neq -G$, combining equations (C.3) yields,

$$\frac{m_{\mathrm{II}}}{m_{\mathrm{I}}}k_{\mathrm{I}}\tan\left(k_{\mathrm{I}}\frac{a}{2}\right) = k_{\mathrm{II}} \qquad \text{by } \frac{(\text{C.3c})+(\text{C.3d})}{(\text{C.3b})+(\text{C.3a})} \qquad (\text{C.4a})$$

similarly, if $A \neq B$ and $C \neq G$,

$$\frac{m_{\mathrm{II}}}{m_{\mathrm{I}}}k_{\mathrm{I}}\cot\left(k_{\mathrm{I}}\frac{a}{2}\right) = -k_{\mathrm{II}} \qquad \text{by } \frac{(\text{C.3c})-(\text{C.3d})}{(\text{C.3b})-(\text{C.3a})} \qquad (\text{C.4b})$$

Because, equations (C.4a) and (C.4b) cannot both be satisfied simultaneously, the resulting wavefunctions are divided into two classes. For the first class,

$$\frac{m_{II}}{m_I} k_I \tan(k_I \tfrac{a}{2}) \;=\; k_{II} \tag{C.5a}$$

$$A \;=\; B \tag{C.5b}$$

$$C \;=\; G \tag{C.5c}$$

Now solving (C.3a) for C using (C.5), $\psi(x)$ can be written,

$$\psi(x) = \begin{cases} \left[2A\cos(k_I\tfrac{a}{2})e^{k_{II}\frac{a}{2}}\right]e^{k_{II}x} & x < -\tfrac{a}{2} \\[2mm] 2A\cos(k_I x) & \tfrac{-a}{2} < x < \tfrac{a}{2} \\[2mm] \left[2A\cos(k_I\tfrac{a}{2})e^{k_{II}\frac{a}{2}}\right]e^{-k_{II}x} & x > \tfrac{a}{2} \end{cases} \tag{C.6}$$

Similarly, for the second class,

$$\frac{m_{II}}{m_I} k_I \cot(k_I \tfrac{a}{2}) \;=\; -k_{II} \tag{C.7a}$$

$$A \;=\; -B \tag{C.7b}$$

$$C \;=\; -G \tag{C.7c}$$

Now solving (C.3a) for C using (C.7), $\psi(x)$ can be written,

$$\psi(x) = \begin{cases} \left[2Bi\sin(k_I\tfrac{a}{2})e^{k_{II}\frac{a}{2}}\right]e^{k_{II}x} & x < -\tfrac{a}{2} \\[2mm] -2Bi\sin(k_I x) & \tfrac{-a}{2} < x < \tfrac{a}{2} \\[2mm] \left[-2Bi\sin(k_I\tfrac{a}{2})e^{k_{II}\frac{a}{2}}\right]e^{-k_{II}x} & x > \tfrac{a}{2} \end{cases} \tag{C.8}$$

The complex constants A and B in equations (C.6) and (C.8) must be chosen to satisfy the normalization condition (C.9), which states that the total probability must be one.

$$\int_{-\infty}^{\infty} \psi^*(x)\psi(x)\, dx = 1 \tag{C.9}$$

Starting with the first class,

$$
\int_{-\infty}^{\infty} \psi^*\psi = \int_{-\infty}^{-\frac{a}{2}} 4A^*A \cos^2\left(k_{\mathrm{I}}\frac{a}{2}\right) e^{k_{\mathrm{II}}a} e^{2k_{\mathrm{II}}x} \, dx
$$

$$
+ \int_{-\frac{a}{2}}^{\frac{a}{2}} 4A^*A \cos^2(k_{\mathrm{I}}x) \, dx + \int_{\frac{a}{2}}^{\infty} 4A^*A \cos^2\left(k_{\mathrm{I}}\frac{a}{2}\right) e^{k_{\mathrm{II}}a} e^{-2k_{\mathrm{II}}x} \, dx
$$

$$
= 2A^*A \left(a + \frac{\sin(k_{\mathrm{I}}a)}{k_{\mathrm{I}}} + \frac{2\cos^2\left(k_{\mathrm{I}}\frac{a}{2}\right)}{k_{\mathrm{II}}} \right) \tag{C.10}
$$

We can now equate (C.9) and (C.10) and solve for the constant A. However, before obtaining a value for A, we need to determine k_{I} and k_{II} and specify the well-width a. Using relations (C.2) and (C.11c), we rewrite (C.4a) and (C.4b) to obtain the two transcendental equations (C.11a) and (C.11b).

$$
\mathcal{E} \tan \mathcal{E} = \frac{m_{\mathrm{I}}}{m_{\mathrm{II}}} \sqrt{\frac{m_{\mathrm{II}} V_o a^2}{2\hbar^2} - \frac{m_{\mathrm{II}}}{m_{\mathrm{I}}} \mathcal{E}^2} \tag{C.11a}
$$

$$
-\mathcal{E} \cot \mathcal{E} = \frac{m_{\mathrm{I}}}{m_{\mathrm{II}}} \sqrt{\frac{m_{\mathrm{II}} V_o a^2}{2\hbar^2} - \frac{m_{\mathrm{II}}}{m_{\mathrm{I}}} \mathcal{E}^2} \tag{C.11b}
$$

where

$$
\mathcal{E} = \sqrt{\frac{m_{\mathrm{I}} E a^2}{2\hbar^2}} \tag{C.11c}
$$

We are interested in the ground state (lowest energy) solution, which is given by Eqn. C.11a. Using the well width and barrier heights sketched in Fig. C.2, and appropriate effective mass values for the $In_{.53}Ga_{.47}As$ and $In_{.52}Al_{.48}As$, given in Table C.1, we plot the graphical solution. (Fig. C.3)

The ground state energy is found from the graphical solution by locating the value of $\mathcal{E}$ at the first intersection on the plots of Eqn. C.11 and then solving backwards for E, the energy. For the effective mass values of table C.1 and a 74 Å well width, the ground state energy of the electron and hole are given by

$$
E_e = 98.89 \, \mathrm{meV} \tag{C.12a}
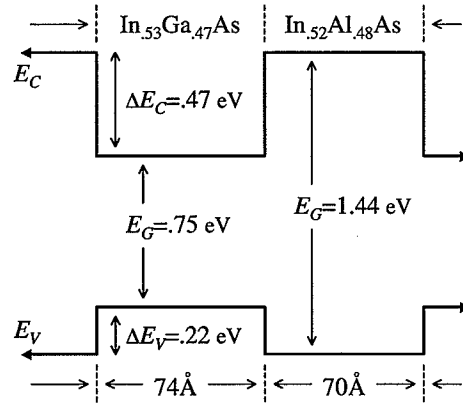$$

$$
E_h = 10.79 \, \mathrm{meV} \tag{C.12b}
$$

Fig. C.2. In$_{.53}$Ga$_{.47}$As/In$_{.52}$Al$_{.48}$As quantum well energy band diagram

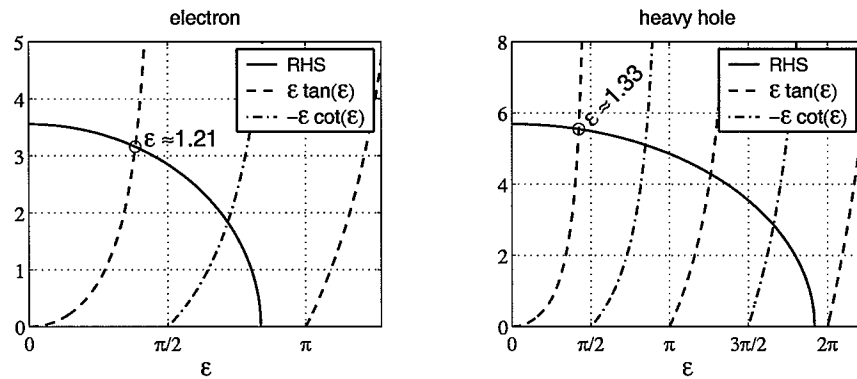| material	effective mass	
	electron (m_e^*)	heavy hole (m_{hh}^*)
In$_{.53}$Ga$_{.47}$As	0.041m_0	0.46m_0
In$_{.52}$Al$_{.48}$As	0.075m_0	0.41m_0

Table C.1
Effective masses

Fig. C.3. Graphical solution of Eqn. C.11

We now obtain values for k_{I} and k_{II} by solving (C.2) using equations (C.12) and the appropriate values from Table C.1 and Fig. C.2. ($m_0 = 5.11\mathrm{E}5$ eV/c^2, $\hbar = 6.582\mathrm{E}{-16}$ eV-sec, $c = 3\mathrm{E}8$ m/s)

	conduction band	valence band
k_I (well)	$440.9\,\mu\mathrm{m}^{-1}$	$631.5\,\mu\mathrm{m}^{-1}$
k_II (barrier)	$340.5\,\mu\mathrm{m}^{-1}$	$1588.2\,\mu\mathrm{m}^{-1}$

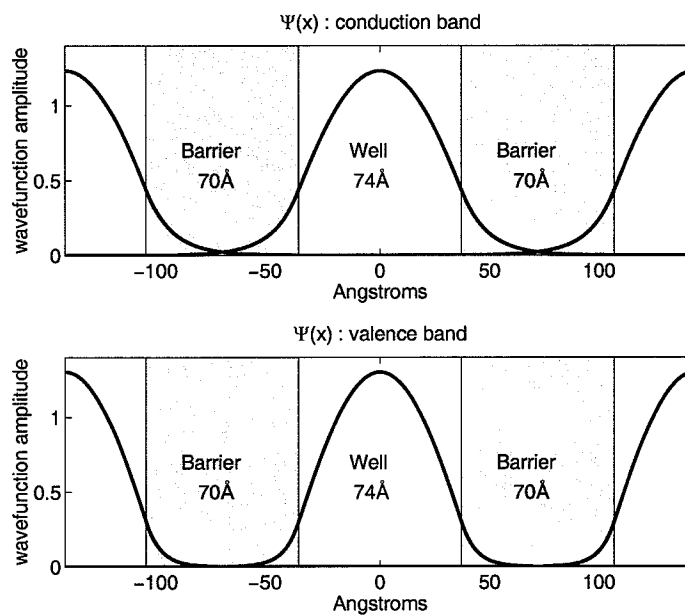Table C.2

k_I and k_II values

Fig. C.4. Wavefunction $\psi(x)/\sqrt{a}$

APPENDIX D

TUNNELING RESONANCE METHOD

In section C we calculated the elevated ground states for a finite quantum well under no applied bias. This section presents a method for determining how the ground states change under a bias. With an applied electric field, the simple square well potential (Fig. C.1 in section C) is distorted as shown in Fig. D.1.
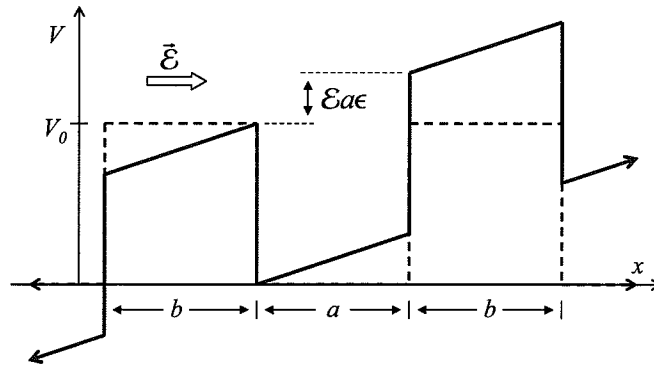

Fig. D.1. Distorted potential under applied field $\vec{\mathcal{E}}$. The zero field case is given by the dashed line.

Unlike the case of the simple square well potential (Fig. C.1), there is no straightforward analytical solution to the problem of finding the energy bound states of the potential in Fig. D.1. Instead we use a numerical method based on the tunneling resonance model. [40, 70] Here we treat the particle's wavefunction as a traveling wave originating outside of the well, and we think of the potential barriers as partial reflectors forming (along with the intervening well) a resonant cavity. Such a cavity is similar to the asymmetric Fabry-Perot cavity discussed in section 9.1. As with any resonant cavity, there are certain energies (wavelengths) for which the cavity is resonant. At these wavelengths, energy will tend to build up inside the cavity,

and subsequently as a small fraction leaks out we observe a peak in the transmitted energy. This is indeed the case for the distorted square well potential of Fig. D.1. For resonant energies, the traveling wave is less likely to reflect off the structure and more likely to tunnel through.

The tunneling resonance method can be described quite simply. It is an iterative method, where we pick a starting energy, and calculate the probability of tunneling. We then repeat this with different energies, looking for peaks in the tunneling probability. The energies with the highest probabilities are the resonant states of the system. We then recognize that these resonant states are the bound (or quasi-bound) energy states that we are looking for, since they are the states with the highest probability of finding the particle inside the well.

D.1 Transfer Matrix Method

Implementing the tunneling resonance method requires that we be able to determine the tunneling probabilty of the potential (Fig. D.1) for a given energy. Since as stated above there is no simple analytical solution for this potential, we approximate it by breaking it into finite constant segments as shown in Fig. D.2. The solution for a constant potential is known, so these segments can be handled one at a time and then stitched back together, observing the boundary conditions as we move from one segment to the next. This process is known as the transfer matrix method [70,71], because it sets up a cascade of matrices which describe how the wavefunction changes across each boundary. The resulting matrix is known as the transfer matrix.

To set up the formalism of the transfer matrix method, we begin with the time-independent Schroedinger equation for variable effective mass. [72]

$$-\frac{\hbar^2}{2}\frac{d}{dx}\left(\frac{1}{m^*(x)}\frac{d}{dx}\psi(x)\right) + V\psi(x) = E\psi(x) \qquad (D.1)$$
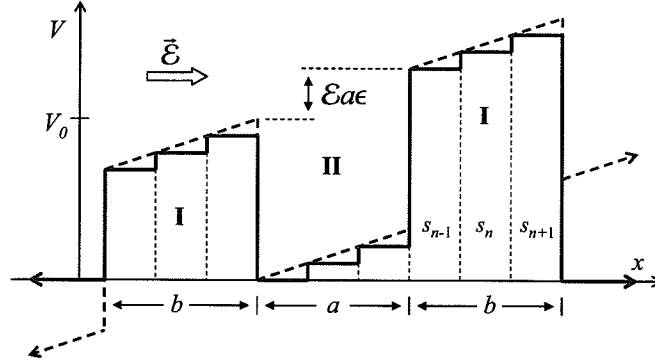
Fig. D.2. Approximation of potential by division into constant segments

Here m^* is the effective mass, V is the barrier potential, and E is the energy. The general solution to (D.1) describes two opposing travelling waves.

$$\Psi(x,t) = \psi(x)e^{-iwt} = Ae^{i(kx-wt)} + Be^{-i(kx+wt)}$$

$$\psi(x) = Ae^{ikx} + Be^{-ikx} \tag{D.2}$$

where

$$k = \sqrt{\frac{2m^*}{\hbar^2}(E-V)} \tag{D.3}$$

Note that when $V > E$, k will be imaginary, which is consistent with a decaying wave.

In order to determine how the wavefunction Ψ will behave at a border, we need to determine the continuity conditions on ψ and $\frac{d}{dx}\psi$. We integrate the Schrodinger equation (D.1) from $-\epsilon$ to ϵ and take the limit as $\epsilon \to 0$. [73]

$$\lim_{\epsilon \to 0} \int_{-\epsilon}^{+\epsilon} \frac{d}{dx}\left(\frac{1}{m^*}\frac{d}{dx}\psi(x)\right) dx = \lim_{\epsilon \to 0} \frac{2}{\hbar^2} \int_{-\epsilon}^{+\epsilon} (V-E)\psi(x)\,dx \tag{D.4}$$

The terms inside the integral on the right hand side of (D.4), (E, V, ψ), are all finite, so in the limit the right hand side goes to zero. The left hand side gives us the relation for the continuity of $\frac{d\psi}{dx}$ involving the effective mass m^*.

$$\lim_{\epsilon \to 0} \left(\frac{1}{m^*} \frac{d\psi}{dx} \bigg|_{+\epsilon} - \frac{1}{m^*} \frac{d\psi}{dx} \bigg|_{-\epsilon} \right) = 0 \qquad (D.5)$$

Equation (D.5) shows us that $\frac{d\psi}{dx}$ is discontinuous when the effective mass changes across a boundary. The derivative does remain finite however, since m^* is finite, which means ψ itself must be continuous across boundaries.

With the general solution wavefunction and the boundary conditions, we can now write down the transfer matrix to describe the wavefunction across a segment. Consider segment s_2 shown in Fig. D.3. Assume that A_3 and B_3, the wavefunction coefficients in segment s_3, are known. Using the boundary conditions, we can write the coefficients in segment s_2 on the left side of the x_{23} boundary, A_2 and B_2.
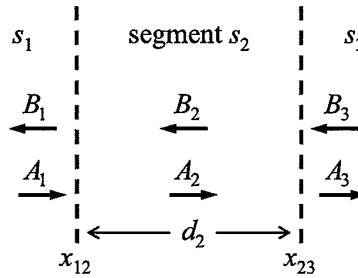

Fig. D.3. Close-up of segments s_1, s_2, and s_3 showing the wavefunction coefficients A_n and B_n for each segment.

The continuity of ψ across the x_{23} boundary gives,

$$\psi_2(x_{23}) = \psi_3(x_{23})$$
$$A_2 e^{ik_2 x_{23}} + B_2 e^{-ik_2 x_{23}} = A_3 e^{ik_3 x_{23}} + B_3 e^{-ik_3 x_{23}} \qquad (D.6)$$

Similarly, the continuity of $\frac{1}{m^*}\frac{d}{dx}\psi$ at the x_{23} boundary gives,

$$\frac{1}{m_2^*} \frac{d\psi_2}{dx} \bigg|_{x_{23}} = \frac{1}{m_3^*} \frac{d\psi_3}{dx} \bigg|_{x_{23}}$$
$$\frac{1}{m_2^*} ik_2 \left(A_2 e^{ik_2 x_{23}} - B_2 e^{-ik_2 x_{23}} \right) = \frac{1}{m_3^*} ik_3 \left(A_3 e^{ik_3 x_{23}} - B_3 e^{-ik_3 x_{23}} \right) \qquad (D.7)$$

Solving (D.6) and (D.7) for A_2 and B_2, we can write the transfer matrix D_{23} which describes how the wavefunction behaves at the x_{23} boundary.

$$\begin{bmatrix} A_2 \\ B_2 \end{bmatrix} = \underbrace{\begin{bmatrix} \frac{1+\Delta}{2}e^{i(k_3-k_2)x_{23}} & \frac{1-\Delta}{2}e^{-i(k_3+k_2)x_{23}} \\ \frac{1-\Delta}{2}e^{i(k_3+k_2)x_{23}} & \frac{1+\Delta}{2}e^{-i(k_3-k_2)x_{23}} \end{bmatrix}}_{D_{23}} \begin{bmatrix} A_3 \\ B_3 \end{bmatrix} \tag{D.8}$$

where

$$\Delta = \frac{m_2}{m_3}\frac{k_3}{k_2}$$

Now, to write the wavefunction coefficients in segment s_1 in terms of the coefficients in segment s_3, we simply cascade the transfer matrices.

$$\begin{bmatrix} A_1 \\ B_1 \end{bmatrix} = [D_{12}][D_{23}] \begin{bmatrix} A_3 \\ B_3 \end{bmatrix} \tag{D.9}$$

APPENDIX E

ABERRATIONS

In idealized optical systems, also called paraxial, first-order, or Gaussian systems, all light from an object point is assumed to be collected at a single image point, and a planar object is assumed to form a planar image. The performance of practical optical systems departs from the predictions of the paraxial approximation in three ways, Monochromatic aberrations, chromatic effects and diffraction. [74] Chromatic aberrations arise from the material dispersion characteristics of optical elements in the system. Chromatic aberration can be reduced by using achromat components which are designed to use two or more materials with compensating dispersion characteristics. Achromat lenses were used for the experiments of this thesis. Diffraction is similar to interference, and is a consequence of the wave nature of light. Diffraction effects become significant only when the lateral extent of a light wavefront is confined, by optical elements in the system, to a size that is on the order of a wavelength. [75] The elements of the optical relay system described in this thesis, as shown in Fig. 6.1, were much larger than the operating wavelength (1.55 μm), and the performance of the system was therefore dominated by monochromatic aberrations.

Monochromatic aberrations are departures in imaging performance of a real system compared with the predictions of paraxial theory, which arise due to two specific approximations of the paraxial theory. These are the approximation of $\sin(\theta)$ and $\cos(\theta)$ to the first terms of their series expansions, where θ is the angle that a ray makes with the optical axis. The series expansions are,

$$\sin(\theta) = \theta - \frac{\theta^3}{3!} + \frac{\theta^5}{5!} - \frac{\theta^7}{7!} + \dots$$

$$\cos(\theta) = 1 - \frac{\theta^2}{2!} + \frac{\theta^4}{4!} - \frac{\theta^6}{6!} + \dots \qquad \text{(E.1)}$$

The paraxial approximation then is $\sin(\theta) \simeq \theta$, $\cos(\theta) \simeq 1$. [74, 76] For refraction at a spherical interface like that shown in Fig. E.1, paraxial theory gives [3]

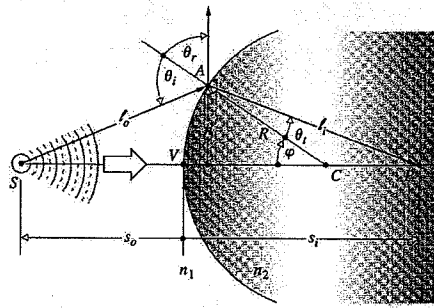$$\frac{n_1}{s_o} + \frac{n_2}{s_i} = \frac{n_2 - n_1}{R} \qquad \text{(E.2)}$$

Fig. E.1. Refraction at a spherical interface. [3]

The above assumptions are reasonable for a small cone of rays whose angular deviation from the optical axis is slight, known as the paraxial region. When the angle made between the ray and the optical axis is large however, the paraxial approximation breaks down and a better theory is needed. This so called third-order theory keeps the first two terms of the series expansions, rather than just one, $\sin(\theta) \simeq \theta - \frac{\theta^3}{3!}$, and $\cos(\theta) \simeq 1 - \frac{\theta^2}{2!}$, and Eqn. E.2 becomes [76]

$$\frac{n_1}{s_o} + \frac{n_2}{s_i} = \frac{n_2 - n_1}{R} + h^2 \left[\frac{n_1}{2s_o} \left(\frac{1}{s_o} + \frac{1}{R} \right)^2 + \frac{n_2}{2s_i} \left(\frac{1}{R} - \frac{1}{s_i} \right)^2 \right] \qquad \text{(E.3)}$$

The differences between the third-order theory and paraxial theory are known as the Seidel aberrations or monochromatic aberrations. There are five monochromatic

aberrations, namely spherical aberration, coma, astigmatism, field curvature (or Petzval curvature), and distortion. [77]

Spherical aberration (Fig. E.2) is the variation of the focal distance for different radial heights in the aperture. The spherical aberration is termed positive when the marginal rays (or radially outer rays) have a shorter focal length than the paraxial rays (rays with a small angular deviation from the optical axis). Spherical aberration can be measured longitudinally, along the optical axis, or transversely along the image plane. [77, 78]
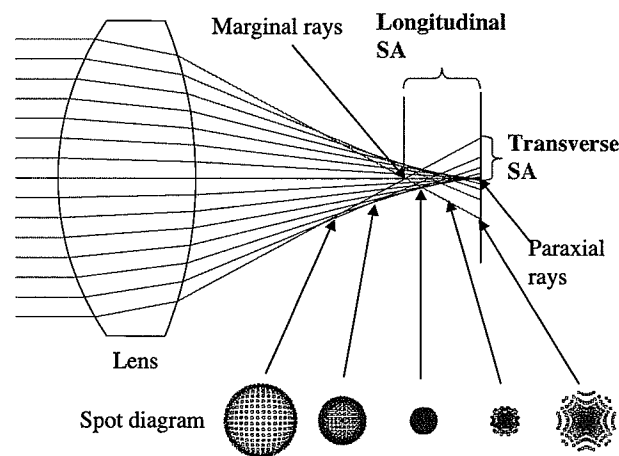

Fig. E.2. Illustration of positive spherical aberration. [4]

Coma (Fig. E.3) is the dependence of magnification on the aperture. Rays which pass through the outer (radially) portions of the lens focus at a different height on the image plane than do rays which pass through the center portion of the lens. Positive coma means that rays passing through the outer portions of the lens produce an image of higher magnification than rays passing through the center of the lens. [76]

Astigmatism (Fig. E.4) arises when an object point lies a significant radial distance off of the optical axis. For a one lens system, the principal ray connects the object point to the center of the lens. The tangential plane is then defined as the plane containing both the principal ray and the optical axis. The sagittal plane is the plane orthogonal to the tangential plane that also contains the principal ray.
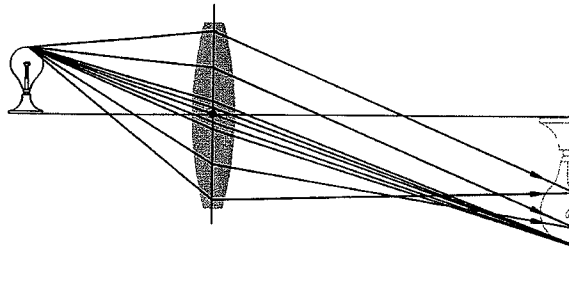
Fig. E.3. Illustration of negative coma. [5]

Astigmatism occurs when the focus of rays lying in the sagittal plane does not coincide with the focus of rays lying in the tangential plane. Astigmatism does not occur for axial object points since the system is then rotationally symmetric about the optical axis, and the sagittal and tangential planes are indistinguishable. [76,77]
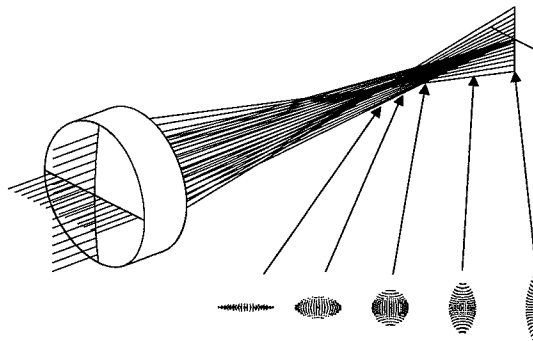

Fig. E.4. Illustration of astigmatism. [4]

Field curvature, or Petzval curvature, (Fig. E.5) is the longitudinal deviation of the image surface from the ideal paraxial image plane. Or, in other words, the tendency of optical systems to image better on a curved surface then on a flat surface, given a planar object. Positive lenses cause inward curvature of the surface, toward the object plane. Negative lenses cause outward curvature, away from the object plane. [76, 77] The curved surface of best image is known as the Petzval surface. (Fig. E.6)
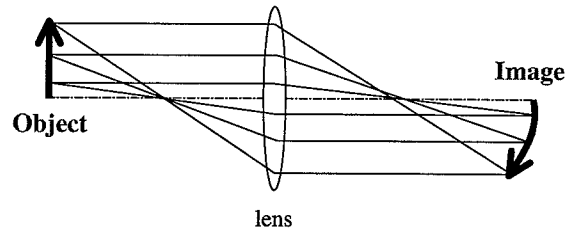
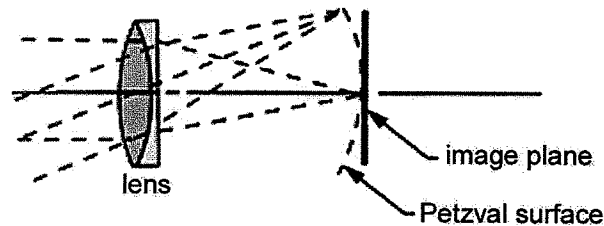Fig. E.5. Illustration of field-curvature. [4]

Fig. E.6. Illustration showing the Petzval surface. [6]

Distortion (Fig. E.7) results when the magnification of the optical system is dependent on the position of the object point. When off-axis object points experience a different magnification than object points close to the axis, the image as a whole deviates from the paraxial image. When the magnification increases with the radial distance of an object point, positive distortion or pincushion occurs. When the magnification decreases with radial distance it is called negative distortion or barrel distortion. [76,77]

In addition to the five Seidel aberrations, spherical aberration, coma, astigmatism, field curvature, and distortion, there are also higher order effects related to the higher order terms of the power series expansions of Eqn. E.1. For the relay optics system described in Section 6 however, the pulse train envelope appears to have largely been dominated by the Seidel aberrations, and in particular the effects of field curvature.
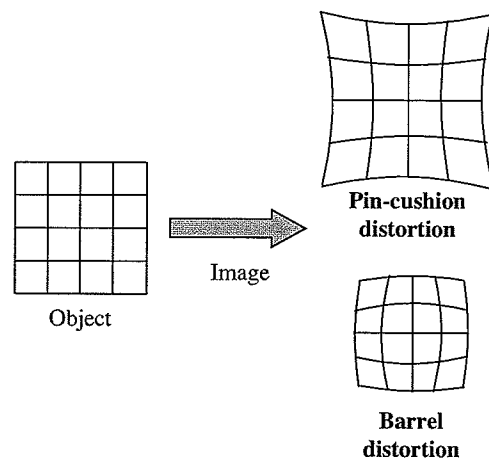
Fig. E.7. Illustration of distortion. [4]

VITA

VITA

Nathaniel A. Webster graduated from Princeton University in 1998 with a B.S.E. degree in Electrical Engineering. He is currently a doctoral student at Purdue University and a research assistant in the Ultrafast Optics and Fiber Communications Laboratory. In 1998 he was the recipient of a Meissner Fellowship and in 1999 he received a Magoon Award for outstanding teaching.